



Morphology and Optical Properties of Liquid-Liquid Phase Separated Particles

Ph.D Thesis
Mehrnoush Mousavi-Fard

DISS. ETH NO. 24389

*Morphology and Optical Properties of
Liquid-Liquid Phase Separated
Particles*

A thesis submitted to attain the degree of
DOCTOR OF SCIENCES of ETH ZÜRICH
(Dr. sc. ETH Zürich)

Presented by

Mehrnoush Mousavi-Fard

MSc in Chemistry, University of Copenhagen

Born on 21.09.1980

Citizen of Canada

Accepted on the recommendation of

Prof. Dr. Thomas Peter, examiner
Dr. Ulrich Krieger, co-examiner
Prof. Dr. Thomas Mentel, co-examiner

2017

Contents

Abstract	vii
Zusammenfassung	ix
Dedication	xii
1. Introduction: The Atmospheric Aerosols	1
1.1 Size distribution	1
1.2 Emission sources and chemical composition	3
1.3 Human health effects	5
1.4 The climate effects of aerosols	7
1.4.1 The direct effect of aerosols	7
1.4.2 The indirect effect of aerosols	8
1.5 Hygroscopic behaviour of atmospheric aerosols	9
1.6 Liquid-liquid phase separation	13
1.7 Morphology of mixed aerosol particles	14
1.8 Motivations and objectives of the thesis	15
2. Theoretical Aspects of Phase Separation	17
2.1 Water activity (a_w)	17
2.2 Deliquescence and Efflorescence	18
2.3 Mechanisms of liquid-liquid phase separation	21
2.3.1 Spinodal decomposition	21
2.3.2 Nucleation and growth	22
3. Optical Properties of Aerosols	25
3.1 Optical parameters	26
3.1.1 Mie theory	26
3.1.2 Absorption and scattering of spherical particles	26
3.2 Light absorbing material in the atmosphere	28

Contents

3.3	Wavelength-dependant light absorption of BrC	31
3.4	The impact of morphology on the optical properties of BrC aerosols	32
4.	Experimental	34
4.1	Material	34
4.2	Sample preparation	35
4.3	Optical microscopy	36
4.4	Calibration methods of RH and temperature	37
5.	Kinetic Limitations to Inorganic Ion Diffusivity and to Coalescence of Inorganic inclusions in Viscous Liquid-liquid Phase Separated Particles	39
	Abstract	39
5.1	Introduction	40
5.2	Experimental Scheme	43
5.2.1	Material and sample preparation	43
5.2.2	Flow cell microscopy	44
5.2.3	Image analysis	46
5.3	Results and Discussions	46
5.3.1	Morphology of aqueous AS/CA particles during phase separation	49
5.3.2	The impact of drying rate on morphology	51
5.3.3	The impact of temperature on morphology	53
5.3.4	Investigating the geometry of inclusions	59
5.3.5	Estimating the viscosity of the AS/CA/H ₂ O ternary system	60
5.3.6	Quantification of ammonium sulfate diffusivity in organic-rich particle shell	64
5.4	Atmospheric implications	71
5.5	Conclusions	74
	Appendix 5.1: Estimating the concentration of AS in the organic phase after LLPS	75

Contents

6. Radiative impact of liquid-liquid phase separation for aerosol containing a molecular absorber	78
Abstract	78
6.1 Introduction	79
6.2 Model system & methodical approach	81
6.2.1 Concentric versus eccentric core-shell computations	81
6.3 Results and discussions	87
6.4 Atmospheric implications	91
6.4.1 The importance of looking at scattering cross-section	91
6.4.2 Calculating the impact of LLPS on radiative forcing of a thin aerosol layer	93
6.5 Conclusions	95
Appendix 6.1: Calculating the real part of refractive index	96
Appendix 6.2: Spectral Irradiance	98
7. Summary and Final Remarks	100
Bibliography	105
Acknowledgements	120
Curriculum Vitae	122

Abstract

The physical state of aerosols plays an important role in dictating their morphology and as a result impacting the optical properties of aerosols, mass-to-particle partitioning, and the chemistry in atmosphere. Tropospheric aerosols are composed of inorganic salts, a wide range of organic compounds and water. Aerosol mass spectrometry data taken during field measurements have shown that these components are mostly internally mixed. As relative humidity (RH) changes in an air parcel, these particles undergo phase transitions including deliquescence, efflorescence, and liquid-liquid phase separation (LLPS). After the onset of LLPS, particles may adopt different morphologies such as core-shell, partially engulfed, or the formation of multiple inorganic inclusions in the organic-rich phase.

Since there is not yet a direct measurement technique to determine the physical state and morphology of ambient aerosol particles, laboratory experiments are needed to gain deeper knowledge into the possible phase transitions and morphologies of internally mixed aerosol particles under atmospheric conditions.

In previous studies regarding LLPS, and the corresponding morphologies of atmospherically relevant particles, the focus was heavily on the thermodynamics of phase transition and the possible kinetic limitation especially under colder mid-to-upper tropospheric temperatures was not studied much.

In the first part of this thesis, in order to investigate the potential impacts of kinetics on the formation of LLPS and different morphologies, we studied the change in morphology of a model system for tropospheric aerosol, namely the ternary ammonium sulfate (AS) / carminic acid / H₂O system at different temperatures and drying rates for droplets between 40 – 75 μm in diameters using optical microscopy.

In our system, LLPS started by the nucleation of inorganic inclusions in the organic-rich phase and grow to different extent to form the final configuration, which was strongly sensitive to the drying rate and to a lesser extent to temperature.

Kinetic analysis of the coagulation of separate phase inclusions was used to estimate viscosity of the organic rich phase after the onset of LLPS and AS diffusivity was calculated applying the Stokes-Einstein relationship.

In addition, AS diffusivity was estimated by measuring the growth of AS inclusions in the matrix and the result was compared to AS diffusivity calculated from viscosity.

We have also used the data of our model system for estimating the time required for a submicron particle undergoing LLPS to grow an inorganic inclusion to at least 10 nm in diameter assuming specific diffusion activation energies. Our estimation predicts no kinetic limitation for the formation of LLPS under low upper tropospheric temperatures and strongly suggest that phase separated mixed submicron particles will exhibit a core-shell morphology.

In the second part of this thesis, the impact of LLPS on the optical properties of mixed aerosols particles containing absorbing organic carbon (BrC) was investigated numerically. In addition to the traditional approach assuming a concentric core-shell morphology, an eccentric core-shell model was used to calculate the extent of change in optical efficiencies that LLPS might inflict on accumulation-sized aerosols. Based on calculated results, we conclude that for the OIR range investigated; concentric core shell morphology approximates the mean of an ensemble of random positioned eccentric core shell morphologies very well.

To see how important this change might be in terms of radiative forcing, we perform a simple radiative transfer calculation to calculate the ratio of absorption and scattering properties of the phase separated versus homogeneously mixed aerosol on a single particle basis. We integrate the results over the UV-VIS region of the solar spectrum to get the ratio of direct forcing in the context of an isolated thin aerosol layer. This introduces a correcting factor that can be implemented by global modelers to take into account the existence of a two-phase particle instead of treating all the particles as homogeneous.

Zusammenfassung

Der Phasenzustand des atmosphärischer Aerosol spielt eine wichtige Rolle für die Morphologie der einzelnen Aerosolpartikel, beeinflusst die optischen Eigenschaften des Aerosol und die Partitionierung zwischen Gas- und Partikelphase sowie die Chemie der Atmosphäre. Troposphärische Aerosolpartikel bestehen aus anorganischen Salzen, einer Vielzahl organischer Moleküle und Wasser. Massenspektrometrische Untersuchungen ergaben, dass diese Komponenten im atmosphärischen Aerosol intern gemischt vorliegen. Mit Änderung der relativen Feuchte (RH) in einem Luftpaket geschehen in den Aerosolpartikeln Phasenübergänge wie Deliquescenz, Effloreszenz und Entmischung einer homogenen flüssigen Phase in zwei flüssige Phasen (eine reich an anorganischen Bestandteilen, die andere reich an organischen Bestandteilen). Nach Eintritt einer derartigen Entmischung können die beiden flüssigen Phasen verschiedene Morphologien innerhalb eines Aerosolpartikels annehmen: die anorganische Phase kann komplett von einer organischen Phase umhüllt sein, sie kann nur teilweise umhüllt sein oder es können auch mehrere anorganische Einschlüsse innerhalb der organischen Phase vorliegen.

Da bislang noch keine Methoden existieren, die eine direkte Messung des Phasenzustandes und der Morphologie des Aerosols erlauben, sind Labormethoden an Modellsystemen erforderlich, um ein tieferes Verständnis in Phasenübergänge und Morphologie gemischter Aerosolpartikel unter atmosphärischen Bedingungen zu gewinnen.

In vorangegangenen Studien bezüglich der Entmischung flüssiger Phasen lag der Fokus auf der Thermodynamik des Phasenüberganges und mögliche kinetische Einflüsse bei niedrigen Temperaturen wie sie in der mittleren und oberen Troposphäre vorliegen, wurden nicht intensiv untersucht.

Im ersten Teil dieser Arbeit wurden an einem Modellsystem für troposphärisches Aerosol, einer wässrigen ternären Mischung aus Ammoniumsulfat (AS) und Karminsäure (CA), die entstehenden Morphologien nach Phasentrennung bei verschiedenen Trocknungsraten und bei unterschiedlichen Temperaturen untersucht. Dies geschah mit Hilfe optischer Mikroskopie an einzelnen Tröpfchen mit Grössen zwischen $40 \mu\text{m}$ und $75 \mu\text{m}$ auf einem hydrophoben Substrat.

In unserem Modellsystem wurde die Phasentrennung durch das Entstehen anorganischer Einschlüsse in der organischen Phase sichtbar, diese Einschlüsse wuchsen und koagulierten um eine endgültige Morphologie anzunehmen, welche stark von Trocknungsrate und Umgebungstemperatur abhing.

Untersuchungen der Koagulationskinetik erlaubte die Viskosität der organischen Phase zu bestimmen und aus dieser Viskosität wurde über die Stokes-Einstein Beziehung die Diffusion von AS in der organischen Phase abgeschätzt. Unabhängig davon wurde aus dem gemessenen initialen Wachstum der anorganischen Einschlüsse ebenfalls die AS Diffusivität bestimmt und mit der aus der Viskosität abgeschätzten verglichen.

Die so erhaltenen Daten wurden genutzt, um die Zeit abzuschätzen, die bei niedrigen troposphärischen Temperaturen benötigt wird, um einen Einschluss auf eine Grösse von 10 nm anwachsen zu lassen. Unsere Abschätzung führt uns zu dem Schluss, dass dies hinreichend schnell geschieht, so dass wir keine kinetische Hemmung der Entmischung einer flüssigen Phase unter atmosphärischen Bedingungen erwarten. Ausserdem lassen unsere Beobachtungen den Schluss zu, dass die entstehende Morphologie nicht aus mehreren Einschlüssen besteht, sondern aus einer anorganischen Phase, die von einer organischen Phase umhüllt wird.

Im zweiten Teil der Arbeit wurde der Einfluss der Entmischung auf die Strahlungswechselwirkung atmosphärische Aerosolepartikel, die molekulare absorbierende Moleküle den sogenannten „braunen“ Kohlenstoff (BrC) enthalten. Dabei wurde angenommen, dass sich dieser BrC nach Phasentrennung in der organischen Phase befindet und dass sich in dieser Phase eine sphärische, exzentrische, transparente anorganische Phase ausbildet. Für solche Systeme wurden die optischen Effizienzen für Absorption und Streuung sowie der Asymmetrieparameter berechnet. Dabei stellte sich heraus, dass für realistische Verhältnisse von organischer und anorganischer Phase und im Grössenbereich von Partikeln der Akkumulationsmode die Exzentrizität keine grosse Rolle spielt, was für die numerische Behandlung des Problems wichtig ist. Um die Wichtigkeit der Phasentrennung auf die Strahlungsantrieb zu untersuchen, haben wir das Verhältnis des Strahlungsantriebs für phasenetrennte Teilchen relativ zu homogen gemischten Partikeln berechnet und diese über den UV-VIS-Bereich des solaren Spektrums integriert. Dies ergibt einen Korrekturfaktor, der genutzt werden kann, um die Grössenordnung des Effekts auf die globale Strahlungsbilanz abzuschätzen.

DEDICATION

To Saeid, Mina, & Maya, for their continuous love, support, and inspiration.

Chapter 1

1. The Atmospheric Aerosol

Aerosols are suspensions of solid and liquid particles in ambient air [Seinfeld & Pandis, 2006]. Atmospheric aerosol particles originate from a wide variety of natural and anthropogenic sources. Primary particles are directly emitted as liquids or solids from sources such as biomass burning, incomplete combustion of fossil fuels, volcanic eruptions, sea spray (i.e., breaking waves and bubble-bursting), biological materials (plant fragments, microorganisms, pollen, etc.), and wind-driven or traffic-related suspension of road, soil, and mineral dust [Seinfeld & Pandis, 2006]. Secondary particles, on the other hand, are formed by gas-to-particle conversion in the atmosphere. Primary gaseous species undergo chemical reaction, which convert them into low volatility products through which gas-phase precursors are oxidized to form lower-volatility species that subsequently condense into the particulate phase, either forming new particles through a process called nucleation or condensing onto pre-existing particles [Seinfeld & Pandis, 2006]. The aerosol particles have relatively short lifetimes in the lower atmosphere, typically from days to weeks, and thus they have a high spatial and temporal variability.

1.1. Size distributions

Atmospheric particles emitted from air pollution sources and formed by natural processes have multitude of different shapes and densities. That is why in air pollution control, it is necessary to use a particle size definition that directly relates to how the particle behaves in a fluid such as air. For this purpose the aerodynamic diameter is defined as the diameter of a spherical particle having a density of 1 g/cm^3 that has the same inertial properties in air as the particle of interest [Seinfeld &

Pandis, 2006].

Depending on the physical and chemical processes involved in the particle formation and growth, the particles are conventionally divided into different size fractions, generally called “modes” (Figure 1.1). These modes differ in their origin, transformation, removal from atmosphere, and acquire different chemical composition and optical properties [Seinfeld & Pandis, 2006]. Their deposition pattern in respiratory tract is also significantly different from each other [Seinfeld & Pandis, 2006]. These modes are called nucleation, Aitken, accumulation, and coarse modes [CAFÉ 2004, Seinfeld & Pandis, 2006].

The nucleation (or nuclei) mode resides in the range up to 10 nm [Seinfeld & Pandis, 2006] of particle diameter and usually presents its maximum number-density around 5-10 nm of particle diameter. New particles are formed by homogenous nucleation from chemical conversion of gaseous precursors into low volatility vapours. These particles have a lifetime of hours in the atmosphere as they rapidly coagulate with larger particles or grow into larger sizes due to condensation. Classical nucleation theory shows that the nucleation highly depends on the concentrations of the gaseous precursors, relative humidity and temperature. In particular, the nucleation is favored by decreases in the temperature and/or increases in the relative humidity [Easter and Peter, 1994].

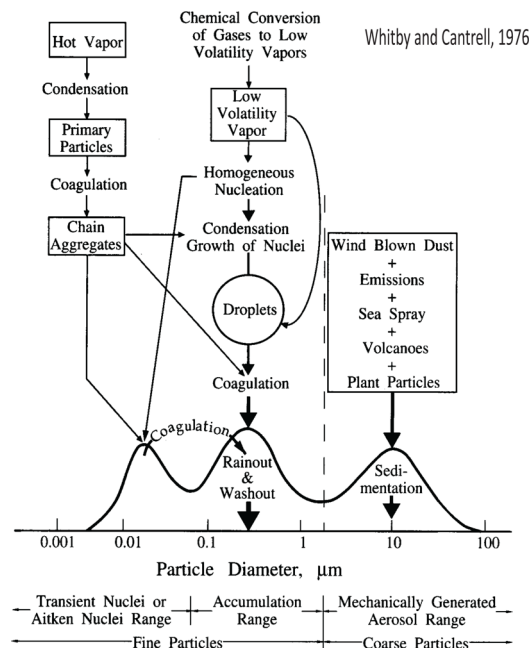


Figure 1.1. Atmospheric aerosol typical size distribution including modes, sources, formation and sinks. [Whitby and Cantrell, 1976].

Aitken mode particles range from 10 nm to 0.1 μm [Seinfeld & Pandis, 2006] in diameter and originate from either primary particles, natural and anthropogenic, or by growth of nucleation mode particles. It is likely that secondary Aitken mode particles are formed by coagulation of ultrafine particles, by condensation and by liquid phase reactions. Primary sources that have very large emissions of Aitken mode particles are combustion processes. The accumulation mode covers the range between 0.1 and up to 2.5 μm in diameter [Seinfeld & Pandis, 2006] and they usually account for the substantial part of the aerosol mass. In the atmosphere, nucleation mode particles grow to accumulation mode particles primarily by coagulation and liquid phase reactions occurring in cloud droplets. They tend to have the longest lifetime in the atmosphere since the removal mechanisms that are effective for small and large particles, work inefficiently in this regime and causing particles to accumulate in the atmosphere [Seinfeld & Pandis, 2006].

The coarse mode includes particles $>2.5 \mu\text{m}$ [Seinfeld & Pandis, 2006]. Most particles in the coarse mode range are formed by mechanical processes, such as the erosion of the earth's crust (mineral dust), or the bursting bubbles on the ocean surface (sea spray). Due to their large size, coarse particles have a large sedimentation velocity and their lifetime in the atmosphere is reasonably short.

1.2. Emission sources and chemical composition

Aerosol concentration and composition vary dramatically since there are different natural and anthropogenic sources contributing to their formation, and also their medium and long-range transport mechanisms. The major PM_{10} and $\text{PM}_{2.5}$ components are sulfate, nitrate, ammonium, sodium, chloride, organic and elemental carbon, mineral dust and water. PM_{10} means particulate matter with an aerodynamic diameter $<10 \mu\text{m}$. On the same basis, $\text{PM}_{2.5}$ and PM_1 are defined [WHO Air Quality Guidelines Global Update 2005]. According to Zhang et al, (2007) organic compounds account for 18-70% of PM_1 measured in his study. The organic fraction can rise up to 90% in tropical forests [Kanakidou et al., 2005]. Figure 1.2 shows the variety in the composition of non-refractory organics, sulfate, nitrate, ammonium, and chloride PM_1 that was measured at different locations using an aerosol mass spectrometer (AMS) [Zhang et al., 2007].

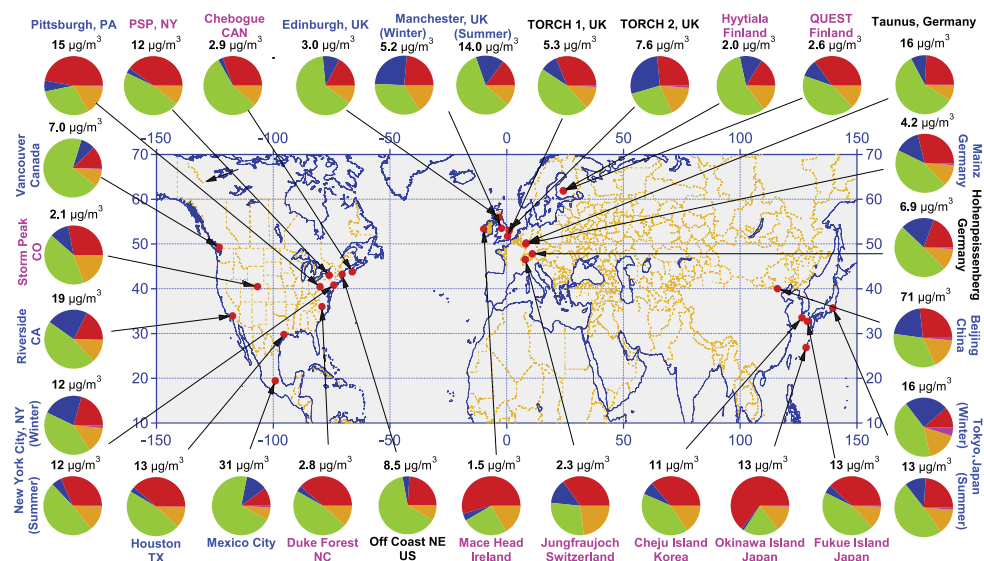


Figure 1.2: composition of non-refractory PM₁ collected at specific locations by AMS. The type of area the sample was collected from is indicated by the font color: Urban area (blue), <100 miles downwind of major cities (black), and rural/remote areas >100 miles downwind (pink). The chemical composition and average mass concentration are represented using the following color code: organics (green), sulfate (red), nitrate (blue), ammonium (orange), and chloride (purple). Adapted from Zhnag et al. (2007).

Natural particles originate mainly from sea spray, volcanic emission, and mineral dust from long-range transport or erosion processes, forest fires and biogenic sources. Primary particle fraction of sea spray is mainly constituted of sodium chloride, sulfates, and some organics especially during high biological activity seasons [O’Dowd et al., 2004]. The sea spray is generated by the breaking of waves in the coastal areas and producing bubble bursting on the ocean/marine surface [Warneck, 1987]. Sea spray primary particles undergo chemical processes in the atmosphere in which nitrate and sulfate could substitute chloride in the particles. This phenomenon is known as “chlorine depletion” [Zhao, 2008]. Volcanic emissions are sources of primary ash particles but also secondary sulfur compounds from SO₂ emission, although the contribution of such events to bulk particle mass levels in ambient air is generally limited. Crustal and mineral dust could be subject to regional variation as a function of the geology of the source areas, but in general they are composed of silicates, carbonates, aluminum, iron and metals in traces. They are originated by erosion processes, e.g. by the wind, or transported from desert regions (e.g. Saharan dust

events in south Europe). Forest fires are sources of both organic primary emission and gaseous precursors of particles. Some specific markers could trace the sources for biomass burning aerosols, mainly levoglucosan, mannosan, galactosan which are degradation products of lignin burning [Zhang, 2011; Reisen 2011]. Biogenic sources emit vegetal debris, pollen, spores which have sizes extending into the coarse mode and minor amounts of microorganisms (e.g. viruses, bacteria, fungi, protozoa or algae) contributing to particles in the size range $< 2 \mu\text{m}$. The natural secondary aerosol is constituted mainly of sulfate originated from the oxidation of SO_2 emitted by volcanoes and nitrate originated from the oxidation of NO_x (NO and NO_2) from soil transpiration and lightning and organic aerosols originated from organic gaseous precursors such as biogenic emissions of terpenes from large forest area.

In urban environments primary particles are emitted as a result of traffic-related combustion processes, house heating and industrial processes. Oxidation of SO_2 emitted by fossil fuel combustion and metal smelting [Charlson, 1992] produces sulphuric acid, which could be incorporated as it is or neutralized by ammonia or by reaction with calcium carbonate or sodium chloride. NO_x are emitted by traffic in urban environments and by some industrial processes. By oxidation of NO_x , nitric acid is formed, which may be neutralized and then incorporated into particles phase. Large agricultural areas, combustion of biomass and fossil fuels are important sources of organic gaseous precursors of anthropogenic secondary aerosol. These vapours are mainly emitted by gasoline evaporation (fugitive emission and combustion processes). Human activities may also generate anthropogenic bio-aerosols. Bacteria and fungi generated in solid waste recycling and composting plants [Marchand, 1995].

1.3. Human health effects

Several worldwide epidemiological and toxicological studies have proven that PM cause adverse health effects. A recent meta-analysis of epidemiological data and $\text{PM}_{2.5}$ concentration in Europe by that Clean Air For Europe (CAFE) depicted the estimated loss of life expectancy due to exposure to fine particulate matter (Figure 1.3) [Zimmermann 2011].

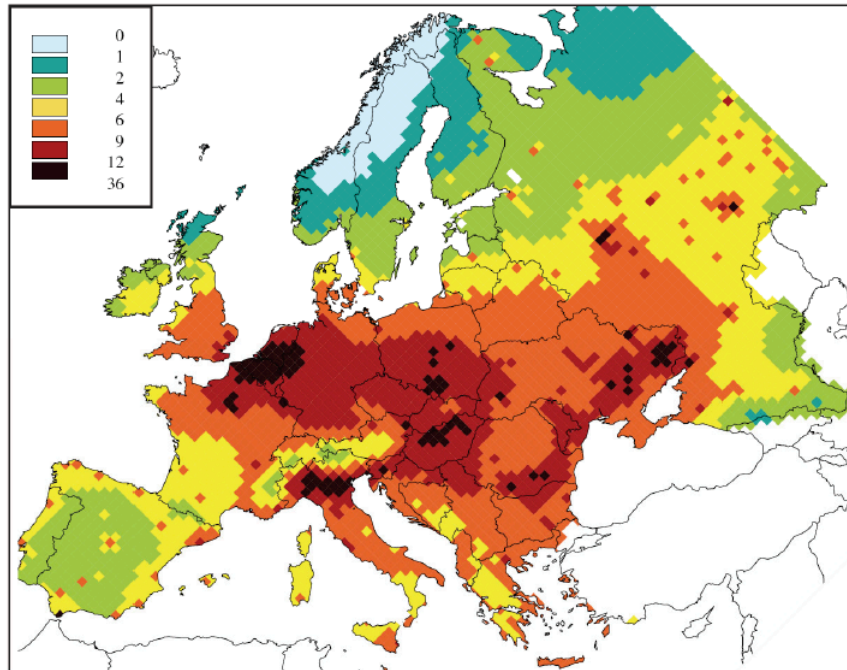


Figure 1.3: Loss of life expectancy (months) due to ambient aerosols (PM10) in Europe [CAFÉ, 2011].

A consistent increasing of cardiovascular and respiratory morbidity and mortality is currently associated to PM exposure [Nel 2005]. In order to prevent adverse health effects we need to understand which particle properties are important and related to them. Parameters potentially relevant for these adverse effects are particle size, and hygroscopicity [Pöschl 2005, Harrison and Yin, 2000].

Particle size is an important characteristic from a toxicological point of view. As the size of a particle decreases its surface to volume ratio increases, allowing a greater proportion of its atoms or molecules to be displayed on the surface, rather than inside the material, and the contact surface with lung tissues increases [Nel 2006]. Moreover, particle size is crucial for penetration and deposition efficiency into human lungs, with ultrafine particles ability to penetrate deep into the respiratory tract and reach alveoli, the small air sacks where the actual gas exchange takes place [Jaques & kim 2000; Sarangapani & Wexler 2000b]. Hygroscopicity determines the water uptake ability of particles and hence their size. The deposition rate of particles in the respiratory tract is very much depends on particle size and its water absorption potential [Sarangapani, 2000a; Löndahl et al., 2008].

1.4. The climate effects of aerosols

Aerosols in atmosphere impact climate in two main ways named direct and indirect effect. The direct effect refers to absorbing and scattering of solar radiation by aerosol particles whereas the indirect effects of aerosols is related to cloud formation and their lifetime.

1.4.1. The direct effect of aerosols

The direct effect of aerosols is related to their ability to absorb and scatter incoming short-wave solar radiation and outgoing long wave thermal radiation and directly affect the albedo of the Earth [Haywood & Boucher, 2000]. The intensity of light scattered by aerosols is strongly dependent on the size, and refractive index of the particle, thus the hygroscopicity of the particles is the major factor determining their direct radiative impact. The composition of the particle is also plays a role. For example, black carbon (BC) or soot has a strong absorption of solar radiation and tends to generate a positive radiative forcing. In recent years, a new class of organic carbons that absorb solar radiation were identified and known as brown carbon (BrC). They have a high wavelength dependence absorption, which decreases going from UV to visible region (see chapter 3). Other particles than soot, BrC, and to some extent mineral dust, scatter a significant fraction of the incoming solar radiation back to space and have a net cooling effect. According to the latest report by the Intergovernmental Panel on Climate change (IPCC), the total direct effect of anthropogenic aerosol particles is about -0.27 W/m^2 (-0.77 to 0.23 W/m^2) as indicated on Figure 1.4.

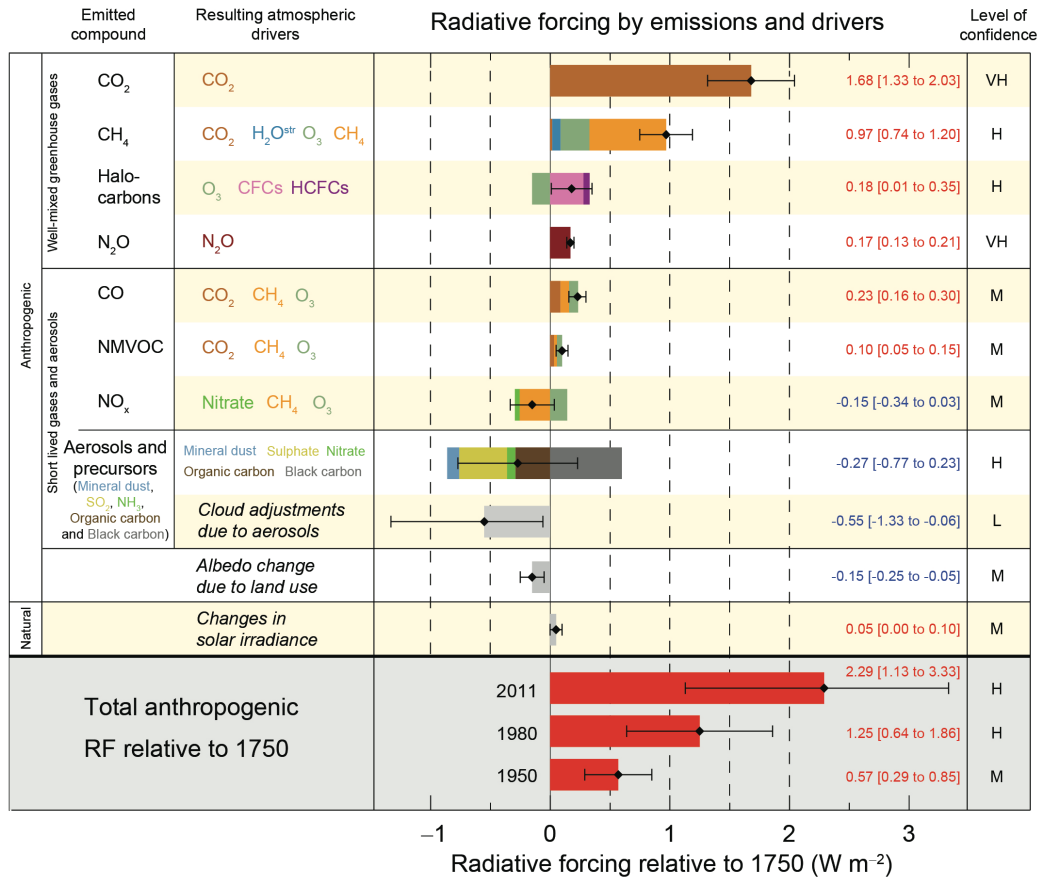


Figure 1.4: Radiative forcing of several environmental effects of our climate system between 1750 and 2011 [IPPC, 2013]

1.4.2. The indirect effect of aerosols

The indirect effect of aerosols includes their impact on cloud microphysics, which includes changes in clouds' radiative properties, their frequency and their lifetimes. Aerosols act as nuclei on which water vapor condenses. When the number concentration of cloud condensation nuclei (CCN) during cloud formation increases, the generated clouds will contain a higher number of aerosol particles but of smaller size. As such clouds exert higher albedo, which results in a negative radiative forcing and a net cooling effect. This is referred to as the first indirect, the cloud-albedo, or the Twomey effect. It is believed that Anthropogenic activities are responsible for an increase in the number concentration of CCN. The most recent IPCC assessment, states that the first indirect effect accounts for a radiative forcing of -0.55 W/m^2

(Figure 1.4), with an uncertainty ranging from -1.33 W/m^2 to -0.06 W/m^2 [IPCC, 2013].

The second indirect effect of aerosols is related to the lifetime of clouds composed of smaller cloud droplets [Albrecht, 1989]. These clouds are believed to have a longer lifetime, as they are not heavy enough to promote drizzle. This effect is complicated and climate models have not yet been able to estimate the magnitude of its impact on climate.

1.5. Hygroscopic behavior of atmospheric aerosols

Hygroscopicity is defined as the ability of particles to absorb or release water as relative humidity (RH) is changing in the surrounding. The hygroscopic growth of atmospheric aerosols plays an important role in the Earth's radiation budget and atmospheric chemistry. The uptake of water by particles affects both their optical properties (direct effect) and their activation into cloud condensation nuclei (CCN), (aerosol indirect effect). The interaction of aerosol particles with water vapor in ambient air determines the size of the particles at the relative humidities prevailing in the atmosphere and thus their direct effect on climate. It also influences cloud properties by determining the concentration of cloud droplets, and with this cloud albedo and cloud lifetime. According to IPCC report in 2013, although our level of understanding with respect to the direct effect has improved, the indirect effects still count for the largest cause of uncertainty when it comes to climate change estimation (Figure 1.4). Furthermore, hygroscopic growth of aerosols impacts the rate of atmospheric wet and dry deposition, human health, and visibility [Broday and Georgopoulos, 2001; Schroeter et al., 2001; Chan et al., 2002].

At very low RH, pure inorganic salt aerosol particles are in a solid state. As RH is increasing in the ambient air, the particles remain solid until RH increases to a specific threshold value known as deliquescence RH (DRH). At DRH, which is a characteristic value for a specific compound the solid particle spontaneously absorbs water from the gas phase and becomes a saturated aqueous solution and its size increases abruptly [Martin, 2000]. Further increase of RH results in additional condensation of water molecules onto the salt solution to maintain thermodynamic

equilibrium between the condensed and gas phase. On the other hand, as the RH is decreased, water evaporates from the salt solution but usually the solution does not crystallize at DRH and remains as a supersaturated solution until much lower RH referred to as efflorescence relative humidity (ERH) when it loses its water to the gas phase and becomes crystallized [Richardson and Spann 1984; Cohen et al. 1987]). This hysteresis behavior is quite common for some inorganic salts including ammonium sulfate (AS) and sodium chloride. Fig. 1.5 (a) illustrates the phase transition of pure AS and its hysteresis behavior.

The chemical composition of a particle determines its hygroscopic properties. Atmospheric particles are comprised of organic and inorganic matters [Middlebrook et al., 1998; Murphy et al., 1998]. Although the inorganic components of atmospheric aerosols have been investigated thoroughly in the past decades [Tang, 1976; Tang and Munkelwitz, 1994; Weis and Ewing, 1999; Colberg et al., 2003], water uptake properties and phase transitions of organic carbon (OC) in particles display considerable amount of uncertainty [Brooks et al., 2004; Intergovernmental Panel on Climate Change (IPCC), 2007; Jimenez et al., 2009]. The fact that 15- 55% of the organic carbon mass in the aerosols composed of water-soluble organic carbon (WSOC) [Graham et al., 2002; Mayol-Bracero et al., 2002; Cavalli et al., 2004; Decesari et al., 2005] indicates that these species may play a significant role on the hygroscopic behavior of atmospheric aerosols. Unlike the inorganic fraction, the chemical composition of the organic matter in the atmosphere is highly complex with a large fraction not yet identified [Decesari et al., 2006; Goldstein and Galbally, 2007]. Previous studies that investigated the physical state of various dicarboxylic acids concluded that the transition properties of these pure organic particles significantly depend on their chemical composition [Braban et al., 2003; Marcolli et al., 2004a; Parsons et al., 2004; Zardini et al., 2008]. Organic constituents of the aerosol without hysteresis behaviour can contribute to an uptake of water at lower RH than the DRH of inorganic salts [Dick et al., 2000]. Such complex mixtures can remain in the liquid state and exchange water with the gas phase at lower RH's [Marcolli et al., 2004].

Since single-particle measurements show that organic and inorganic constituents of the aerosols are indeed internally mixed [Zhang et al., 1993; Murphy & Thomson, 1997; Middlebrook & Murphy, 1998; Lee et al., 2002; Lee et al., 2003], Depending on the organic to inorganic mass ratio (OIR), and the interactions between organic

and inorganic substances within an aerosol particle, the DRH and ERH of atmospheric mixed particles may be drastically affected. In many cases, it's been shown that the addition of organic will decrease the DRH and ERH of the inorganic salt in the mixed inorganic/organic particle [Marcolli et al., 2004; Braban and Abbatt, 2004; Parsons et al., 2004a; Bertram et al., 2011; Smith et al., 2012; Song et al., 2013]. Figure 1.5 illustrates the change in hygroscopic behavior of pure AS (Fig. 1.5 a) as it mixes in with citric acid at different molar ratio (1.5 b-d). The hygroscopic growth of pure citric acid is also shown in Fig. 1.5 e. [Zardini et al., 2008].

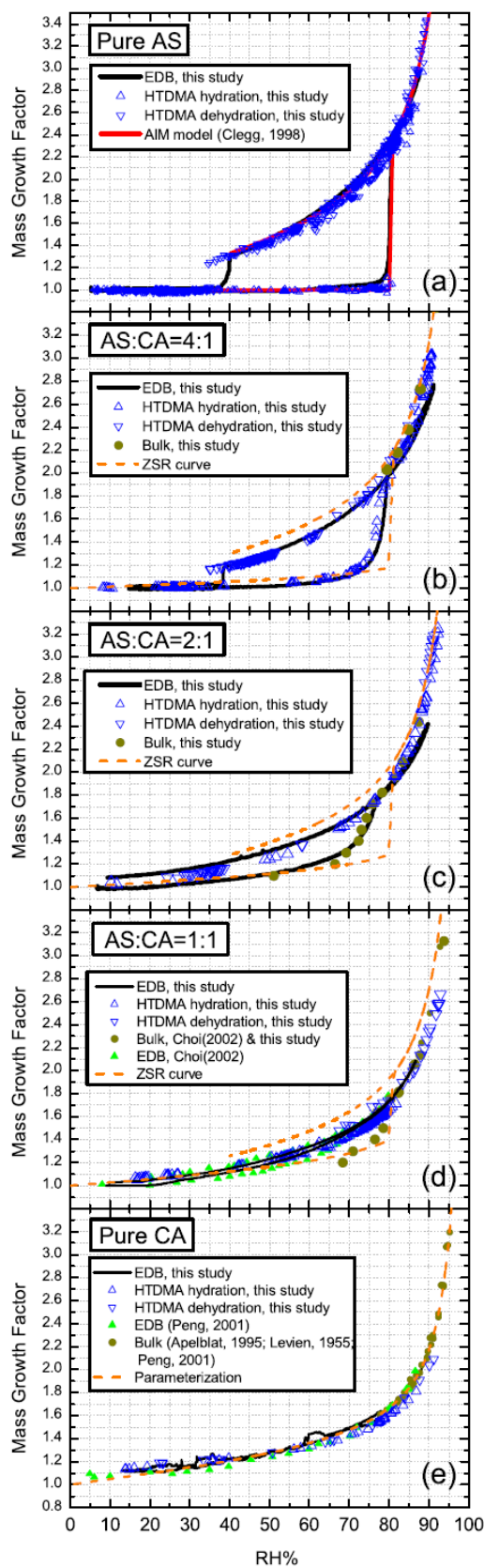


Figure 1.5: Hygroscopicity behavior of

- (a) pure ammonium sulfate (AS),
- (b) mixture of AS and citric acid (molar ratio = (4:1),
- (c) mixture of AS and citric acid (molar ratio = (2:1),
- (d) mixture of AS and citric acid (molar ratio = (1:1),
- and
- (e) pure citric acid particles.

Measurements are taken from particles in an electrodynamic balance (EDB) (black solid line), and from a hygroscopicity tandem differential mobility analyzer (HTDMA) (blue triangle). Source: Zardini et al. (2008).

1.6. Liquid-Liquid phase separation

As discussed above, the physical state of aerosol particles depends on their chemical composition, ambient relative humidity (RH) and temperature [Kwamena et al., 2010; Reid et al., 2011; Krieger et al., 2012]. Tropospheric aerosols are composed of inorganic salts and acids, organic compounds and water and are mostly internally mixed [Lee et al., 2002; Marcolli et al., 2004; Murphy et al., 2006]. When aerosol particles are exposed to humidity fluctuations in the atmosphere, they may undergo phase transitions such as deliquescence, and efflorescence [e.g., Martin, 2000; Clegg et al., 2001; Brooks et al., 2002; Pankow, 2003; Parsons et al., 2004; Erdakos et al., 2006; Marcolli and Krieger, 2006; Anttila et al., 2007; Ciobanu et al., 2009; Prisle et al., 2010; Zuend et al., 2010; Smith et al., 2011]. Experiments and modeling studies on model systems for mixed organic/inorganic aerosols have shown that deliquesced aerosols can exist not only as one-phase system containing organics and inorganics together, but often as two-phase systems consisting of a predominantly organic and a predominantly inorganic aqueous phase [Pankow, 2003; Marcolli and Krieger, 2006; Ciobanu et al., 2009a,b; Bertram et al., 2011; Krieger et al., 2012]. This phenomenon is known as liquid-liquid phase separation (LLPS). The non-ideal nature of the mixed organic/inorganic compounds prevents them to form a ternary solution that is miscible at all compositions and all temperatures. As RH decreases, the less polar organic material that has less affinity for water will be driven out of the rich-water phase and forms a liquid phase with less water content. This leads to a miscibility gap, which minimizes the free energy of the system.

This phenomenon can be explained through salting-out effects, where the presence of a highly polar salt can reduce the solubility of less polar organic components in water and push them away from the water rich phase [Marcolli and Krieger, 2006; Ciobanu et al., 2009; Zuend et al., 2010; Bertram et al., 2011; Zuend and Seinfeld, 2012]. For theoretical mechanisms behind the formation of LLPS, see chapter 2.

There is no direct measurement technique available at the present moment that could observe LLPS in ambient aerosols but all recent laboratory studies that were conducted with model mixtures representing tropospheric aerosols [Ciobanu et al., 2009a,b; Bertram, et al., 2011; Song et al., 2012a; Song et al., 2012b], secondary organic aerosol from smog chamber experiments [Smith et al., 2012] and from field samples [You et al., 2012] suggest LLPS is indeed a common phenomenon in mixed organic/inorganic particles.

1.7. Morphology of mixed aerosol particles

Below a critical relative humidity when phase separation occurs (often termed SRH), the two phases in the particle may adopt different morphologies, such as core-shell, partially engulfed, or the formation of multiple inorganic inclusions in the organic phase (Figure 1.6).

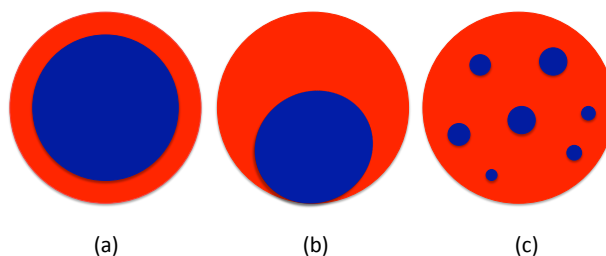


Figure 1.6: Schematic diagram of major possible morphologies of mixed organic/AS/H₂O particles after the onset of LLPS. Navy blue and red color represent AS-rich phase and organic-rich phase respectively. (a) Concentric core-shell, (b) Partially engulfed, and (c) AS inclusions in organic/H₂O mixtures

A core-shell configuration, in which the inorganic phase is fully enclosed by the more viscous organic phase, may affect heterogeneous chemistry especially the

heterogeneous hydrolysis of N_2O_5 [Folkers et al., 2003; Thornton and Abbatt, 2005; Anttila et al., 2006; McNeill et al., 2006; Cosman and Bertram, 2008; Riemer et al., 2009; Escoreia et al., 2010; Gaston et al., 2014; Gaston et al. 2016]. According to Folkers et al. (2003), the reaction probability for the hydrolysis of N_2O_5 can be reduced by about a factor of five on a phase-separated particle exhibiting core-shell morphology (organic coating around inorganic core).

LLPS could also impact the hygroscopicity of mixed particles and alter their radiative properties [Martin et al., 2004; Wang et al., 2008a]. The impact of LLPS on optical properties of mixed aerosols will be further discussed in chapter 6.

Furthermore, phase separation could impact the gas-to-particle partitioning of semi-volatile organic compounds [Seinfeld et al., 2001; Chang and Pankow, 2006; Zuend et al., 2010; Shiraiwa et al., 2013] and change the ice-nucleation efficiency of atmospheric particles depending on the physical state of their organic shell [Schill and Tolbert, 2013].

1.8. Motivations and objectives of the thesis

Prior to this thesis, studies only investigated the morphology of different inorganic/organic mixed systems at or near room temperature. Examinations of changes in morphology of the particles at lower temperature that are more representative of tropospheric conditions were missing. LLPS was mainly viewed from a thermodynamic perspective and the kinetic limitations that might prevent the formation of phases separated mixtures at lower temperatures were not taken into account. One of the primary objectives of this thesis was to investigate the change in morphology of mixed particles at lower temperatures and at different drying rates for a ternary model system consist of ammonium sulfate (AS)/carminic acid (CA)/ H_2O .

In addition to morphology studies, available thermodynamic data were combined with the information obtained from particle analysis software to infer AS diffusivity from the measured growth rate of inorganic inclusions after nucleation and quantitatively estimate the diffusion constant of AS ions in the CA/ H_2O matrix enclosing the AS inclusions. The resulting AS diffusivities were compared with the AS diffusivity constants derived from estimating the viscosity of the matrix from a coalescence model and applying Stokes-Einstein relationship.

Furthermore, The impact of LLPS on the optical properties of mixed aerosol particles containing AS and brown carbon was investigated using both a concentric and eccentric core-shell Mie code compare to the classical approach that treats mixed particles either as homogenous or concentric core-shell. The extent at which LLPS can impact the radiative properties of particles with absorbing organic carbon in the outer shell over UV-VIS region of the solar spectrum was estimated.

Chapter 2

2. Theoretical Aspects of Phase transition

2.1. Water Activity (a_w)

The ability of aerosol particles to uptake water (hygroscopicity) and eventually grow to form cloud droplets are important atmospheric processes affecting the hydrological cycle and global climate [Lohmann, U.; Feichter, 2005; IPCC, 2007]. As mentioned before, the water content of atmospheric particles also affects the ability of particles to absorb and scatter light [Haywood, and Boucher, 2000] as well as the partitioning of semi-volatile molecules between gas and particle phases in the atmosphere [Pankow, and Chang, 2008]. The water contents of particles and droplets in the atmosphere span a wide range. In some particles, such as freshly emitted soot, the water content can be very small, whereas cloud droplets are highly dilute aqueous solutions. In addition to water, particles in the atmosphere contain a multitude of organic as well as inorganic components [Saxena, and Hildemann, 1996; Cass et al., 2000]. Most of the water associated with atmospheric particles is chemically unbound [Pilinis et al., 1989]. Understanding the interactions between liquid water molecules and inorganic and organic aerosol particles as well as the interactions between aerosol particles and water in the surrounding gas phase are important challenges in the field of atmospheric aerosol science [Kanakidou et al. 2005].

Water activity is a key parameter in the theoretical description of these processes. The water activity (a_w) of an aerosol solution is defined as the ratio of the equilibrium water vapor pressure (P_{H_2O}) over the solution to the equilibrium vapor pressure of

pure water ($P_{H_2O}^\circ$) at the same temperature [Seinfeld and Pandis, 1998]:

$$a_w = \frac{P_{H_2O}(T)}{P_{H_2O}^\circ(T)} \quad \text{Eq (2.1)}$$

Water activity is the measure of the amount of available or “unbound” water molecules in a system [Caurie, 1983].

The amount of water vapor in the air is referred to as relative humidity and defined as the ratio of partial vapor pressure of water (P_{H_2O}) to its saturation vapor pressure ($P_{H_2O}^\circ$) at a given temperature and is normally expressed in percentage:

$$RH = \frac{P_{H_2O}(T)}{P_{H_2O}^\circ(T)} \times 100\% \quad \text{Eq (2.2)}$$

2.2. Deliquescence and Efflorescence

Water is the most important component of atmospheric aerosols. The majority of the water molecules associated with atmospheric aerosols are not chemically bounded.

At low relative humidities, atmospheric particles containing inorganic salts are in solid state. As RH increases, the particle uptakes water from surrounding and reaches a point where it transforms to a saturated aqueous droplet. The RH at which the phase transition from solid to liquid occurs is known as *deliquescence relative humidity* (DRH) and is characteristic for each composition and varies only with temperature [Seinfeld and Pandis, 2006]. This is important to note that this is only true for the majority of binary systems. For the multicomponent systems we observe a continuous water uptake until the salt with highest DRH in the binary system gets dissolved, the growth curve will experience a kink. Figure 1.5 illustrates this phenomenon quite clearly.

The concentration of an aqueous solution of a salt at the deliquescence point is the same as the solubility of the salt.

On the other hand, as ambient RH decreases, water evaporates from the surface of the particle but the shrinking droplet does not crystallize at DRH. Instead it remains as a

supersaturated aqueous droplet up until much lower RH where efflorescence (crystallization) occurs. This hysteresis behavior of deliquescence and efflorescence is a characteristic feature of most common inorganic salts and their mixtures with different organic compounds.

The phase transition of aerosol droplets (particles) can be explained by the change in Gibbs free energy during the humidity cycle.

When the relative humidity is lower than the DRH of a salt, the Gibbs free energy is lower for the solid salt than its corresponding aqueous solution and the salt is promoted to stay in the solid form (state). As relative humidity increases, the Gibbs free energy of the solution decreases and at DRH it equals the energy of the corresponding solid. As relative humidity increases further, the solution becomes the state with the lowest energy and the particle uptakes water spontaneously to form a saturated salt solution. The transition to the deliquescence point is followed by a substantial increase in mass of the particle and the solution state remains the favored state for higher RHs (Seinfeld and Pandis, 2006).

As the RH decreases, the energy of the solution and the solid state becomes equal once again at DRH. However, in order for the particle to form a solid as RH decreases below DRH, all the water has to evaporate and an energy barrier has to overcome to form the critical nuclei that would eventually initiate crystallization. Therefore, the particle remains as liquid as RH keeps decreasing and water continues to evaporate and form a supersaturated solution. This metastable supersaturated solution will remain to exist until it reaches a critical supersaturation, where the crystallization occurs at a RH much lower than DRH. The relative humidity at which crystallization (nucleation) takes place is known as *efflorescence relative humidity* (ERH). The change in Gibbs free energy as a function of RH is depicted in figure 2.1.

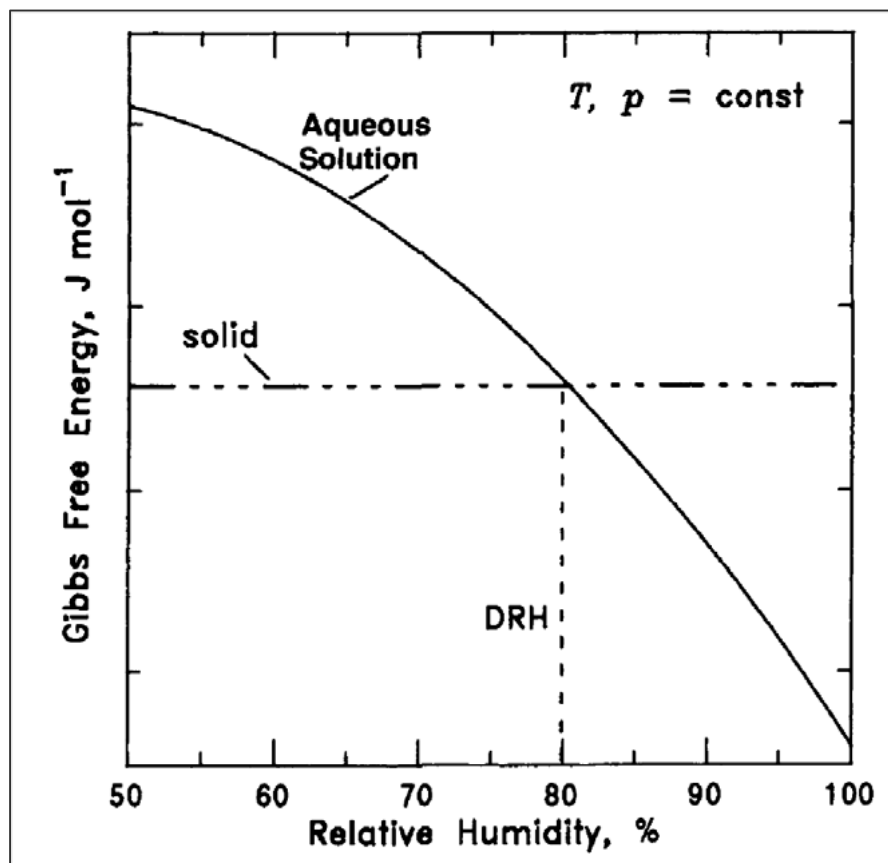


Figure 2.1: Gibbs free energy of a solid salt and its corresponding (binary) aqueous solution as a function of RH at constant pressure and temperature. At DRH, both solid and liquid states are equal in energies. Source: Seinfeld and Pandis (2006).

It is important to note that not all aerosol particles exhibit deliquescent/efflorescent behavior. Species like H_2SO_4 are highly hygroscopic and their water content changes smoothly as RH varies in the atmosphere without experiencing any deliquescence. Instead they tend to form a number of crystalline hydrates ($\text{H}_2\text{SO}_4 \cdot n\text{H}_2\text{O}$). Some salts including NaNO_3 , and NH_4NO_3 do not exhibit efflorescence even if they exposed to 0% RH.

DRH and ERH of some inorganic salts and electrolyte solutions that are common species of ambient aerosols are given in Table 2.1:

Salt	DRH (%)	ERH (%)
KCl	84.2	59
Na ₂ SO ₄	84.2	56
NH ₄ Cl	80.0	45
(NH ₄) ₂ SO ₄	80.0	35
NaCl	75.3	43
NaNO ₃	74.3	Not observed
NH ₄ NO ₃	61.8	Not observed

Table 2.1: DRH and ERH of Electrolyte solutions at 298 K. “Not observed” means that crystallization was not reached for the corresponding particle as RH lowered down to 0%.

Sources: Tang (1980), Tang and Munkelwitz (1993), and Martin (2000).

2.3. Mechanisms of liquid-liquid phase separation

The two main mechanisms that lead to the formation of liquid-liquid phase separation (LLPS) are “spinodal decomposition” and “nucleation and growth”. The phase separation due to spinodal decomposition is much more defined, and occurs uniformly throughout the particle rather than at discrete nucleation sites. Each process will be explained in the followings sections.

2.3.1. Spinodal decomposition

A one-phase solution can be decomposed into two liquid phases via spinodal decomposition. During spinodal decomposition, spontaneous fluctuations in concentration cause its transition to a stable second phase without it being necessary to overcome the energy barrier corresponding to creation of an interface in order to form a nucleus.

This process initiates by the instantaneous appearance of rapidly growing inclusions dispersed all over the solution volume and their subsequent aggregation

(coalescence). According to figure 2.2, Spinodal decomposition occurs when the solution is in the unstable region below the spinodal curve (dashed line in fig 2.2).

Since there is no thermodynamic barrier to the reaction inside of the spinodal region, the decomposition is determined merely by *diffusion*. Thus, the process can be treated purely as a diffusion problem, and many of the characteristics of the decomposition can be described by an *approximate analytical solution* to the general diffusion equation.

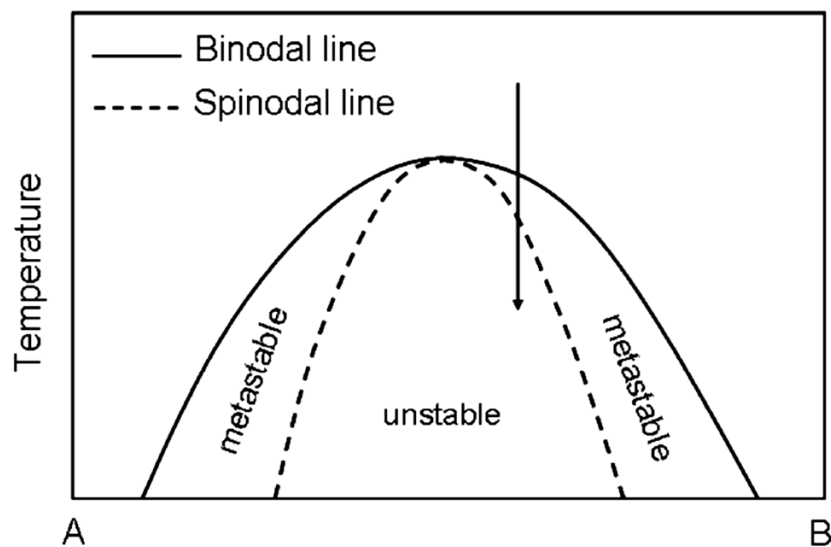


Figure 2.2: Phase diagram of two partially miscible components (A and B). The arrow points out to the unstable region where spinodal decomposition could take place. Adapted from Papon et al. (1999).

2.3.2. Nucleation and growth

LLPS may also occur by nucleation and growth, when a system has reached the metastable region shown in (Figure 2.2). For nucleation and growth to occur, a transition energy barrier has to overcome. When concentration fluctuations reach a critical amplitude and size, a critical nucleus can form and overcome this nucleation barrier. The creation of a nucleus implies the formation of an interface at the boundaries of a new phase. For the formation of the second aqueous phase, the free energy change $\Delta G(r)$ is balanced by the two competitive factors, the volume free

energy and interfacial energy due to formation of second phase, just as depicted in the diagram below (Figure 2.3).

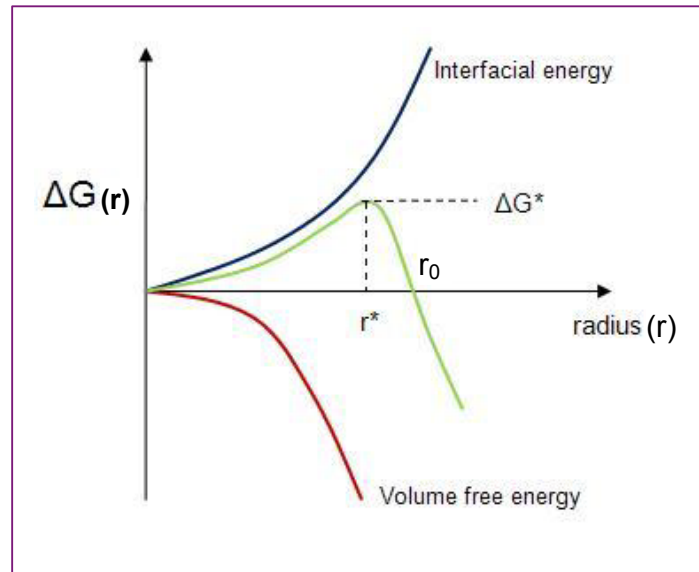


Figure 2.3: Thermodynamics of nucleation and growth: nucleation initiates from the free molecules to form small inclusions (nucleus). As the inclusions grow, $\Delta G(r)$ increases mainly due to the rapid increase in surface energy, implying that nucleus growth is not thermodynamically favorable in this regime. Once some of the inclusions reach the size of r^* and pass the barrier of $\Delta G(r^*)$, further growth of inclusions will lead to decrease in $\Delta G(r)$, a tendency favorable for the continuous growth, although $\Delta G(r)$ in this regime before reaching the size of r_0 is still > 0 (not thermodynamically favorable). After passing r_0 , ΔG will become more negative, and the growth of nucleus will be highly favored and eventually lead to formation of second aqueous phase ($r \rightarrow \infty$).

During nucleation and growth mechanism, the concentration of the second phase (α_2 in fig 2.4 (a)) reaches the critical amplitude (C_2 in figure 2.4), and then it grows in time by diffusion.

The nucleus of the second phase might appear anywhere in the volume of the sample. The nucleuses are expected to exist as spherical inclusions since that would minimize the surface for a fixed volume when both phases are present as liquids. Later in the process, the inclusions may come in contact with each other either by sheer growth or by Brownian diffusion and coalesce. Nucleation and growth mechanism evolves less rapidly over time when compared to spinodal decomposition.

Nucleation and growth is a dominant mechanism of LLPS when the system consists

of a major volume (phase) and a minor one. This can be observed from Fig. 2.4, where the spinodal curve meets the bimodal curve (the critical point) and both components have relatively equal concentrations. While nucleation and growth process requires that the two components have different initial concentrations (vertical downward arrow in figure 2.4). The importance of the mixture's initial concentration (C_B) for the formation of the second phase via nucleation and growth and spinodal decomposition mechanism is illustrated in Fig. 2.4 (a), and (b) respectively [Papon, 1999].

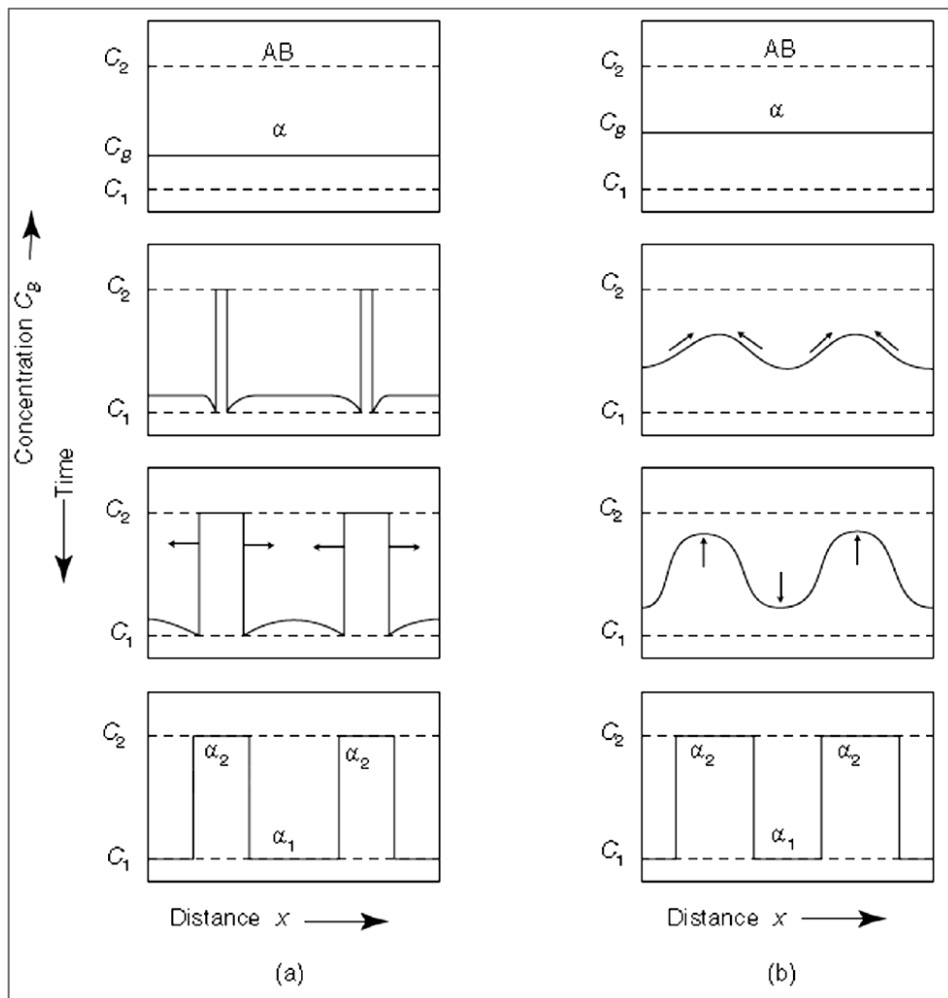


Figure 2.4: Phase separation mechanisms: nucleation and growth (a) and spinodal decomposition (b) for a binary mixture AB with initial concentration C_B . The two phases α_1 and α_2 are formed from the initial homogenous mixture α . Via nucleation and growth mechanism (a), the inclusions are growing over time and during spinodal decomposition (b) the concentration fluctuations increase in the mixture and give rise to the second phase. C_1 and C_2 are the final concentrations for α_1 and α_2 respectively. Source: Papon (1999).

Chapter 3

3. Optical properties of aerosols

As light propagates through the air, it may hit a particle. Depending on the size, shape and composition of the particle, the light can be either absorbed or scattered. Different approximations were developed to describe the aftermath of light-particle interaction. These theories derived from the solution to Maxwell equation and calculate different optical parameters [Van de Hulst, 1957]. The optical properties (absorption and scattering cross-section) of particle significantly depend on the size of the particle.

For particles that are much smaller than the wavelength of the incident light (i.e particles of diameter $\leq 0.02 \mu\text{m}$) Rayleigh approximation is used to properly predict their scattering and absorption. In this regime, the scattering is isotropic quite independent of the shape of the particle.

For particles with diameter much larger than the wavelength of light (i.e particles of diameter $> 50 \mu\text{m}$), geometrical optics is used which applies the classical laws of reflection, refraction, and diffraction.

For the spherical particles with diameter in between, but in particular for those as large as the the wavelength of radiation, Mie theory is used to predict absorption and scattering of spherical particles, using complex refractive index, size of the particles and the wavelength of incident light as input parameters. Most atmospheric aerosol particles lie in the size regime ($20 \text{ nm} \geq \text{particle diameter} \leq 50 \mu\text{m}$) where Mie-theory applies.

3.1. Optical parameters

3.1.1 Mie theory

Mie theory was developed by Gustav Mie in 1908 [Mie, 1908] and solves Maxwell's equations for the problem of a light interacting with a dielectric sphere. It describes the change in internal and scattered electromagnetic fields of a spherical particle as it interacts with the electromagnetic field of an incident light and gives the intensity of the scattered light. The intensity of the scattered light, which varies with scattering angle, and the amount of absorption by the sphere, depends on the complex refractive index of the spherical particle, and the ratio of particle size to the wavelength of the incident light. Therefore, the particle size parameter, x , is used to describe the ratio of the particle size to the wavelength of the incident light [Barber and Hill, 1990]:

$$x = \frac{2\pi r}{\lambda}$$

Where r is the particle radius, and λ is the wavelength of the incident light.

3.1.2. Absorption and scattering of spherical particles

When a beam of light hits a particle, electric charges in the particle get excited and start oscillating which result in emitting the radiation energy in all directions (scattering) and convert a part of the incident radiation into thermal energy (absorption). The net irradiance (I_{ext}) removed from an incident beam of light irradiance (I_0), by a single particle via scattering and absorption is referred to as extinction and is given by the following equation:

$$I_{\text{ext}} = I_0 \sigma_{\text{ext}}$$

Where, σ_{ext} is the optical extinction cross-section and can be defined as the sum of the individual absorption and scattering cross-sections [Van de Hulst, 1957]:

$$\sigma_{\text{ext}} = \sigma_{\text{sca}} + \sigma_{\text{abs}}$$

Where, σ_{sca} and σ_{abs} represent scattering and absorption cross-sections, respectively. Mie theory allows calculating the optical efficiencies of a sphere as a function of size parameter and refractive index. The extinction efficiency, Q_{ext} , is expressed as the ratio of the cross-section for light extinction, σ_{ext} , to the geometrical cross-section of the particle, $\sigma_{geometric}$:

$$Q_{ext} = \frac{\sigma_{ext}}{\sigma_{geometric}}$$

For spherical particles with radius r , $\sigma_{geometric} = \pi r^2$.

The total extinction efficiency is the sum of scattering and absorption efficiencies. [Bohren and Huffman, 2008]:

$$Q_{ext} = Q_{sca} + Q_{abs}$$

Another quantity that is important for climate modeling and remote sensing is called single scattering albedo (SSA), ω . For a single particle, SSA describes the ratio of the scattering cross section to the total light extinction cross-section [Reid and Mitchem, 2006; Moise et al., 2015]:

$$\omega = \frac{\sigma_{sca}}{\sigma_{ext}}$$

ω is dependent not just on the composition but also on the particle size, hence it allows to investigate the impact of particle size on the optical properties and radiative forcing of aerosols. There is a critical single scattering albedo (ω^*) that determines the cooling or warming effect of the aerosol layer such that for $\omega < \omega^*$, the forcing is positive. ω^* depends on the up-scatter fraction ($\beta(\theta)$) and the ground albedo. $\beta(\theta)$ is the fraction of light that is scattered by an aerosol into the upward hemisphere relative to local horizon and is related to radiative forcing by aerosol single scattering [Wiscombe and Grams, 1976]. $\beta(\theta)$ depends on the solar zenith angle (SZA) as well as on the angular distribution of the light scattering by the aerosol (phase function). The importance of SSA and the up-scatter fraction for radiative forcing of single aerosol layer will be discussed in chapter 6.

All the optical properties mentioned here including σ , Q , and ω depend on the particle size, the wavelength of the incident light, and the complex refractive index of the surrounding medium and the complex refractive index (RI) of the particle.. The refractive index (RI) of the particle is a complex quantity given by:

$$N = n + ik$$

Where n is the real part of the refractive index and is responsible for the scattering properties of the particle while k is the imaginary part of the refractive index and dictates absorption. Complex refractive index is the only intrinsic optical property of a particle; hence knowing the value of N is crucial for accurate modeling of the atmospheric aerosols using Mie-code.

Particle morphology will affect the scattering and absorption of particles. In chapter 6, we performed these calculations for homogenous and particles adopting concentric core-shell morphology, using a modified version of Mie-code developed by Kaiser & Schweiger (1993). In addition, the eccentric core-shell Mie-code by Mackowski [Mackowski and Miscchenko, 1996] was employed to calculate the optical efficiencies of particles exhibiting eccentric core-shell configuration. Using the refractive index of a compound and the size parameter, the absorption, scattering, and extinction efficiencies can be calculated.

3.2. Light absorbing material in the atmosphere

The direct effect of aerosols refers to the direct absorption and scattering of solar and terrestrial radiation by aerosols. Most organic aerosols (OA) can be characterized as transparent since they efficiently scatter visible light. However, a major and highly variable part of carbonaceous and organic aerosols absorbs radiation [Satheesh and Moorthy, 2005; Bond and Bergstrom, 2006; Yu et al., 2006; Moosmueller et al., 2009; Bond et al., 2013]. It's been known for quite a long time that black carbon (BC) is the main light-absorbing agent in the atmosphere covering a broad range of solar spectrum from ultraviolet (UV) all the way into infrared (IR). BC is a collection

of soot-like particulates formed primarily by fossil fuel combustion and biomass burning [Bond et al., 2013].

Some type of mineral dust particles such as calcium carbonate also absorb solar radiation but it is still unclear whether they contribute to the net cooling or warming of climate [Veghte and Freedman, 2012].

Most organic carbon (OC) compounds are relatively transparent to visible light (400–700 nm) but in recent years, a class of OC was identified that can efficiently absorb radiation in the near-UV (300–400 nm) and less significantly in the visible regions [Andreae and Gelencser, 2006; Bond and Bergstrom, 2006; Ramanathan et al., 2007; Feng et al., 2013; Moise et al., 2015; Laskin et al., 2015; Shiraiwa et al., 2017] of the solar spectrum. This absorbing part of OA is referred to as “brown carbon” (BrC).

In addition to their direct effects on radiation, BC and BrC can facilitate water evaporation and cloud dispersion by absorbing light inside cloud droplets and compensate for the indirect cooling effect of aerosols [Hansen et al., 1997].

Brown carbon is often a by-product of biomass burning but its exact formation mechanism is not very well understood. Early studies identified primary emissions as the main source of BrC formation [Andreae and Crutzen, 1997; Bond, 2001; Ramanathan et al., 2007]. However, in recent years scientists attribute BrC to the secondary organic aerosols (SOA) that can form through oxidation of volatile organic compounds (VOCs) present within biomass smoke [De Haan et al., 2011; Nguyen et al., 2012; Lee et al., 2013; Powelson et al., 2014; Drozd and McNeil, 2014; Laskin et al., 2015; Costabile et al., 2016; Tang et al., 2016; Shiraiwa et al., 2017].

BrC in aerosols are commonly classified on the basis of their water solubility. Water Soluble Organic Carbon (WSOC) dominates atmospheric organic matter [Andreae and Gelencser, 2006; Ramanathan et al., 2007; Feng et al., 2013]. Between 20 and 70 wt% of the WSOC fraction is composed of high molecular weight and multifunctional compounds containing aromatic, phenolic, and acidic functional groups [Hansen et al., 1997; Poschl, 2005; Moosmueller et al., 2011; Wang, 2011; Bond, 2011; Ma et al., 2012; Lack and Langridge, 2013]. These multifunctional aerosol compounds resemble Humic Substances (HS) from terrestrial and aquatic sources since both are either water-soluble or can form suspended colloidal structures in atmospheric water [Graber and Rudich, 2006; Salma et al., 2008]. Therefore they have been called

Humic-Like Substances (HULIS). A major fraction of BrC in the atmosphere could compose of HULIS-like material [Andreae and Gelencser, 2006; Graber and Rudich, 2006]. However, the optical properties of HULIS material are not well understood, mostly due to difficulties in sampling and extraction of atmospheric HULIS for detailed laboratory measurements. The lack of atmospheric HULIS suggest the use of proxies that are commercially made HS from aquatic and terrestrial sources. A common model mixture used in laboratory studies is Suwannee River Fulvic Acid (SRFA) [Graber and Rudich, 2006].

Unlike BC, the chemical structure and optical properties of BrC are quite unknown. The complex molecular composition of light-absorbing OC and high level of uncertainty regarding their relative concentrations make the characterization of their molecular composition quite challenging and hence, complicates the determination of their optical properties. It is yet not clear if typical BrC is composed of a few strong chromophores or it is a mixture of a large number of weak chromophores. The latter case would be more consistent with the featureless UV–VIS spectra of BrC observed in the majority of field studies. However, UV–VIS spectra showing clear peaks in the visible range also have been reported for BrC observed in several field studies [Doherty et al., 2010; Corr et al., 2012; Liu et al., 2013] suggesting that both molecular and supramolecular complexes of functional chromophores may coexist in atmospheric BrC.

In order to accurately interpret the aerosol optical depth (AOD) which is the light extinction of aerosols in the atmospheric column, it is essential that BrC contribution to light absorption be investigated thoroughly. Climate models calculate the AOD data and implement them in their climate predictions. This requires accurate knowledge of the main single particle optical quantities namely extinction efficiency and single-scattering albedo (SSA). Current global models often only account for BC and mineral dust as the light-absorbing aerosols in the atmosphere, and regard the rest of OA as purely scattering [Bond et al., 2011; Ma et al., 2012]. However, the increasing amount of data in recent studies implying that BrC concentration is quite significant in certain geographic locations, where it may play a crucial role in total aerosol absorption or even dominate it at specific wavelengths near UV [Kirchstetter et al., 2004; Ramanathan et al., 2007; Yang et al., 2009; Bond et al., 2011; Bahadur et al., 2012; Chung et al., 2012; Ma et al., 2012; Feng et al., 2013].

3.3. Wavelength-dependent light absorption of BrC

Unlike BC, the light-absorption coefficient of BrC is strongly dependent on the wavelength of solar radiation ($\lambda^{-2} - \lambda^{-6}$) with absorption increasing smoothly from the visible to the UV range [Andreae and Gelencser, 2006; Moosmueller et al., 2011; Lack and Langridge, 2013; Laskin et al., 2015; Bluvshstein et al., 2016].

BrC was first introduced in the experimental studies [Bond, 2001; Kirchstetter et al., 2004; Andreae and Gelencser, 2006; Bond and Bergstrom, 2006] where they identified a new class of carbonaceous aerosols based on the spectral dependence of their light-absorption using the following power law relationship:

$$\text{MAC}_a(\lambda) = K\lambda^{-\text{AAE}}$$

Where, MAC_a is the mass absorption cross-section (in $\text{cm}^2 \text{g}^{-1}$), K is a factor that includes aerosol mass concentration, λ is the wavelength (nm), and AAE is the absorption Angström exponent.

The corresponding AAE values for absorptions dominated by BC aerosols are close to 1 [Bergstrom et al., 2002; Bond and Bergstrom, 2006; Drozd and McNeil, 2014; Valenzuela et al., 2015]. The AAE values rise sharply toward shorter wavelengths and are linked to organic aerosols generated from inefficient combustion at lower temperatures during biomass burning. Kirchstetter et al. (2004) separated the organic component from the soot like carbon material in a biomass sample using solvent extraction and measured the AAE for each case. The original sample showed a strong wavelength dependence with $\text{AAE} = 2.2$, but drops to $\text{AAE} = 1.3$ after the removal of the organic constituents. In a modeling study, Lack and Cappa observed that AAE values for internally mixed OC/BC particles could range from 1 – 1.6 and suggested particles with AAE values higher than 1.6 should be categorized as BrC [Lack and Cappa, 2010].

Recent climate modeling studies [Chung and Ramanathan, 2012; Feng et al., 2013; Wang et al., 2014], demonstrated the importance of BrC wavelength-dependent absorption using satellite-based remote sensing retrievals [Jethva and Torres, 2011] and AOD data analysis from Aerosol Robotic Network (AERONET) spectral

measurements [Arola et al., 2011; Bahadur et al., 2012; Wang et al., 2013; Wang et al., 2014]. The extent of BrC contribution to positive radiative forcing of climate is estimated to be in the range of 0.1– 0.25 W m⁻², which is approximately 25% of the radiative forcing by BC (1.07 W m⁻²) [Feng et al., 2013]. The regional impacts of BrC over major biomass burning areas and biofuel combustion sites, such as South America, South and East Asia and subtropical regions in Africa may be substantially higher than 0.25 W m⁻², implying that BrC might dominate absorption in these regions [Feng et al., 2013].

The importance of BrC light absorption in the UV region of the solar spectrum may also significantly decrease the photolysis rates of photochemically active gaseous compounds and alter the concentrations of oxidation agents in the atmosphere including ozone [Li et al., 2011; Jiang et al., 2012].

There are large gaps in understanding the fundamental data regarding BrC sources, formation mechanisms, chemical composition, and optical properties. Further instrumental optimization, extensive laboratory and field studies are required to have a more advanced understanding to characterize the chemical composition and absorption properties of BrC.

3.4. The impact of morphology on the optical properties of BrC aerosols

The change in morphology and physical state of BrC particles could potentially impact their radiative properties [Laskin et al., 2015]. It is important to understand how RH fluctuations in the atmosphere might affect particle morphology, and the distribution of light absorbing OC within the particle, and alter chemical equilibrium between BrC chromophores and non-absorbing OA constituents.

The lack of accurate knowledge regarding the chemical composition and internal structure of BrC particles with respect to the location of chromophores within individual particles makes the investigation of optical properties of BrC aerosols even more challenging.

The impact of liquid-liquid phase separation (LLPS) in particles containing BrC has not yet been investigated and the extent at which LLPS could impact the optical

properties of aerosols is quite unknown. The diversity of light absorbing OC requires more lab and field studies to classify BrC in terms of their absorbing ability. It is important to note that upon LLPS, the chromophores stay in the organic phase.

The modeling studies could also help to shed some light on the impact of different morphologies on the optical properties of particles containing BrC.

In chapter 6, we used a concentric and eccentric core-shell model to predict the potential impact of LLPS on the optical properties of a ternary model system containing ammonium sulfate/ BrC/ H₂O.

Chapter 4

4. Experimental

Optical microscopy was used to investigate the change in morphology of the particles in a selected model system consisting of carminic acid (CA), Ammonium sulfate (AS), and water during the humidity cycle. The morphological changes for a selected droplet were recorded at different temperatures including 20°C, 15°C, 10°C, and 5°C. The experiment at each temperature was performed at three different rates ranging from RH%.min⁻¹ to RH%.min⁻¹. The impact of kinetic limitations in forming different configurations in the droplets was investigated using the procedures and instrument explained in the following sections.

4.1. Materials

For this work, we designed a simple model system consist of pure ammonium sulfate ((NH₄)₂(SO₂)) salt representing the major inorganic component in the troposphere and carminic acid (C₂₂H₂₀O₁₃) as an organic compound. Carminic acid (CA) is a red dye that naturally occurs in some scale insects and absorbs light in the blue region of the solar spectrum. As illustrated in Fig. 4.1, the core structure of CA is an anthraquinone linked to a glucose sugar unit. Anthraquinone is a building block of many dyes and is poorly soluble in water. It has been used as a proxy for the organic fraction of mixed aerosol particles resembling humic-like substances absorbing solar radiation in the atmosphere. All components were purchased from Sigma-Aldrich with purities ≥ 98% and were used without further purification.

Aqueous solutions containing ammonium sulfate (AS) and carminic acid (CA) in 1:3 organic-to-inorganic ratio (OIR) were prepared by adding purified water (resistivity $\geq 18.0 \text{ M}\Omega \text{ cm}$) to the mixture of dry AS and CA.

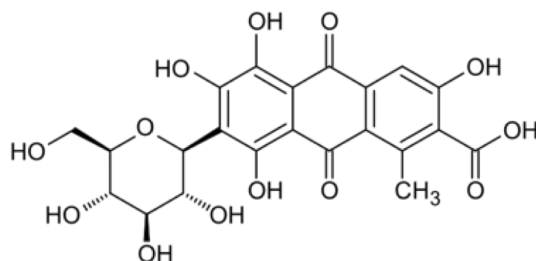


Figure 4.1: Molecular structure of carminic acid, which may be viewed as a proxy for humic-like substances in the organic fraction of aerosol particles.

4.2. Sample preparation

Micrometer-sized droplets are produced from mixed organic/inorganic aqueous solutions using a homemade droplet generator, which consists of a modified ink-jet cartridge (Hewlett Packard, Model HP 51604) (Knopf, 2003) and deposited on commercially siliconized glass circle cover slides with 12 mm in diameter (HR3-277, HAMPTON Research, CA, USA) to prevent the spreading of the aqueous solutions and heterogeneous nucleation due to surface contact. A few 10 μl of aqueous solution are filled into the cartridge. A resistor wire heats the solution for a short period of time. This causes the formation of a gas bubble in the solution, which pushes out a tiny amount of the liquid through the nozzle shown in figure 4.2. Single pulse mode was used to generate about 30 single droplets amongst which one droplet is chosen for further investigation under the microscope. Schematic representation and the working principle of the droplet generator are illustrated in Figure 4.2.

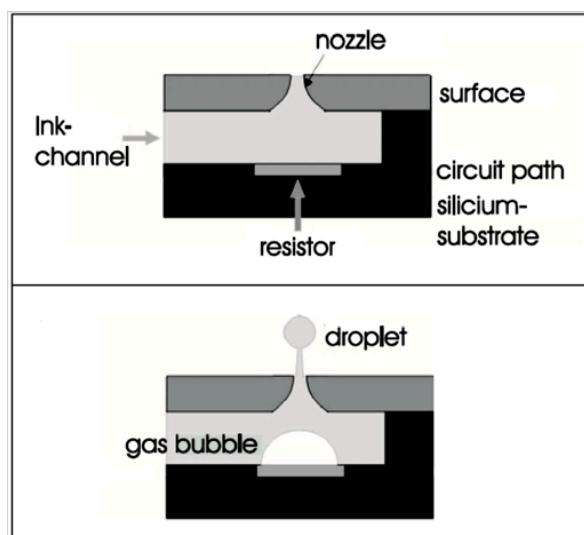


Figure 4.2: Schematic diagram of the droplet generator adapted from Knopf (2003). Upper panel shows the internal structure of the modified inkjet cartridge. Lower panel depicts the process of droplet formation.

4.3. Optical microscopy

Figure 4.3 illustrates the setup that was used to investigate the morphological behavior of the mixed AS/CA droplets. The hydrophobically coated microscopic slide is mounted in an environmental flow cell (about 10 cm³ in volume) and illuminated from below. The temperature within the cell is kept constant by water heating/cooling of the cell housing and the support of the microscopic slide. To adjust RH inside the cell, the water vapor mixing ratio of a constant total flow (typically 200 sccm) is varied by mixing dry and water saturated N₂ flows using automatic mass flow controllers. Temperature and RH of the gas flow inside the cell are measured by a sensor (G-TUCN.34, U.P.S.I. Humidity Sensing, France; capacity probe for measuring RH, NTC resistor for measuring temperature), which is positioned about 15 mm downstream from the gas entrance. An additional Pt100 temperature sensor (Minco, USA) is attached to the substrate to measure the temperature of the slide inside the cell.

Online readouts for temperature and RH in the cell, adjustment of the N₂/H₂O gas flows through the mass flow controllers to run humidity cycles are controlled by a PC

using a customized program (VEE, Agilent, USA).

The instrument uses an optical microscope (Olympus BX-40) with long working distance objective (magnification 50, aperture 0.7, Leica, Germany) and black-and-white CCIR camera (acquisition frequency of 25 frames per second, 8 bit gray levels) to take movies of the selected droplet while exposed to humidity cycles (see Fig. 2). This objective/camera combination leads to a field of view of 720×726 pixels with a nominal resolution of $0.204 \mu\text{m}$ per pixel.

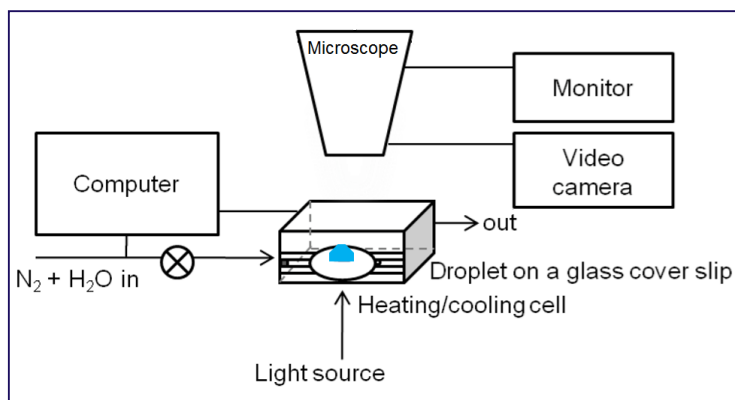


Figure 4.3: Schematic diagram of the experimental setup. The blue half sphere is representing a single droplet deposited on a hydrophobically coated glass slide.

4.4. Calibration methods of RH and temperature sensors

The specified accuracy of the G-TUCN.34 RH sensor by the manufacture company is $\pm 2 \%$ in the RH range from 2 – 98 %. However, since precise knowledge of RH and temperature is critical to our experiments, we calibrated the commercial RH sensor (G-TUCN.34) using the deliquescence RH for a number of inorganic salts to prevent offsets from the calibration curve provided by the manufacturer. The deliquescence RH is always measured upon humidification. Since capacitive RH probes are known to show hysteresis (Li et al., 2000) between humidifying and drying, we conservatively estimate the accuracy of the RH measurements to be no worse than $\pm 3\%$. The calibration curve for a G-TUCN.34 RH sensor is shown in figure 4.4 below.

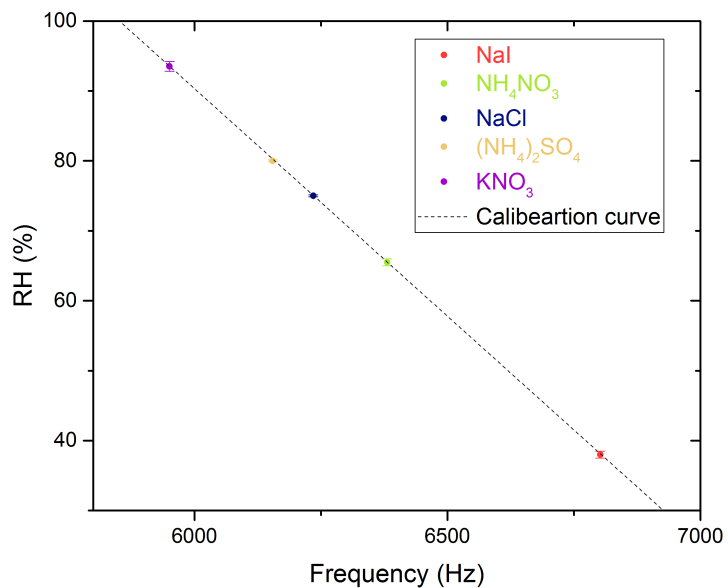


Figure 4.4: Calibration curve for a G-TUCN. 34 RH sensor. DRH onset of the pure inorganic salts KNO_3 (purple circle), $(\text{NH}_4)_2\text{SO}_4$ (yellow circle), NaCl (blue circle), NH_4NO_3 (green circle), and NaI (red circle). Error bars: standard deviation of experiments with different particles.

Chapter 5

Kinetic Limitation to Inorganic Ion Diffusivity and to Coalescence of Inorganic Inclusions in Viscous Liquid-liquid Phase Separated Particles

Published as: Fard, M. M.; Krieger, U. K.; Peter, T. Kinetic Limitations to Inorganic Ion Diffusivity and to Coalescence of Inorganic Inclusions in Viscous Liquid-Liquid Phase Separated Particles. *J. Phys. Chem. A*. **2017**, 121 (48), 9284-9296.

ABSTRACT Mixed organic/inorganic aerosols may undergo liquid-liquid phase separation (LLPS) when relative humidity drops in the atmosphere. Phase separated particles adopt different morphologies, which will have different consequences for atmospheric chemistry and climate. Recent laboratory studies on submicron particles led to speculation whether LLPS observed for larger drops might actually be suppressed in smaller droplets. Here, we report on micron-sized droplets of a ternary mixture of ammonium sulfate (AS), carminic acid and water at different temperatures, which were exposed to typical atmospheric drying rates ranging from 0.34–5.0% RH min⁻¹. Our results reveal that increasing drying rate and lowering temperature results in different morphologies after LLPS and may suppress the growth and coalescence of the inorganic-rich phase inclusions due to kinetic limitations in a viscous matrix. The coalescence time was used to estimate the viscosity of the organic-rich phase within a factor of 20 and based on the Stokes-Einstein relationship, we estimated AS diffusivity. Furthermore, we evaluated the initial growth of inclusions to quantitatively determine the AS diffusivity in the organic-rich phase, which is about

$10^8 \text{ cm}^2 \text{ s}^{-1}$ at room temperature. Extrapolation of diffusivity to lower temperatures using estimations for the diffusion activation energy leads us to conclude that the growth of the inorganic phase is not kinetically impeded for tropospheric submicron particles larger than 100 nm.

5.1. Introduction

Aerosol particles are an integral part of the atmosphere and play an important role in influencing the Earth's radiation budget, hydrological cycle in the atmosphere, climate change, human health and regional visibility with many possible feedback mechanisms that are far from being fully understood [Finlayson-Pitts and Pitts, 1997; Ravishankara, 1997; Martin et al., 2004; Pope and Dockery, 2006; Seinfeld and Pandis, 2006; Forster et al., 2007]. In order to minimize the uncertainties associated with aerosol forcing, a better understanding is needed of aerosol abundance, chemical composition, physical state, size, and morphology of aerosols [Hanel, 1976; Martin, 2000; IPCC, 2013]. Tropospheric aerosols are composed of inorganic salt, acids, organic compounds and water. These components are mostly internally mixed [Lee et al., 2002; Marcolli et al., 2004; Murphy et al., 2006]. The physical state of aerosol particles depends on their chemical composition, ambient relative humidity (RH) and temperature [Kwamena et al., 2010; Reid et al., 2011; Krieger et al., 2012]. When aerosol particles are exposed to humidity cycles in the atmosphere, they may undergo phase transitions such as deliquescence and efflorescence [e.g., Martin, 2000; Clegg et al., 2001; Brooks et al., 2002; Pankow, 2003; Parsons et al., 2004; Erdakos et al., 2006; Marcolli and Krieger, 2006; Anttila et al., 2007; Ciobanu et al., 2009; Prisle et al., 2010; Zuend et al., 2010; Smith et al., 2011].

Experiments and modeling studies on model systems for mixed organic/inorganic aerosols have shown that deliquesced aerosols can exist not only as one-phase systems containing organics and inorganics together, but often as two-phase systems consisting of a predominantly organic and a predominantly inorganic aqueous phase [Pankow, 2003; Marcolli and Krieger, 2006; Ciobanu et al., 2009a,b; Bertram et al.,

2011; Krieger et al., 2012]. Recent laboratory studies were conducted with model mixtures representing tropospheric aerosols [Ciobanu et al., 2009; Ciobanu et al., 2010; Bertram et al., 2011; Song et al., 2012a; Song et al., 2012b], secondary organic aerosol from smog chamber experiments [Smith et al., 2012] and from field samples [You et al., 2012]. All these studies suggest that liquid-liquid phase separation (LLPS) is indeed a common phenomenon in mixed organic/inorganic particles. Below a critical relative humidity, when phase separation occurs (often termed SRH), the two phases in the particle may adopt different morphologies, such as core-shell, partially engulfed, or the formation of multiple inorganic inclusions in the organic phase. A core-shell configuration isolates the inner phase from the surrounding gas phase, which may affect heterogeneous chemistry, gas to particle partitioning of semi-volatile organic aerosols, hygroscopicity, and optical properties of aerosols [Anttila et al., 2007; Cosman et al., 2008; Zuend et al., 2010; Zuend and Seinfeld, 2012].

In recent years, studies including the ones done by our group, investigated the morphology of different inorganic/organic mixed systems at or near room temperature. Examinations of changes in morphology of the particles at lower temperature that are more representative of tropospheric conditions are still missing.

Veghte et al. and Altaf et al. Investigated the size dependence of morphology of mixed particles by means of cryo-transmission electron microscopy requiring an ultrafast drying rate ($99.7\% \text{ RH s}^{-1}$ and $87.2\% \text{ RH s}^{-1}$, respectively), leading to extremely dry conditions ($\text{RH} < 2\%$). These drying rates are three to four orders of magnitude faster than drying rates occurring in the real atmosphere. They observed that LLPS does not tend to happen for some model organic systems in accumulation-mode (submicron, 20 nm – 900 nm) particles below a critical size in the range of 82 nm – 270 nm and made the small size of the particles responsible for this observation. If true, this would contradict Bertram et al. and Song et al., who concluded for a wide range of organic substances and mixtures that LLPS always occurred for oxygen-to-carbon ratios $\text{O:C} < 0.56$, never for $\text{O:C} > 0.80$, and depending on the specific types and compositions of organic functional groups in the regime $0.56 < \text{O:C} < 0.80$.

However, Bertram et al. and Song et al. relied on using super-micron droplets, as we do in the present work, i.e. radii factors 10^2 and volumes 10^6 times larger than those used by Veghte and colleagues in a later publication [Altaf et al., 2016], they made a comment that the fast drying rate ($87.2\% \text{ RH s}^{-1}$) of their experiment might have influenced the outcome of LLPS where nucleation and growth is the predominant mechanism of phase separation. However, our experiments below reveal a pronounced sensitivity of morphology with respect to the drying rate. Given our experiments and the absence of a physical mechanism distinguishing LLPS in super-micron droplets from submicron droplets larger than 100 nm (which are still too large for the Kelvin effect to be significant), we argue here that also the particles investigated by Veghte et al. and Altaf et al. may undergo LLPS despite their small size, but that the growth of the second phase was likely suppressed due to kinetic limitations under the extremely high drying rates of their experiments, which quenched the particles.

To investigate the impacts that kinetics might have on the formation of LLPS and different morphology under different drying rates and temperatures, we studied the change in morphology of the ammonium sulfate / carminic acid / H₂O model system (AS/CA/H₂O) for droplets between 40 – 75 μm in diameters using optical microscopy. AS and CA were mixed at organic-to-inorganic mass ratio (OIR) = 1:3. CA is poorly soluble in water. It has been used as a proxy for organic fraction of mixed aerosol particles resembling humic-like substances. The distinctive morphological features of each experiment, which was conducted at a specific temperature and drying rate, will be discussed in the following sections.

In addition to morphology analysis, frame-by-frame image analysis was used to evaluate the growth of inclusions after onset of LLPS. Available thermodynamic data were combined with the information obtained from particle analysis, to quantitatively estimate the diffusion constant of AS in the organic-rich matrix surrounding the inclusions.

We also used image analysis to analyze the kinetics of coagulation of separate phase inclusions for estimating the viscosity of the organic-rich phase after phase separation occurred and compared viscosity with AS diffusivity utilizing the Stokes-Einstein relationship. Finally, using the thermodynamic data of our model system and assuming specific diffusion activation energies, we estimated the time required for a submicron particle (≥ 100 nm) undergoing LLPS to establish a fully developed inorganic inclusion.

5.2. Experimental Scheme

5.2.1. Material and sample preparation

As illustrated in Figure 5.1, the core structure of CA is an anthraquinone linked to a glucose sugar unit. Anthraquinone is a building block of many dyes and is poorly soluble in water. CA is a red dye that naturally occurs in some scale insects to protect them against predators. Its multi-functional ring structure, low solubility in water and absorptive properties may make it a good candidate for humic-like substances. Aqueous solutions of CA and AS at OIR = 1:3 were prepared by dissolving the pure substances in purified water (resistivity ≥ 18.0 M Ω cm). All components were purchased from Sigma-Aldrich with purities $\geq 98\%$ and were used without further purification.

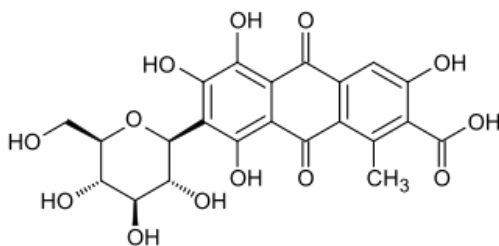


Figure 5.1. Molecular structure of carminic acid, which may be viewed as a proxy for humic-like substances in the organic fraction of aerosol particles.

Micrometer-sized droplets are produced from mixed organic/inorganic aqueous solutions using a homemade droplet generator [Knopf, 2003], which consists of a modified ink-jet cartridge (Hewlett Packard, Model HP 51604), and deposited on commercially siliconized glass circle cover slides with 12 mm in diameter (HR3-277, HAMPTON Research, CA, USA). A few 10 μL of aqueous solution are filled into the cartridge to generate 30 single droplets amongst which one droplet is chosen for further investigation under the microscope.

5.2.2. Flow cell microscopy

Figure 5.2, illustrates the setup that was used to investigate the morphological behavior of the mixed AS/CA droplets. The hydrophobically coated microscopic slide is mounted in an environmental flow cell (about 10 cm^3 in volume) and illuminated from below. The temperature within the cell is kept constant by water heating/cooling of the cell housing and the support of the microscopic slide. To adjust RH inside the cell, the water vapor mixing ratio of a constant total flow of typically 200 sccm is varied by mixing dry and water saturated N_2 flows using automatic mass flow controllers. Temperature and RH of the gas flow inside the cell are measured by a sensor (G-TUCN.34, U.P.S.I. Humidity Sensing, France; capacity probe for measuring RH, NTC resistor for measuring temperature), which is positioned about 15 mm downstream from the gas entrance and illustrated as a black object upstream of the droplet. An additional Pt100 temperature sensor (Minco, USA) is attached to the substrate to measure the temperature of the slide inside the cell.

Online readouts for temperature and RH in the cell and the adjustment of the $\text{N}_2/\text{H}_2\text{O}$ gas flows by the mass flow controllers to run humidity cycles are controlled by a PC using a customized program (VEE, Agilent, USA). As precise knowledge of RH and temperature is critical to our experiments, we calibrated the commercial RH sensor (G-TUCN.34) using the deliquescence RH for a number of inorganic salts to prevent offsets from the calibration curve provided by the manufacturer. The deliquescence RH is measured upon humidification. Since capacitive RH probes are known to show

hysteresis [Li et al., 2000] between humidifying and drying, we conservatively estimate the accuracy of the RH measurements to be no worse than $\pm 3\%$.

We determine separation relative humidity, SRH, in our experiments upon drying. Uncertainties associated with SRH are large and related to a number of factors: (a) hysteresis of the capacitor sensor, (b) inhomogeneities in the water vapor concentration field within the cell, (c) a diffusive gradient of water vapor across the boundary layer flow (which may be laminar or turbulent), (d) the stochastic character of phase separation, which is a nucleation process in our system, hence varying from experiment to experiment despite unchanged conditions.

The instrument uses an optical microscope (Olympus BX-40) with long working distance objective (magnification 50, aperture 0.7, Leica, Germany) and black-and-white CCIR camera (acquisition frequency of 25 frames per second, 8 bit gray levels) to take movies of the selected droplet while exposed to humidity cycles (see Figure 5.2).

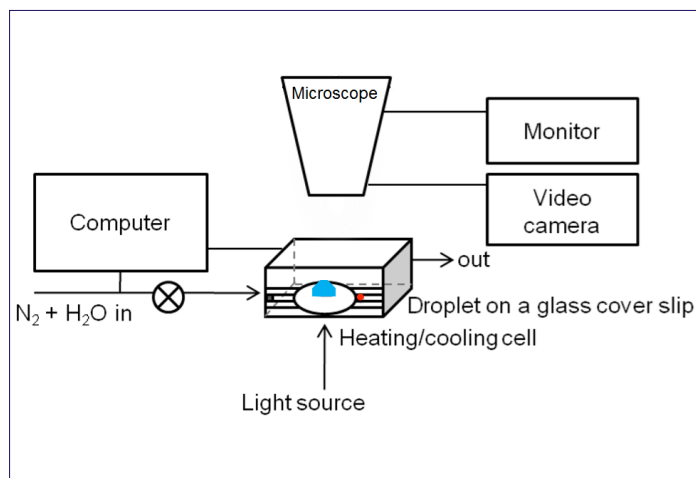


Figure 5.2. The schematic diagram of the experimental setup. The blue half sphere is representing a single droplet deposited on a hydrophobically coated glass slide. The red object is the Pt 100 temperature sensor attached to the substrate.

5.2.4. Image Analysis

The photographic objective/camera combination leads to a field of view of 720×726 pixels with a nominal resolution of $0.204 \mu\text{m}$ per pixel. To measure total droplet size and the size of inclusions of the inorganic phase after LLPS for each frame of the recorded video we use the public domain image-processing program “ImageJ 1.x”⁴⁰. We used the Bernsen method [Bernsen, 1986] with a local threshold to convert the movie into binary black and white images frame by frame. Each inclusion was enclosed with the elliptical selection tool of “ImageJ” and its area and center of mass was calculated in pixel and then converted to effective radius in μm . This only allows measuring the two-dimensional projection of the investigated objects, whereas the third dimension in the direction of light remains undetermined, an issue discussed below.

5.3. Results and Discussions

The first part of this section is qualitative, i.e. we first discuss the general morphology of aqueous AS/CA particles during phase separation at an intermediate temperature of 15°C (Section 5.3.1), and then investigate the impact of the drying rate (Section 5.3.2) and of temperature (Section 5.3.3) on the particle morphology. Subsequently we address the question, whether the observations made here for supermicron particles could also apply to submicron particles (see atmospheric implications). The second half of the section is semi-quantitative by first showing that the inclusions resemble more a two- than a three-dimensional geometry (Section 5.3.4). From this we estimate the viscosity of the AS/CA/H₂O ternary system (Section 5.3.5) and finally we quantify the diffusivity of ammonium sulfate ions in the organic-rich particle shell (Section 5.3.6).

Table 5.1, summarizes the 19 experiments performed in the present work: nine around 20°C , five around 15°C , three at 11°C , and two around 6°C . Separation

relative humidity, SRH, is associated with substantial uncertainties and therefore is only indicative, for reasons mentioned in Section 5.2.2. In the subsequent sections we will systematically refer to the experiment numbers given in Table 5.1. Those experiments in the table marked by a star (*) are discussed in detail with respect to dependences on drying rate and temperature in Sections 5.3.1-5.3.3.

Table 5.1. The 19 experiments performed in the present work, sorted first according to temperature, subsequently according to drying rate.

Exp. #	Temp (°C)	Drying (RH% min ⁻¹)	SRH (%)	Morphology observed before efflorescence
1*	20.7	-0.34	74	Spherical core-shell
2	20.7	-0.44	65	Non-spherical core-shell
3	20.8	-0.51	68	Non-spherical core shell
4	20.7	-0.81	71	Spherical core-shell
5	20.7	-0.82	71	Spherical core-shell
6	20.6	-0.85	72	Spherical core-shell
7	20.7	-1.41	72	Non-spherical core shell
8	20.0	-3.00	78	Multiple inclusions, no final coalescence, “freezing in”
9	19.6	-3.22	56	Multiple inclusions, no final coalescence, “freezing in”
10	15.8	-0.29	74	Spherical core-shell
11	15.8	-0.41	69	Semi-spherical core-shell
12*	15.8	-0.55	66	Non-spherical core-shell
13*	15.8	-0.76	69	Five final inclusions that grow but do not coalesce
14	15.8	-2.93	68	Some inclusions after coalescence and growth
15	10.0	-0.42	67	Four inclusions that grow but do not coalesce
16	11.0	-1.58	67	Some inclusions after coalescence and growth
17	11.0	-4.91	33	Multiple inclusions, minor growth, “freezing in”
18*	6.2	-0.54	62	Multiple inclusions, “freezing in”
19	6.1	-2.38	27	Multiple inclusions, “freezing in” in half of the particle

Experiments marked by stars (*) indicate the experiments that are discussed in detail in Sections 5.3.1-5.3.3. SRH is very uncertain and hence only indicative.

5.3.1. Morphology of aqueous AS/CA particles during phase separation

The general morphology pattern evolving upon LLPS is illustrated for Experiment #12 in Figure 5.3. This particular experiment was conducted at 15.8°C, starting from a humidity of 85%. We apply a drying rate of 0.55% RH per minute. The red arrow in Frame 5.3b marks the start of LLPS at RH = 65.8%. The second phase appears first as a single AS inclusion in the middle of the droplet, followed by three separate inclusions closer to the edge of the particle (Frames 5.3a-c), indicating nucleation and growth as the mechanism behind LLPS. All inclusions grow in size until two of them coalesce and form a single, larger inclusion (Frames 5.3g-h). During initial growth (Frames 5.3e-f), one can observe that the inclusions at the edges appear to move towards the center. Note, that during the entire drying the outer diameter of the droplet does not shrink in spite of the water loss to the gas phase (presumably because of surface tension effects). Hence, as RH decreases and water evaporates from the particle surface, the whole particle needs to flatten. It is likely that this flattening pushes the inorganic phase inclusions towards the center.

When two inclusions grow and get in close proximity (Frames 5.3f-g), they touch and coalesce into a bigger non-spherical inclusion (Frame 5.3g) and then rearrange to a more spherical shape (Frame 5.3h). McGuire et al., (1996) proposed a model to describe the merging of two inclusion droplets and the impact the two coalescing inclusions will have on nearby inclusions. In Section 5.3.5 we will use this model to quantitatively estimate the viscosity of the CA/H₂O phase. When two inclusions coalesce, fluid is displaced and this flow causes the movement of neighboring inclusions, which may result in the subsequent coalescence events. Their model assumptions correspond quite well with what we observe to take place from Frames 5.3f-j. The motion of two smaller inclusions, represented by two small red arrows in Frame 5.3g, towards the larger inclusion just after it coalesced is clearly visible in the movie (see online supporting information). The process continues until all 4 initial inclusions have coalesced and form a single, non-spherical inorganic inclusion

equivalent to a core-shell morphology of the phase-separated droplet. The particle maintains this shape for another half hour and RH drops from 51.3% to 34.7%, when finally the AS undergoes efflorescence. Obviously, the viscosity of the system at these RHs and $T = 15.8$ °C does not allow the inorganic phase to establish a spherical shape. Frame 5.3l demonstrates the start of efflorescence at 34.7% RH, indicated by the appearance of granular structures in the aqueous AS inclusion. Frame 5.3m shows the particle at 33.8% RH, after the AS efflorescence came to a close. Interestingly, also the remaining AS in the outer organic-rich phase effloresces at this point, leading to a granular structure also of the particle shell. (The granular structure deliquesces at the same time as the AS in the inclusions upon humidification, which indicates that it is made of crystalline AS).

While Figure 5.3 shows the general evolution of particle morphology during LLPS for this system, the drying rate and temperature may influence the evolution as well as the final morphology before efflorescence. This is discussed in the following sections.

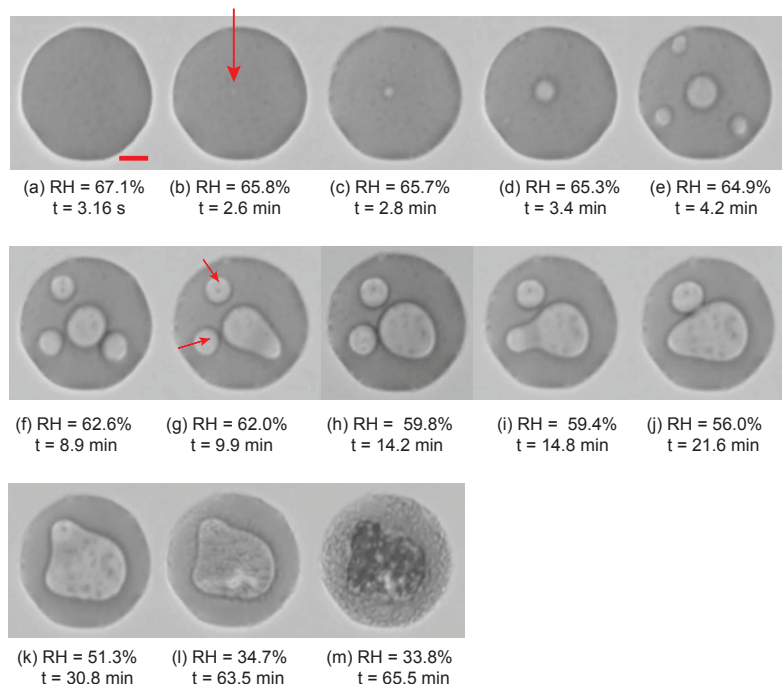


Figure 5.3. The morphology of AS/CA mixture in Experiment #12 at 15.8°C and 0.55% RH drying per minute starting at 67.1% RH at time 0. The onset of LLPS (nucleation of the first inorganic phase inclusion) is marked by a red arrow in (b). The size bar in (a) is 10 μm .

5.3.2 The impact of drying rate on morphology

Figure 5.4, illustrates the changes observed in morphology for Experiment #13, which is very similar to the one shown in Figure 5.3, namely the same temperature (15.8°C), but at a faster drying rate. An initially homogenous AS/CA particle is dried from 70% to 34% RH with a rate of 0.76% RH per minute, i.e. about a factor of 1.4 faster compared to Experiment #12 shown in Figure 5.3. Frame 5.4b shows that SRH is about the same for both cases, within the uncertainty of the humidity sensor, but the number of AS inclusions forming the inorganic phase is higher when the drying rate is faster. This is consistent with a nucleation and growth mechanism of LLPS. The

higher drying rate leads to a slower reduction in supersaturation during the growth of the first inclusions. This allows additional nucleation events to occur during the initial phase of LLPS. There are some coalescence incidents during the experiment, see Frame 5.4f-g, leading to the formation of three larger and two smaller inclusions (Frame 5.4h) before efflorescence takes place (Frames 5.4i-1). Efflorescence happens independently in the different inorganic inclusions, see Frame 5.4i with just one effloresced inclusion and Frame 5.4j with all of them.

Unlike the previous experiment, the five inclusions remaining after the initial limited coalescence activity do not coalesce further but remain separated. In particular, they do not form a concentric spherical core-shell morphology, nor do they adapt spherical shapes. We conclude that with faster drying, the viscosity of organic phase increases rapidly enough to reduce the mobility of the inclusions and, hence, their coalescence rate significantly. This implies that condensed phase water diffusion is fast enough to lower the water content of the organic phase and hence increase viscosity drastically.

In summary, the reason behind this observation is the stronger forcing of the particle, which does not provide enough time for the AS to diffuse to the initially nucleated inclusions (Frame 5.4b), triggering the nucleation of more inclusions (Frame 5.4c) until the diffusive uptake of AS by a sufficient number of inclusions (Frame 5.4d in this case) can compete with the further forced increase in AS supersaturation (Frame 5.4f). The further drying then allows some limited coalescence (Frame 5.4g), but the aspherical shapes of the resulting inclusions already suggest increased viscosity and decreased mobility, so that further nucleation is suppressed (Frames 5.4h-i), long before AS efflorescence sets in (Frames 5.4j-1).

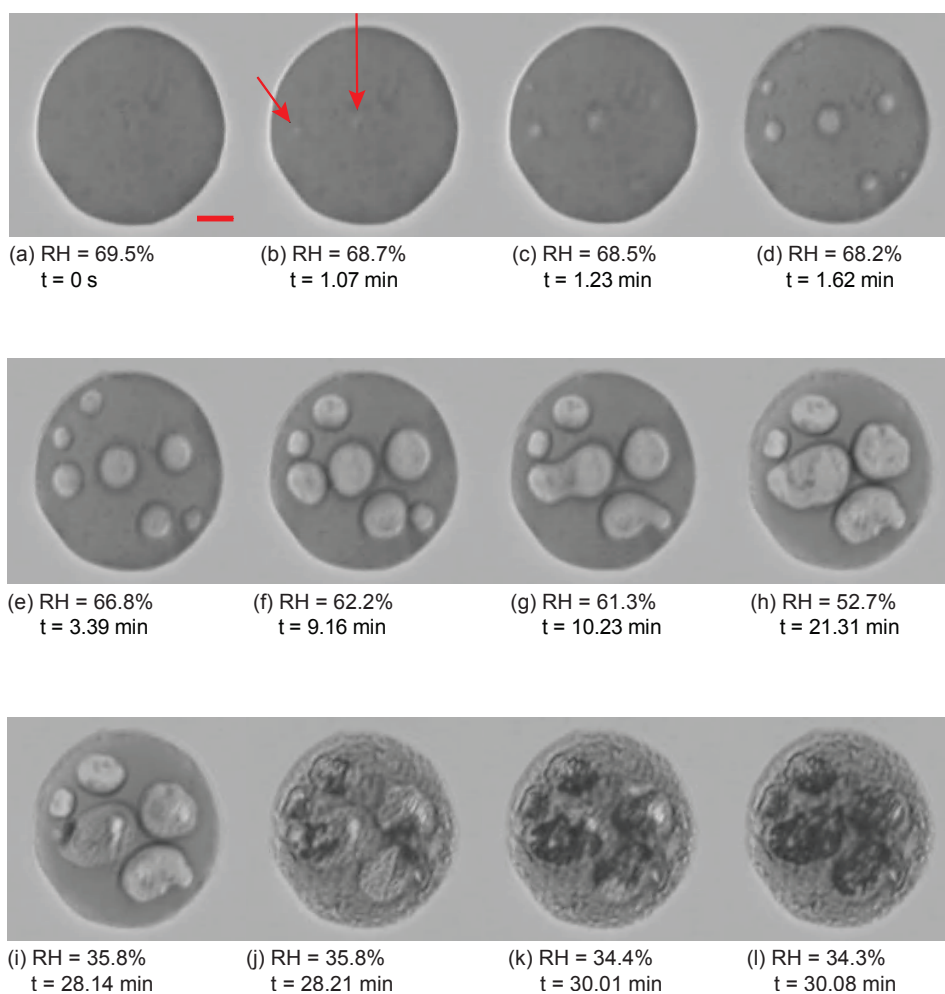


Figure 5.4. The morphology of AS/CA mixture in Experiment #13 at 15.8°C and 0.76% RH drying per minute. The onset of LLPS is marked by red arrows in (b). The size bar in (a) is 10 μm .

5.3.3. The impact of temperature on morphology

Another factor impacting the morphology of the aqueous AS/CA particles is temperature. Previous studies on LLPS have been mostly performed at room temperature. You and Bertram⁴³ studied the formation of LLPS at low temperatures (down to -30°C). However, they investigated only the impact of temperature on the onset of LLPS (terming the separation relative humidity “SRH”) and did not discuss

the particle morphology after the formation of the second phase. Morphological data continue to be missing at temperatures lower than room temperature.

Figure 5.5, tracks the morphological changes of the AS/CA particle in Experiment #1 at 20.7°C instead of 15.8°C and a drying rate of 0.34% RH min⁻¹, which is even slower than the rate for the experiment shown in Figure 5.3. Both, the higher temperature and the slower drying rate allow the system to nucleate at even higher RH, and correspondingly the onset of LLPS occurs already at RH = 73.6%. For this particular experiment, we also measured the transition RH from phase separated to homogenous state upon humidification. We found the SRH to be 75.5% RH.

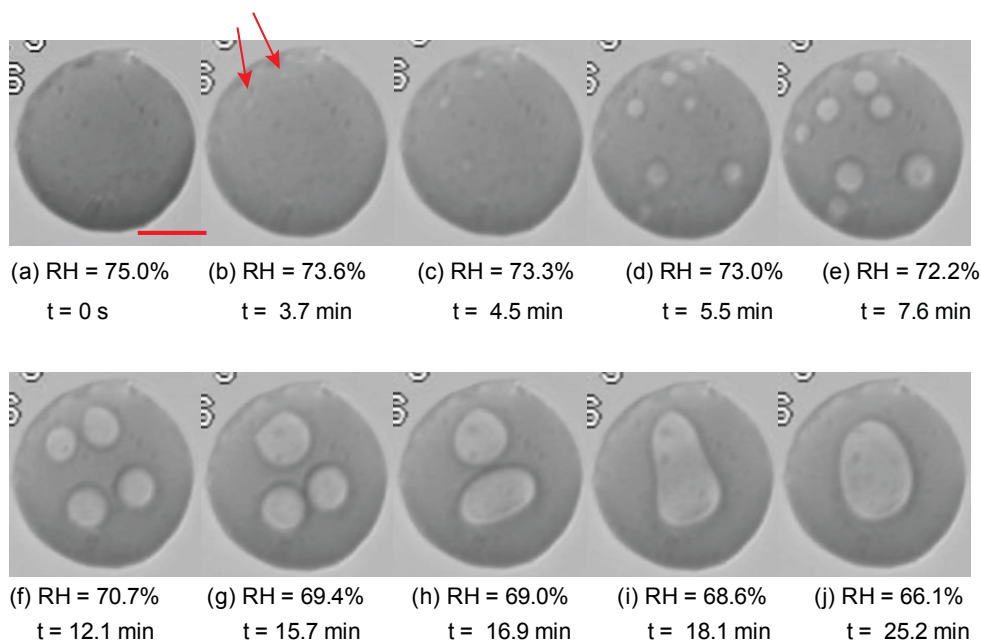


Figure 5.5. The morphology of AS/CA mixture in Experiment #1 at 20.7°C and 0.34% RH drying per minute. The onset of LLPS is marked by red arrows in (a). The bar size in panel (a) is 10 μ m.

After nucleation (Frames 5.5b-d) and formation of highly spherical inclusions (Frame 5.5e), which then coalesce (Frames 5.5f-i), we finally observe the formation of a single, spherical core-shell morphology (Frame 5.5j), before crystallization of AS

takes place (not shown). After final coalescence of the inclusions, the inorganic phase reshapes itself into spherical geometry (see Section 5.3.4, where we discuss this matter quantitatively). Note that the last coalescence to a single, inorganic phase is occurring at 68% RH, significantly higher compared to 55% RH at $\sim 16^\circ\text{C}$. Contrary to the observations shown in Figure 3 at $\sim 16^\circ\text{C}$, here, at the more elevated temperature and higher humidity, the viscosity of the organic phase is low enough to allow the inorganic phase to minimize its surface area. In addition, note that both the significantly smaller size of the particle and slower drying rate in this experiment, reduce the kinetic limitation and promote the formation of the concentric spherical core-shell.

Note that one major difference is that the onset of LLPS occurs at significantly higher RH (SRH = 73.6%) compare to the experiments #12, and #13. For the 20.7°C experiment #1, we measured the SRH on the humidifying ramp to be 75.5%. Hence, the observed difference could be either due to an unexpectedly high temperature dependence of SRH (contrary to findings by You, and Bertram) or the fact that nucleation happens at increasingly higher supersaturation under colder conditions, the latter being the much more likely explanation. Another possibility to explain the difference in the onset of LLPS could be the stochastic nature of nucleation.

Another experiment was performed at 6.2°C and a drying rate of 0.54% RH per minute, shown in Figure 5.6 (#18 in Table 5.1). The drying rate is almost identical to that of the experiment at $\sim 16^\circ\text{C}$ shown in Figure 5.3. This corroborates the strong effect of temperature. The appearance of several inclusions in the second quadrant of the particle marks the onset of LLPS, which spreads from there all over the particle. The directional preference probably points to a ventilation bias in the setup of our cell. Overall, we observe a significantly higher number of nucleation events than in the previous, warmer cases. The most likely explanation is that in the colder, more viscous particle, the diffusivity of the AS ions is much reduced, which in the absence of an inclusion close-by undergo higher supersaturation and are driven to nucleate additional inclusions.

Strikingly, despite a few initial coalescence events, further coalescence is drastically reduced. The morphology, showing a large number of micrometer size inclusions, does not change significantly when RH decreases from 60% to 40%, but “freezes in” during the ~40 minutes of drying (Frames 5.6f-h) before efflorescence starts at RH = 39.9%. These observations are consistent with a significantly larger viscosity of the organic phase at 6°C compared to 15-20°C. In passing we note that the inorganic phase inclusions effloresce individually, see Frame 5.6i.

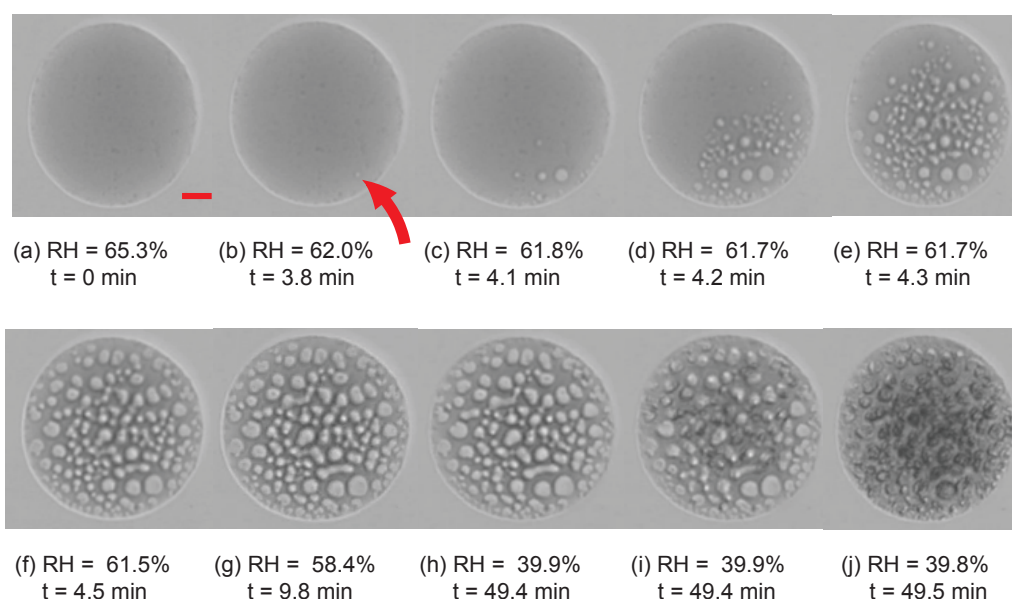


Figure 5.6. The morphology of AS/CA mixture in Experiment #18 at 6°C and 0.54% RH per minute drying rate. The onset of LLPS is marked by a red arrow in (b). The bar size in panel (a) is 10 μm .

Figure 5.7, illustrates the morphology of AS / CA / H₂O particles exposed to low and high drying rates at three temperatures (~20°C, ~16°C, ~6°C) right before efflorescence. This figure emphasizes the importance of drying rate and temperature on the final morphology of mixed particles before crystallization takes place. By

increasing the drying rate at 20°C by about a factor of 10, the particle will develop a morphology similar to the one at 6°C and slow drying.

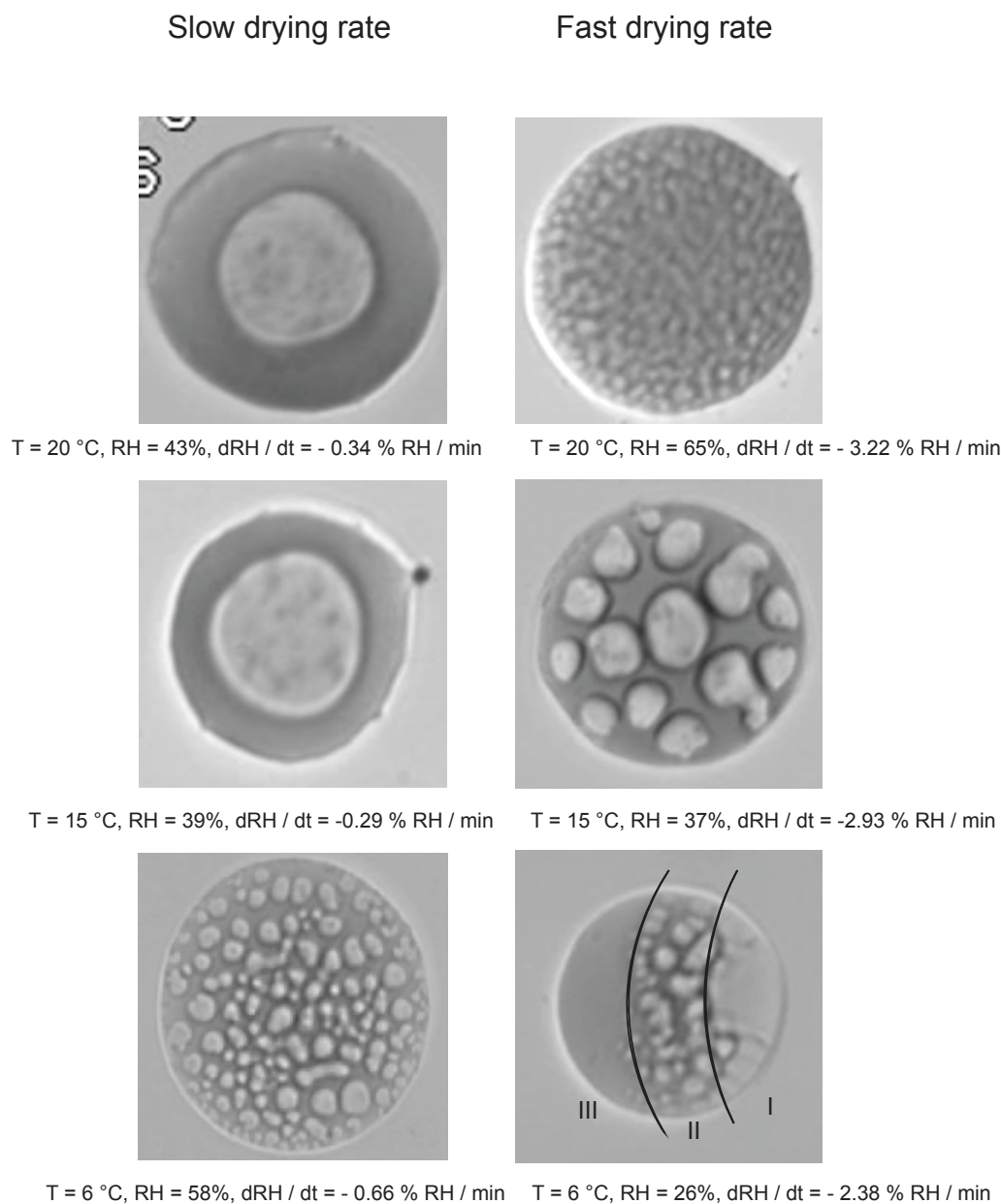


Figure 5.7. The morphologies of particles shortly before efflorescence at ~20°C (experiments #1 and 9), ~16°C (experiments #10 and 14), and ~6°C (experiments #18 and 19), at low and high drying rates (left and right column, respectively). Sectors I-III in Experiment #19 are discussed in the text.

It should be noted that the drying rates at different temperatures are not identical and cannot be compared directly, but it is evident that by increasing the drying rate, the number of final inorganic inclusions increases. The same phenomenon can initially be observed at 6°C, however the morphology of the particle at 6°C and fast drying rate develops differently from the rest (see supporting information for the movie clip). It is likely that under conditions of low temperature and fast drying rate (2.38% RH min⁻¹), the particle builds up massive supersaturation with respect to LLPS, which must lead to nucleation of a very large number of inorganic inclusions. However, these cannot readily grow or coalesce, because of the low diffusivity and high viscosity under these conditions. Similar as for lower drying rates in Experiment #18 (Figure 5.6), also at higher drying rates, the drying proceeds from upstream (sector I) to downstream (sector III), probably because the air stream is moistened by the evaporating water when it flows across the droplet. We can only speculate what happens then. Possibly, on the upstream side in sector I, the many nanoscale inclusions can still grow and coalesce to a visible size, providing a very dense and highly light-scattering matrix. In sector II, there is still some limited coalescence, which becomes visible only at a later time than establishing sector I. In contrast, in the downstream sector III, the substance remains optically homogeneous even below the efflorescence relative humidity. This could either be because AS leaves sector III and diffuses upstream or because AS inclusions form but remain too small to effectively scatter visible light. We can exclude the former explanation, as from Figure 6 there is evidence that AS cannot diffuse rapidly to the upstream side. Therefore, we think that the AS inclusions in sector III exist but remain too small (below micrometer range) to effectively scatter visible light, presumably because the plasticizing H₂O molecules leave the particle rapidly and AS diffusivity becomes very small. However, the exact mechanisms behind establishing sectors I-III remain unclear and should be investigated in future work.

5.3.4. Investigating the geometry of inclusions

In order to characterize the geometry of the inclusions, we calculate the total equivalent sphere volume (Figure 5.8a) and total area (Figure 5.8b) covered by coalescing inorganic inclusions (Experiment #12 at 15.8°C and 0.55% RH min⁻¹, see Figure 5.3). The general shape of these curves, i.e. rapid increase which slowly levels off, represents the growth of the inclusions by diffusive uptake of AS and the subsequent depletion of AS in the organic-rich phase. The discontinuities occur at times of coalescence of two inclusions, namely at ~9.5 minutes (Frames 5.3f-g), ~14.2 minutes (Frames 5.3h-i), and ~22 minutes (Frames 5.3j-k). Coalescence leaves the total volume unchanged, and the microscopic images before and after coalescence of two inclusions provide an indication whether the geometry of the inclusions is half-spheres, spherical caps with constant contact angle, or thin cylindrical discs. Half-spheres or spherical caps with constant contact angle would not show discontinuities in Figure 5.8a, but this is clearly not the case. Rather, the total area is approximately conserved during coalescence, indicating a disc-like shape of the inclusions (at least after they have grown to an equivalent radius of about 5 μm). As discussed above the whole droplet is flattening due to the loss of H₂O molecules during the drying, and hence it is conceivable that initially spherical inclusions are first pushed towards the center of the droplet by geometrical constraints and are forced to assume a disc-like shape when subsequently even less space is available.

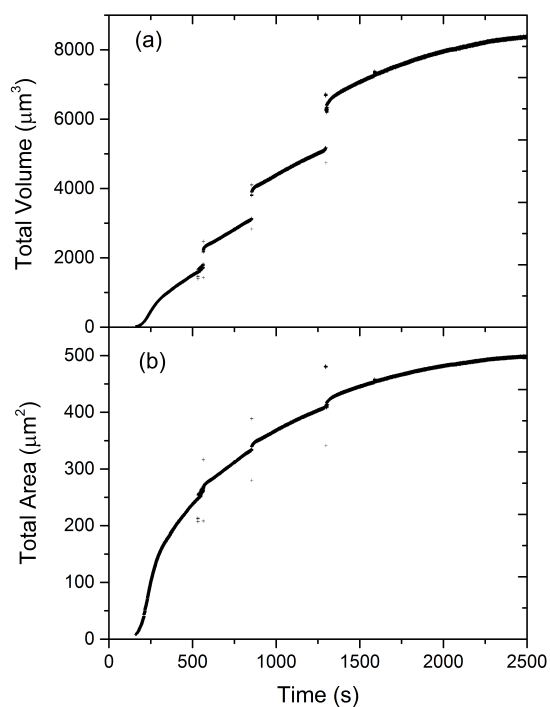


Figure 5.8. (a) Temporal evolution of the total volume of all inorganic inclusions in the AS/CA mixed particle in Experiment #12 at 15.8°C and 0.55% RH min⁻¹ (see Figure 5.3) assuming the volume to be proportional to r^3 (for both spheres and spherical cabs with contact angle remaining unchanged by coalescence). (b) Temporal evolution of the total area in the microscopic image covered by the same inorganic inclusions. Discontinuities occur at times of coalescence of two inclusions.

5.3.5. Estimating the viscosity of the AS/CA/H₂O ternary system

Once several inclusions nucleated, it becomes difficult to quantitatively analyze the growth of the inorganic phase, and we return to this in Section 5.3.6. However, the time needed for coalescence relaxation provides a mean to estimate the viscosity of the organic phase. Pajunoja et al. (2014) used this technique to determine the viscosity of amorphous SOA particles under dry conditions. Based on an approach by Frenkel (1945), they estimated the coalescence relaxation time, t_c , as the ratio of the product of the diameter of the primary dry particles and the viscosity divided by the surface tension. More recently, McGuire et al. (1996) introduced a coalescence model for

liquids having high viscosities and low interfacial tensions. During coalescence two initially spherical symmetric droplets at first touch, a thin film forms between the droplets and afterwards the neck region between the droplets expands until finally a single spherically symmetric droplet evolves (because this shape minimizes the interfacial energy). They showed that the characteristic coalescence relaxation time, t_c , depends on viscosity, η , interfacial tension, γ , the radius of the droplet after coalescence, R , the critical thickness of the film forming initially, h_{cr} , and the initial neck radius, r_0 , as:

$$t_c = \frac{3\eta R^2}{h_{cr}\gamma} \left[1 - \left(\frac{r_0}{R}\right)^2 \left(1 + 2 \ln\left(\frac{R}{r_0}\right)\right) \right] . \quad (5.1)$$

In Figure 5.9, we plot the perimeter of the two inclusions of Experiment #1 with slow drying at 20.7°C shown in Figure 5.5f-g, coalescing at about 690 s. Clearly, the total perimeter of the two inclusions of about 25 μm relaxes upon coalescence to a new perimeter of about 18 μm . Before and after coalescence, the perimeter continues to increase slowly, due to diffusive uptake of AS. We take the 1/e time as the characteristic coalescence time, t_c .

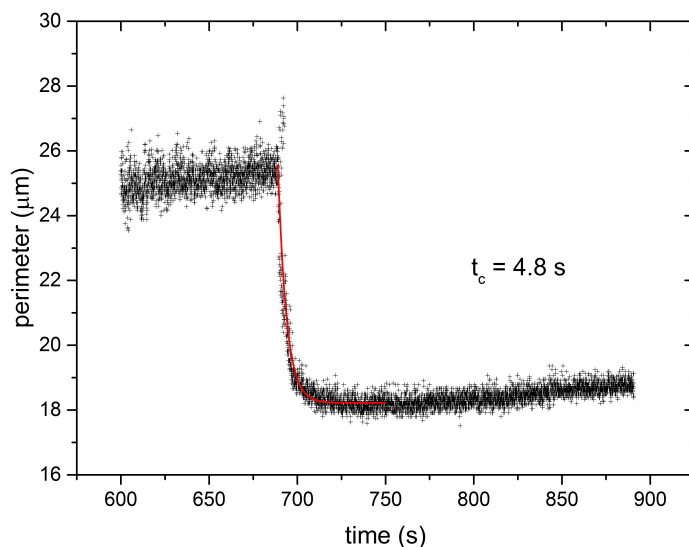


Figure 5.9. Total perimeter of two inclusions coalescing in Experiment #1 at 20.7°C (black crosses) at RH = 70%. Thin red line: exponential decay fitted to the data yielding a characteristic coalescence time of 4.8 s.

The characteristic time for relaxing to spherical shape is $t_c = 4.8$ s for this event (i.e., relaxation of perimeter difference to $1/e$ of its original). To estimate viscosity from these data we follow McGuire et al. (1996) assuming $r_o = 0.1 \times R$ and the critical thickness $h_{cr} = 50$ nm. The final radius was measured as $R = 2.7 \mu\text{m}$ (based on the area of the coalesced inclusion) using the same analysis as before (e.g. Figure 5.8). The interfacial tension was not measured for our system, but enters linearly into eq (5.1). Song et al. (Faraday Discussion, 2013) measured the interfacial tension between aqueous PEG-400 and aqueous AS at a RH = 82% as $\gamma = 1.07 \text{ mN}\cdot\text{m}^{-1}$. Using this as order of magnitude, we obtain a viscosity of $\eta = 11 \text{ Pa}\cdot\text{s}$. However, for the C6 + C7 /AS /Water system, they estimated the interfacial tension as $0.05 \text{ mN}\cdot\text{m}^{-1}$. Taking this value will yield a viscosity of $0.55 \text{ Pa}\cdot\text{s}$. The results for all the coalescence events during this experiment are given in Table 5.2.

Table 5.2. Measured viscosity of the organic-rich phase using the model of McGuire (1996).

Temp – Event #	Coalescence occurrence time (s)	RH ($\pm 3\%$)	Coalescence relaxation time t_c (s)	Viscosity of organic-rich phase η (Pa·s)	AS diffusivity D_{AS} ($10^9 \text{ cm}^2 \text{ s}^{-1}$)
20.7 – 1	402	73	13.3	2.9 - 58	0.0075 – 0.15
20.7 – 2	533	72	3.8	0.40 - 8	0.055 – 1.1
20.7 – 3	568	72	7.1	0.65 - 13	0.036 - 0.71
20.7 – 4	693	71	4.8	0.55 - 11	0.039 – 0.78
20.7 – 5	891	70	8.5	0.37 - 7.4	0.060 – 1.2
20.7 – 6	1078	69	46.3	0.75 - 15	0.029 – 0.58
15.8 – 1	630	60	58.8	0.80 - 16	0.028 – 0.55

The viscosity values correspond to inclusions in Experiment #1 at 20.7°C and in Experiment #12 at 15.8°C. Fifth column: AS diffusivity calculated from viscosity (column 4) by means of the Stokes-Einstein relationship. Note that viscosity range is based on two interfacial tension values given by Song et al., 2013.

All data at 20.7°C in Table 5.2 agree with each other within about a factor of two, except the very first coalescence event, which involves the smallest inclusions located close to the edge of the particle and is therefore considered the least accurate measurement. The contrast in the images is very low at the edges of the particle making the size determination more difficult and leading to higher uncertainty. The average viscosity is 11 Pa·s, when excluding the first coagulation event. This value may be compared to the viscosity of α -pinene SOM determined by the “bead-mobility” technique, Renbaum-Wolff et al.(2013) obtained values of about $6 \cdot 10^2$ Pa·s for the water soluble SOM at 70% RH, while Song et al. (2016) obtained about 15 Pa·s for toluene derived SOA at 70% RH. The only coagulation event of the 15.8 °C

experiment relaxing to spherical shape yielded a viscosity of 16 Pa·s which is larger but not significantly larger compared to the data obtained at 20.7 °C.

It is difficult to assess the accuracy of the obtained viscosities, as we did not test our method against any standards. While we believe the order of magnitude should be correct, the method still needs to be tested in a system in which the viscosity has been determined with independent methods.

In column 5 of Table 5.2, we show diffusivities of AS based on the Stokes-Einstein relationship:

$$D_{AS} = \frac{kT}{6\pi\eta R_{AS}} \quad (5.2)$$

Here, D_{AS} is the diffusion coefficient for AS ions, k is the Boltzmann constant, T is temperature in Kelvin, η is the dynamic viscosity of the matrix, and R_{AS} is the hydrodynamic radius of AS. The hydrodynamic radius was taken as 0.237 nm [Marcus, 1988]. The obtained diffusivities will be further discussed in the following section.

5.3.6. Quantification of ammonium sulfate diffusivity in organic-rich particle shell

The rather complex evolution of the geometry of the inorganic phase inclusions including the coalescence events makes it difficult to quantitatively model their growth over the entire experiment. However, the initial growth of the first nucleated inclusions can be used to estimate the diffusivity of the ammonium sulfate ions in the early phase of the mixed inorganic/organic matrix.

To illustrate these considerations, Figure 5.10 shows the growth of the four individual inclusions analyzed previously for Experiment #12 at 15.8 °C and 0.55% RH min⁻¹ (see Figure 5.8) in terms of equivalent radii of the single inclusions that are

shown in Figure 5.3. The area of the inclusion as detected in the frames was determined using the “ImageJ” software [Schneider et al., 2012] and converted to equivalent radius by assuming a spherical shape for the early morphology of the inclusions.

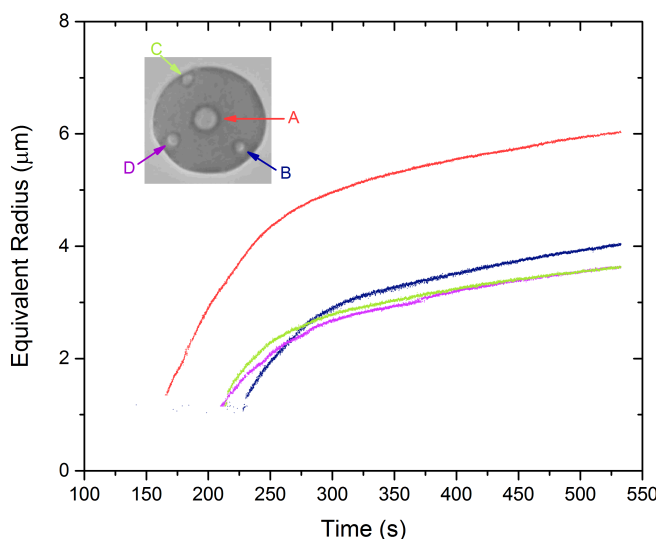


Figure 5.10. Equivalent radius during formation, and initial growth of individual inclusions due to diffusive uptake of ammonium sulfate in the particle shown in Figure 5.3 (Experiment #12 at 15.8°C and 0.55% RH min⁻¹) before the first coalescence event (i.e. Frame 5.3e). Times are identical to those in Figure 5.3. Inserted photo identifies inclusions by a color code. The center inclusion is the largest, marked by a red arrow and referring to the red equivalent radius curve.

Note that the automatic sizing algorithm detects a large background of small inclusions in almost all frames. However, based on the position of the grown inclusions at advanced times, the spurious hits can be easily rejected based on their center of gravity position. Figure 5.10 shows the initial growth phase of the four inclusions using the automatic rejection. Once the inorganic phase inclusion has grown beyond approximately 1.5 μm radius the data allow consistent sizing and hence the determination of initial growth rates. To interpret the rates we use the well-known composition of the mixed droplet before the first nucleation of the inorganic

phase, with the OIR from preparing the stock solution and the water content from RH. We assume water diffusivity to be fast enough to ensure thermodynamic equilibrium between gas-phase water vapor and condensed phase water (which might be violated for the coldest experiments at 6°C, see above). Once the first inclusion of the inorganic phase nucleates after RH drops below SRH, a concentration profile for AS will form surrounding the inclusion. The concentration of AS just above the surface of the inclusion, C_s , is much smaller compared to the concentration of AS far away from the inclusion, C_∞ , which is close to the concentration before nucleation. This concentration gradient drives AS diffusion towards the inorganic inclusion. For estimating the diffusivity of AS we utilize the derivation by Maxwell (1878) for the growth of spherical particles by diffusion:

$$\frac{dr^2}{dt} = \frac{2 D_{AS} M_{AS}}{\rho} (C_\infty - C_s). \quad (5.3)$$

Here, D_{AS} is the diffusion coefficient of AS in the aqueous CA/AS solution, r is the radius of the inorganic inclusion, ρ is the density of the particle and M_{AS} is the molar mass of AS. C_∞ is the molarity (moles per volume) of AS far from the inclusion and is taken equal to the initial concentration of AS in the homogeneous particle before the formation of the second phase. C_s is the AS molarity in the organic-rich phase close to the liquid-liquid interphase. The value of C_s was estimated using the phase diagram of AS/CA/H₂O mixture and AIOMFAC model prediction [Zuend and Seinfeld, 2012; Zuend et al., 2008; AIOMFAC homepage: (<http://www.aiomfac.caltech.edu/>)]. The difference between AS concentration in the homogeneous particle and at the border of inorganic inclusion ($C_\infty - C_s$) is reported in Table 5.3. See supporting information for a detailed explanation regarding AS concentration estimation in the organic-rich phase after the onset of LLPS.

Note that the concentration gradient in AS leads to a concentration gradient in carminic acid and to a lesser degree in water as well. In this sense the derived AS diffusivity represents an averaged diffusivity in the ternary mixture. Figure 11, shows the initial growth of inclusion A of Figure 5.10, plotted as r^2 versus time to calculate D_{as} according to eq (5.2). The fit was done for the first 100 s to isolate its growth from the competition with the other inclusions, which are being nucleated then.

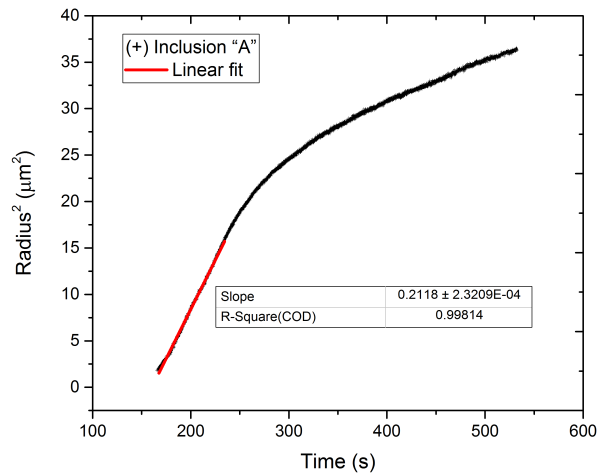


Figure 5.11. Square of radius, r^2 , of inclusion “A” in Figure 5.10 plotted as a function of time (Experiment #12 at 15.8°C and 0.55% RH min⁻¹). The red line is a linear fit to the first 100 s of growth data.

We estimated the value of C_∞ using AIOMFAC water activity calculations [Zuend and Seinfeld, 2012; Zuend et al., 2008; AIOMFAC homepage: (<http://www.aiomfac.caltech.edu/>)] of the ternary mixture of AS/CA/H₂O (OIR = 1:3). Water activity of the AS/CA/H₂O ternary system with OIR=1:3 as a function of water content predicted by AIOMFAC is plotted and included in the supporting information. The density of the ternary mixture is based on assuming ideal mixing of the pure compound densities.

As discussed above, growth of the first inclusion that starts to form the second phase will be the most reliable one for estimating AS diffusivity, because here the AS

concentration far from it is still very close to the originally prepared mixture. We took the first inclusion in experiments performed at different temperatures and in addition all four inclusions in Figure 5.10 for calculating the initial growth rates for different conditions (otherwise similar to the linear regression in Figure 5.11 and using eq 5.2). The results are summarized in Table 5.3.

Table 5.3. AS diffusivity values from the initial growth of individual inclusions.

Inclusion	$T(^{\circ}\text{C})$	RH ($\pm 3\%$)	$d\text{RH}/dt$ (RH%/min)	$dr/dt(10^9$ $\text{cm}^3\text{s}^{-1})$	$C_{\infty} - C_s(10^3$ $\text{mol cm}^{-3})$	D_{AS} ($10^9\text{cm}^2\text{s}^{-1})$
A (Fig. 5.10)	15.8	66	-0.55	2.13	1.19 ± 0.15	9.4 ± 3.9
B (Fig. 5.10)	15.8	66	-0.55	1.02	1.19 ± 0.15	4.5 ± 1.9
C (Fig. 5.10)	15.8	66	-0.55	1.08	1.19 ± 0.15	4.8 ± 2.0
D (Fig. 5.10)	15.8	66	-0.55	0.75	1.19 ± 0.15	3.3 ± 1.4
1 st inclusion (Fig. 5.4)	15.8	69	-0.76	1.20	0.88 ± 0.16	7.2 ± 3.3
1 st inclusion (Fig. 5.5)	20.7	74	-0.34	0.22	0.28 ± 0.22	12.7 ± 11.1
1 st inclusion (Fig. 5.6)	6.2	62	-0.54	2.16	1.60 ± 0.13	7.0 ± 2.6

All inclusions in the experiment performed at 15°C and the first inclusion formed at the other experiments performed at different temperatures and drying rates.

The diffusivities D_{AS} listed in Table 5.3 differ by about a factor of two between the experiments at the lowest (6°C) and highest temperature (20.7°C). As expected, D_{AS} decreases with decreasing temperature although the drying rates are different for all these experiments. While the differences imposed by temperature overlap within the uncertainty range of our measurements note that the uncertainty in diffusivity comes from limited knowledge of the AS concentration at the surface of the inclusion (C_s). This will shift the absolute value of AS diffusivity but will not influence the trend. In addition, we observe a lower diffusivity at lower RH, which may be caused by the

increase in viscosity with lower water content. Hence, both temperature and RH could be responsible for the observed trend in diffusivity.

Clearly the growth of the first inclusion in the experiment performed at 15.8°C with the lower drying rate yielded the fastest diffusivity when compared with those derived from the subsequently nucleated inclusions. The matrix becomes more depleted in AS with time and it becomes more viscous with decreasing water content, which slows the diffusion of AS in the organic-rich phase. In addition there is competition between inclusions. One exception is inclusion “D” in Figure 5.10, which shows lower diffusivity for AS compared to inclusions “C” and “B” that are formed later. The reason for this observation might be due to the location of inclusion “D” in the particle being very close to the rim and hence having less AS available in its immediate surroundings. In addition to that, it is in closer proximity to inclusion “A”, which is the first one to form and grow at a faster rate compared to the other ones. Indeed, competition between separate inclusions growing simultaneously may influence their growth behavior. Therefore, subsequently we consider only the diffusivities derived from the initial growth of the first inclusion.

The experiment run with a faster drying rate at 15°C yielded a value for the AS diffusivity which agrees within 20% with the experiment with the lower drying rate. This is well within the experimental uncertainties.

Literature data are available for AS diffusivity in aqueous solution at 25°C, with the binary mutual diffusion coefficient for infinitely diluted solutions being $1.53 \times 10^5 \text{ cm}^2 \text{ s}^{-1}$, which reduces to $0.98 \times 10^5 \text{ cm}^2 \text{ s}^{-1}$ at a concentration of 1.0 mol/L [Leaist and Hao, 1992] Tracer diffusion experiments for sulfate ion diffusivity in AS aqueous solution with 1.0 mol/L at 25°C yielded a value of $0.869 \times 10^5 \text{ cm}^2 \text{ s}^{-1}$ [Tanaka, 1988] Diffusivity of the sulfate and ammonium ions in marine sediment mud at 20°C were determined as $5.0 \times 10^6 \text{ cm}^2 \text{ s}^{-1}$ for the sulfate and $9.8 \times 10^6 \text{ cm}^2 \text{ s}^{-1}$ for the ammonium ion [Krom and Berner, 1980]. There are a few studies available in literature that focus on diffusivity for a single component in a matrix representative for organic aerosol

[e.g. Abramson et al., 2013; Bateman et al., 2016; Kidd et al., 2014; Lu et al., 2014; Marshall et al., 2016; Pajunoja et al., 2014, 2015; Perraud et al., 2012; Yatavelli et al., 2014; Zhang et al., 2015; Bastelberger et al., 2017]. Abramson et al. (2013) estimated the diffusion rate of pyrene in SOA at dry condition and room temperature to be $2.5 \times 10^{17} \text{ cm}^2 \text{ s}^{-1}$. In a recent study, Chenyakin et al. (2017) measured the diffusion coefficients of three fluorescent organic dyes (fluorescein, rhodamine 6G and calcein) in a sucrose/H₂O binary matrix for several water activities at room temperature. The diffusion coefficients at 38% RH were determined to be $1.5 \times 10^{14} \text{ cm}^2 \text{ s}^{-1}$, and $7.7 \times 10^{14} \text{ cm}^2 \text{ s}^{-1}$, and $1.9 \times 10^{13} \text{ cm}^2 \text{ s}^{-1}$, respectively.

Although these studies did not use the same system and conditions to investigate diffusivity in organic matrices, they still can provide a comparative framework. Compared to these studies, the diffusivity of AS in CA in our model system is much closer to water diffusivity in different organic systems measured previously [Zobrist et al., 2011; Lienhard et al., 2014; Steimer et al., 2015; Lienhard et al., 2015] than the diffusivity of a single organic component in an organic aqueous mixture. This may not be surprising as the phase separation happens at considerably high relative humidities where water acts as a plasticizer compared to those studies cited above, which were measured under dry conditions.

A comparison of the diffusivities at 15°C derived from growth rates and summarized in Table 5.3 with the ones derived from viscosity via the Stokes-Einstein relation in Table 5.2 reveals that the Stokes-Einstein-derived D_{as} is smaller by a factor of 10 - 475 ($(0.028 - 0.55) \times 10^9 \text{ cm}^2 \text{ s}^{-1}$ vs. $(9.4 \pm 3.9) \times 10^9 \text{ cm}^2 \text{ s}^{-1}$). Three possible reasons could explain this discrepancy:

(i) the uncertainties in our diffusivity and viscosity data are based on estimations of the properties of the system, so that a fair fraction of the discrepancy might simply be due to the uncertainty estimations of the properties;

(ii) the difference might be partly due to a pronounced RH-dependence of AS diffusivity, when taking into account that as the viscosity measurements are

performed under slightly drier conditions than the inclusion growth measurements (albeit only by a few % RH);

(iii) there might be a failure of the Stokes-Einstein relation in the AS/CA system, similar to other systems where such a breakdown was demonstrated and shown to be particularly important for small diffusing molecules [e.g., Bastelberger et al., 2017].

It appears to be unlikely that the discrepancy in AS diffusivities could be explained by any single one of the above reasons, but possibly a combination of (i), (ii), and (iii).

5.4. Atmospheric implications

Our values of the AS diffusivity in aqueous CA solutions may be used to investigate whether kinetic limitations could prevent LLPS to occur under tropospheric conditions in submicron particles larger than 100 nm. Since we measured the diffusivity only over a limited temperature range we extrapolate those data to lower, atmospherically relevant temperatures by assuming different values for an Arrhenius type diffusion activation energy [e.g., Lienhard et al., 2015]. Our data indicates a diffusion activation energy of about 35 kJ/mol. We also plot in Figure 5.12, the Smith and Kay (1999) water diffusivity temperature dependence shifted in absolute value to our data point of AS diffusivity at 15°C. There, the temperature dependence is based on a Vogel-Fulcher-Tammann (VFT) parameterization, which deviates from an Arrhenius temperature dependence but may be considered as a lower limit estimate for the temperature dependence nature of the aqueous AS/CA system. For an estimate of the upper limit of the temperature dependence we followed Angell (and used again a VFT parameterization which is still consistent with our data but with temperature dependence more representative of a „fragile“ liquid [Angell, 1988]). The red lines in Figure 5.12 show the characteristic timescales for a nucleated AS-rich phase to grow to a 100 nm radius inclusion calculated from eq (5.3) and assuming an aerosol to behave like our CA/AS/H₂O-system. We have chosen 100 nm, because this is about as large as inclusion can get at most in typical atmospheric aerosol particles

in the accumulation mode. Clearly, from these extrapolations LLPS is not going to be kinetically delayed even under cold, upper tropospheric conditions. We believe this conclusion is valid for most of the mixed organic/inorganic aerosol for which LLPS is predicted from thermodynamic considerations [Zeund et al., 2011; Song et al., 2012a; You et al., 2014]. This is because, first, CA is a highly functionalized compound and rather at the higher end of molecular mass of atmospherically relevant compounds, and viscosity in general scales with molecular mass and functionalization [Koop et al. 2011, Rothfuss and Petters, 2017]. Second, the SRH of the system we studied is rather at the lower end of relative humidities observed in atmospherically relevant model systems as well as atmospheric samples Song et al., 2012; Song et al., 2013; You et al. 2014]. For example You et al. (2012) found an SRH > 90% for SOM collected at Atlanta in the summer. At higher RH, the water content in aerosol phase is higher and the viscosity is lower because of the plasticizing effect of water.

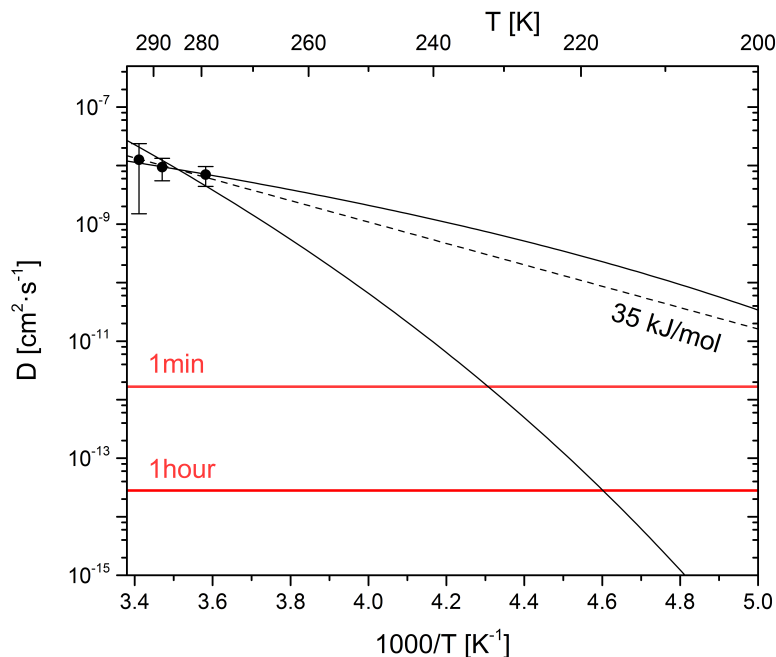


Figure 5.12. Temperature dependence of AS diffusivities in organic matrices similar to carminic acid. Data points with error bars: this work is based on the growth measurements (Section 5.3.6). Dashed black line: Arrhenius extrapolation of the measured AS diffusivities to lower temperatures corresponding to a diffusion activation energy of 35 kJ/mol. Upper solid black line: shifted VFT temperature dependence of water diffusion (Smith and Kay, 1999). Lower solid line: diffusion activation energy taken from Angell (1988), and VFT parameterization to highlight the upper bound temperature dependence diffusion activation energy more representative of a „fragile“ liquid. Red lines: times of 1 minute and 1 hour required to grow an inclusion of 100 nm radius of the AS-rich phase after nucleation.

The argument developed above can be used to speculate about the morphology of atmospheric particles in general. There are two issues to consider here. The first one is the number of inclusions that will form. As it takes less than a minute at $T = 220$ K to grow an inclusion to a 100 nm radius size, the depletion of AS in the organic-rich phase will be fast and likely prevent further nucleation of the salt-rich phase. Hence, in contrast to the super-micrometer sized particles in our experiments we expect aged atmospheric particles in accumulation-mode range to have most likely a single inclusion. Because of the relatively strong Kelvin effect at these sizes, even if two or more inclusions would nucleate, the smaller ones would quickly merge into the larger

ones. The second question regards the morphology of this phase-separated particle. Since the atmospheric implication section focuses on the aged aerosol particles, the O:C ratio will be high enough to result in a core-shell morphology rather than partially engulfed (see the Faraday Discussion on this very matter).

5. Conclusions

The morphology of micrometer sized AS/CA/H₂O particles depends on both temperature and drying rate. Lowering the temperature and increasing the drying rate will both inhibit the formation of spherical core-shell and to a greater extent the final coalescence of all inclusions to one inorganic aqueous phase. The growth of a single AS inclusion can be used to estimate the diffusivity of AS in the CA/AS/H₂O matrix. The diffusivities estimated from AS inclusion growth were compared with the ones derived from viscosity and show that either the Stokes-Einstein relation underestimates AS diffusivity in an AS/CA/H₂O matrix, and/or the diffusivity is an extremely strong function of water activity, and/or the uncertainties of our experiments cause a bias towards too high viscosities. Calculating the impacts this might have on a submicron particle with a diameter equal or greater than 100 nm shows that for aerosols with the organic/inorganic composition similar to our model system, the formation of LLPS is very feasible even at low temperatures with respect to designated diffusion activation energy and the life-time of tropospheric aerosols. For submicron atmospheric particles larger than 100 nm, we conclude that the most likely morphology is a core-shell since the AS diffusion is sufficiently fast to lower supersaturation with respect to the formation of the second liquid phase and will likely prevent further nucleation after the first inclusion formed.

Appendix 5.1: Estimating the concentration of AS in the organic phase after LLPS

For calculating ammonium sulfate diffusivities in section 5.3.7 the concentration difference between the concentration of AS in the mixed phase before phase separation and the equilibrium concentration after phase separation needs to be estimated, see eq. (5.3). We measured SRH for 4 different organic to inorganic ratios upon drying, see Fig. 5.A1.

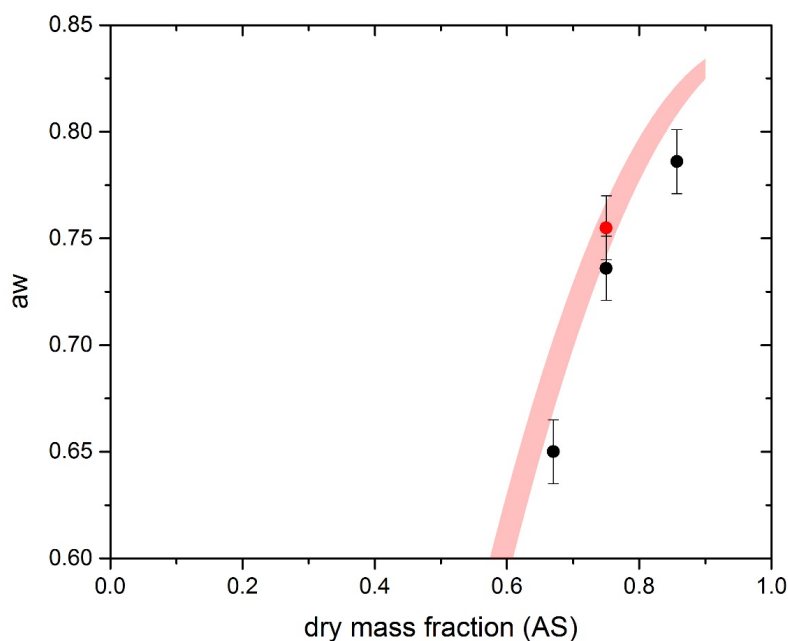


Figure 5.A1: SHR as measured upon drying for different OIR (black dots) of the CA/AS/H₂O-system. Transition water activity from phase separated to a homogeneous, one-phase mixed particle upon humidification (red dot). Estimated phase boundary between one-phase liquid to two liquid phases (red shaded area).

These data show a strong composition dependence of SRH indicating that the system may be completely miscible for particles with high enough carminic acid content. (Experiments with a dry mass fraction of AS equal to 0.33 were inconclusive whether LLPS occurred as the strong absorption of the carminic acid led to very low contrast of the microscopic images.) For the OIR 1:3 case we measured in addition the

transition from phase separated to one phase upon humidification. This yielded a higher water activity compared to the SRH of the same composition as expected for LLPS occurring through nucleation and growth. However, both values of water activity –SRH and transition upon humidification– agreed within error of the humidity sensor. Since capacitance sensors for humidity always show some hysteresis (Li et al., 2000), estimation of the thermodynamic phase boundary between the miscible and phase separated region of the phase diagram carries some uncertainty. We performed an estimation based on fitting the SHR data using several 2nd order polynomials and shifting those according to the observed difference in SHR between drying and humidifying for the OIR 1:3 experiment (red shaded region in Fig. 5.A1).

We used the prediction of AIOMFAC (<http://www.aiomfac.caltech.edu>) for the water content for the homogeneous system prior to LLPS. For estimating the concentration of AS in the organic phase at the phase boundary to the second phase, we read the dry mass fraction of AS from Fig. 5.A1 and take the water content at the observed RH once more from AIOMFAC predictions. The estimated error for the concentration difference entering eq. (5.3) becomes particularly large for the experiment performed at 20 °C (RH=73.6 %) as there is little concentration difference in AS between the mixed particle and the concentration in the organic phase after phase separation. For the experiments at lower temperature the observed SHR decreased so that this concentration difference becomes more significant. (Note, that we assume the phase diagram to be temperature independent for the small temperature difference of our experiments.) The concentration differences estimated using this procedure are reported in Table 5.3.

Chapter 6

Radiative impact of liquid-liquid phase separation for aerosol containing a molecular absorber such as “Brown Carbon”

This chapter is in preparation for submission to Atmospheric Chemistry and Physics
M. M. Fard, U. K. Krieger, and T. Peter

Abstract

We investigate the optical properties of accumulation mode (0.1 – 1 μm) “brown carbon” particles (BrC) containing ammonium sulfate (AS) and absorbing organic carbon (OC). Here, we use a modified eccentric core-shell Mie code to calculate the absorption and scattering efficiencies of liquid-liquid phase separated (LLPS) accumulation mode particles containing aqueous AS as engulfed phase and absorbing aqueous OC as engulfing phase. The calculations were done for different imaginary parts of the index of refraction representing BrC particles of different organic to inorganic mass ratio (OIR) with different range of absorptivities. The ratio of optical efficiencies for the LLPS particle over the homogenous case was calculated to determine the extent to which LLPS might impact the optical properties of mixed aerosols. We show that this change can be captured by a simple correction factor, which may be implemented in global models to take into account the existence of two-phase particles instead of treating all the particles as homogeneous or concentric core-shell. The largest LLPS impact on the scattering efficiency Q_{scat} of our model system at $\lambda = 355$ nm was close to 50% and resulted from a highly absorbing ($k = 0.168$) case where the organic fraction had the lowest contribution in the mixed particle (OIR = 1:4). This

effect of LLPS reduces substantially, namely to 11.8%, after integrating over the full solar spectrum. We show that the concentric core-shell model is a good approximation for treating phase-separated particles for the OIR range relevant to atmospheric aerosols, and in worst case the deviation of Q_{scat} from the result for an eccentric particles is 2.8%.

6.1. Introduction

Among many other impacts, atmospheric aerosols influence the radiation budget of the Earth directly through scattering and absorption (and less importantly emission) of incoming shortwave solar and outgoing infrared radiation. Aerosols can also affect climate indirectly through their interaction with clouds. Depending on their optical properties, aerosols contribute mostly to the cooling of our planet [IPCC, 2013], but when they are highly absorptive (e.g., soot) may also contribute to warming [e.g. Ramanathan et al., 2001]. Anthropogenic aerosols are dominated by sulfate, organic carbon, black carbon (soot), nitrate and dust. According to the fifth Intergovernmental Panel on Climate Change report [IPCC, 2013], anthropogenic aerosols produce a net cooling effect, with a total direct radiative forcing of -0.27 [-0.77 to $+0.23$] Wm^{-2} and an indirect cloud albedo forcing of -0.55 [-1.33 to -0.06] Wm^{-2} . Despite dedicated research efforts, aerosols remain one of the main sources of uncertainty for climate prediction.

Although organic aerosol particles are mainly characterized as only scattering as they are largely transparent in the visible region of the solar spectrum, a significant fraction of carbonaceous aerosols absorb solar and terrestrial radiation. Black carbon (BC) is by far the most well known absorbing component of the atmospheric aerosols, which strongly absorbs light over a broad wavelength range from UV to IR. It has only been in recent years that a new class of organic matter was identified, which exhibits significant though weaker absorptive properties compared to BC. This absorbing fraction of organic matter is referred to as Brown Carbon (BrC) [Ramanathan et al., 2005; Pöschl, 2005; Andreae and Gelencser, 2006; Laskin et al., 2015]. In contrast to BC, the absorptivity of BrC has a very strong wavelength dependence with high absorption in the near-UV, but absorption decreasing rapidly towards longer wavelengths [Andreae and Gelencser, 2006; Bond and Bergstrom, 2006; Ramanathan et al., 2007; Feng et al., 2013; Laskin et al., 2015]. Several studies have suggested that at shorter wavelength, BrC can significantly contribute to the total aerosol

absorption or even dominate it in certain geographic regions [Yang et al., 2009; Bond et al., 2011; Zhang et al., 2011; Chung et al., 2012; Feng et al., 2013; Laskin et al., 2015]. Despite recent interest and extensive research regarding the impact of BrC on radiative forcing [e.g., Arnott et al., 2003; Ramanathan et al., 2007; Alexander et al., 2008; Lack and Cappa, 2010; Lang-Yona et al., 2010; Nakayama et al., 2010; Lack et al., 2012; Ma and Thompson, 2012; Feng et al., 2013; Langridge et al., 2013; Saleh et al., 2013; Tang et al., 2016], the magnitude of BrC absorption as well as its wavelength dependence is not yet well-established and its assignment to different sources and its oxidation lifetime is far from being fully characterized.

In addition to the limited knowledge associated with the optical properties of organic carbon, our current understanding with respect to aerosol compositions, physical state, and morphology is insufficient to accurately quantify the direct radiative effect of such aerosols. In particular, particle phase and morphology need to be investigated, since they influence the scattering and absorption of radiation [e.g., Baumgardner and Clarke, 1998; Martin et al., 2004; Lewis et al., 2009; Lack and Cappa, 2010]. Experiments and modelling studies have shown that as ambient relative humidity (RH) decreases, deliquesced aerosols can exist not only as a one-phase system containing organics, inorganic salts and water in a homogeneous mixture, but often as two-phase systems, where one aqueous phase is dominated by the organic material while the other aqueous phase is predominantly inorganic, e.g. containing inorganic salts [Pankow, 2003; Marcolli and Krieger, 2006; Ciobanu et al., 2009a,b; Bertram et al., 2011; Krieger et al., 2012]. This phenomenon is referred to as liquid-liquid phase separation (LLPS). In recent years, laboratory studies using model mixtures to represent tropospheric aerosols [Ciobanu et al., 2009; Bertram et al., 2011; Song et al., 2012a,b], or secondary organic aerosol (SOA) produced from smog chamber experiments [Smith et al., 2012] and filter samples collected during field measurement campaigns [You et al., 2012] imply that liquid-liquid phase separation (LLPS) is a common feature in mixed organic/inorganic particles. When two aqueous phases coexist in a particle, they may form different morphologies, such as core-shell or partially engulfed, depending on which configuration yields the lowest total surface free energy [Kwamena et al. 2010, Qiu and Molinero, 2015]. According to Song et al. (2012b and 2013), for aged aerosols with moderate to high oxygen-to-carbon (O:C) ratio, core-shell is the dominated morphology (see the Faraday Discussion on this very matter). Besides consequences for hygroscopicity (Hodas et al., 2015), a core-shell configuration will alter the optical properties of the particles in

particular for organic phases containing absorbing molecules, such as BrC.

Brown Carbon is referring to the light-absorbing fraction of the organic carbon that has a wavelength dependent absorptivity. Emission sources of BrC are not very well characterized. The primary emissions are mainly linked to biomass burning, smoldering combustion and biogenic emissions from humic matter, plant debris and other bio-aerosols [Andreae and Gelencser, 2006; Alexander et al., 2008; Chakrabarty et al., 2010; Kirchstetter and Thatcher, 2012]. Field measurements have also associated BrC to secondary organic aerosol (SOA) that form by gas to particle partitioning of semi-volatile organic compounds presenting in the biomass burning smoke [Hecobian et al., 2010; Saleh et al., 2013]. As SOA ages through oxidation processes, it may become significantly more absorbing in the near-UV region of the solar spectrum [Bones et al., 2010; Updyke et al., 2012, Laskin et al., 2015, George et al., 2015], implying that heterogeneous chemistry producing BrC in the condensed phase.

Despite the fact that the presence of LLPS has been observed and studied by a number of research groups, its impact on the radiative properties of mixed aerosol particles with molecular absorbers has so far not been quantified. In previous optical modeling studies, mostly focusing on the optical properties of particles containing soot inclusions, typically volume mixing approximations for the optical properties were employed or the morphology were assumed to be that of a spherical symmetric, concentric core-shell. In this paper, we apply a Mie-code developed for calculating the scattering properties of a non-symmetric cluster of spheres [<http://eng.auburn.edu/users/dmckwski/scatcodes/>] to calculate the ratio in optical efficiencies between homogeneous and phase-separated particles. We vary size, absorptivity of BrC, organic to inorganic ratio over ranges typical for aged atmospheric aerosol in the accumulation mode and show first, that the average optical efficiencies of an ensemble of phase separated particles with a random eccentric inclusion are well represented by those calculated for a simple concentric core shell particle. Second, we take advantage of this finding and calculate the radiative forcing caused by phase separated aerosol particles relative to homogeneously mixed once in a thin aerosol layer approximation [Nemesure and Schwartz, 1998].

6.2 Model system & methodical approach

6.2.1 Eccentric versus concentric core shell computations

As discussed above, we first want to discuss the difference in scattering and absorption accounting for differences in morphology for liquid-liquid phase separated particles. In

particular, we investigate the difference between a symmetric core shell morphology compared to one with an eccentric inclusion. To represent typical aged atmospheric aerosol containing BrC we choose the inorganic salt to be ammonium sulfate, representing the most abundant inorganic salt in continental aerosols, and light-absorbing organic carbon material representing BrC. We choose to study three organics to inorganic ratios (OIR), 1:4, 1:1, and 4:1, from inorganic rich to organic rich, which cover the typical range observed with aerosol mass spectrometry (AMS) [Zhnag et al., 2007].

To account for the absorptivity of BrC values the imaginary part of the refractive index (k) for BrC are taken from various studies [Kirchstetter et al., 2004; Chen and Bond, 2010; Feng et al., 2013] that measured k for different SOA at different locations, spanning a wide range from non-absorbing organic material ($k = 0$) to highly absorbing organic matter ($k = 0.168$ at 355 nm). The real part of the refractive index (n) for BrC at dry condition is taken as 1.65 [Hoffer et al., 2006]. We use simple volume mixing to calculate the size of the core relative to the shell for the different OIRs (see Fig. 1) as well as to calculate the refractive indices for the homogeneous particles.

For about 20 years numerical calculations for scattering and absorption of a host sphere containing a non-concentrically positioned smaller sphere have been feasible. In particular, the T-matrix approach of [Mackowski, 1996 and Mishchenko, 2011] solves the problem of obtaining random-orientation properties of clusters of spheres in a numerically efficient manner. In our context, it has been applied in recent years for computing scattering and absorption of morphologically complex soot containing aerosol [e.g., Mishchenko et al., 2013, Cheng et al., 2014]. Here, we use the Multiple Sphere T Matrix (MSTM) version 3.0 [Mackowski, 2013, (<http://eng.auburn.edu/users/dmckwski/scatcodes/>)] to compute fixed and random oriented scattering and absorption cross sections as well as the asymmetry parameter for eccentric core shell liquid-liquid phase separated aerosol with a molecular absorber in the organic phase.

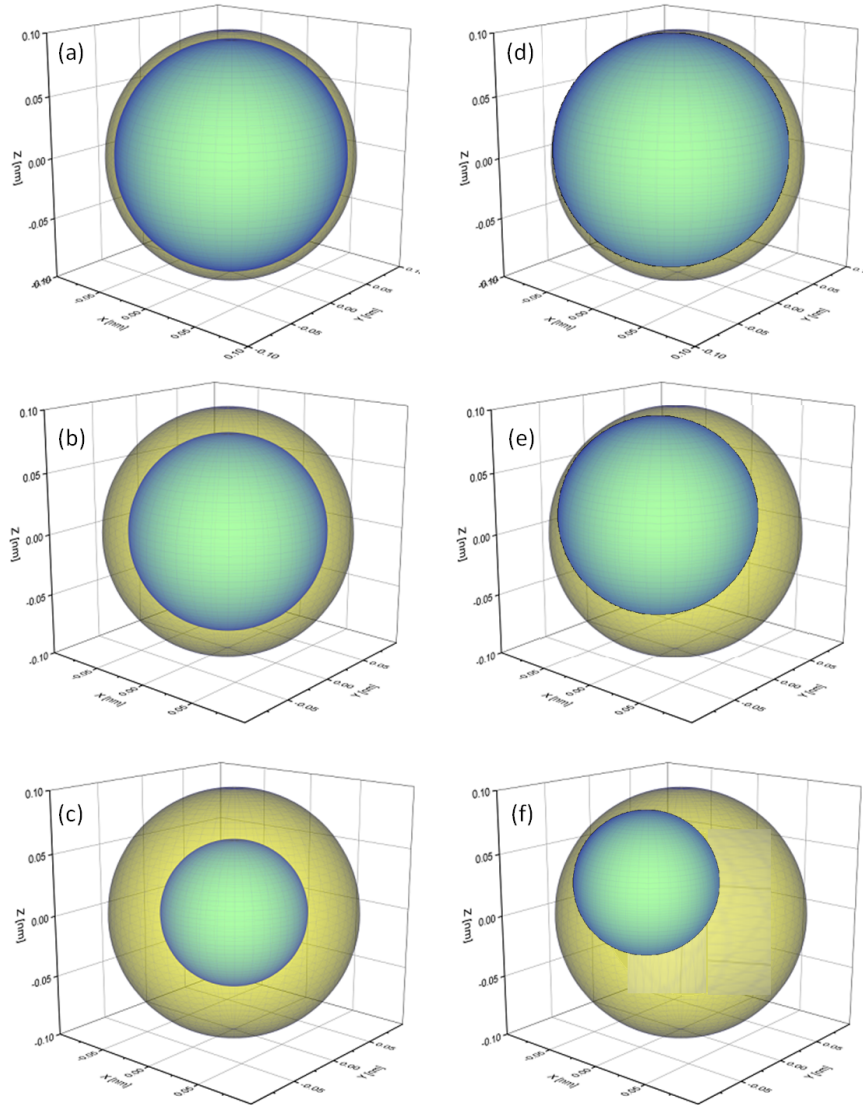


Figure 6.1: Schematic of a phase separated particle with a 75 nm radius to illustrate the thickness of the organic shell at (a): OIR = 1:4, (b): OIR = 1:1, and (c) OIR = 4:1 for concentric core-shell morphologies. (d)-(f) same for a single realization of an eccentric core-shell morphology. The calculations in this work use typically 500 such realizations, randomly oriented (with different distances of the inclusion from the center of the particles and different azimuth and polar angles). The direction of incoming light is along the z-axis.

The computational costs of calculating cross sections increase substantially, when going from highly symmetric core shell morphology, to a given eccentric core position relative to the incident light, and even more when random orientational averaging with random positioning of the core within the shell volume is required. Hence, we investigate systematically how the mean of the computed cross sections for the eccentric morphologies differs from the cross

section for concentric morphology. We performed this comparison for particles with properties ranging within the limits of OIR, size and absorptivity discussed above.

First, we used the MSTM code with random positioning of the center of the inorganic core within the organic shell to check how many realizations of fixed positions are needed for convergence of the mean cross sections. Figure 6.2(a) shows the distribution of scattering efficiency (Q_{scat}) for a particular choice of particle parameters comparing 10000 (locations) realizations (red columns, which refer to the Q_{scat} of individual particles with their core located at different positions within the volume of the shell) with 500 realizations (green columns).

Scattering efficiency (Q_{scat}) is expressed as the ratio of the scattering cross-section, σ_{scat} to the geometrical cross-section of the particle, $\sigma_{\text{geometric}}$:

$$Q_{\text{scat}} = \frac{\sigma_{\text{scat}}}{\sigma_{\text{geometric}}}$$

For spherical particles with radius r , $\sigma_{\text{geometric}} = \pi r^2$.

As illustrated in Fig. 6.2(b) the mean shows that neither scattering efficiencies nor the corresponding standard deviations differ much when increasing the number of realizations beyond 100. The same holds true for absorption efficiencies. Conservatively, in the following we use 500 different positions of the inclusion within the particle to determine the averaged Q_{scat} and Q_{abs} for the particles with eccentric core-shell morphology.

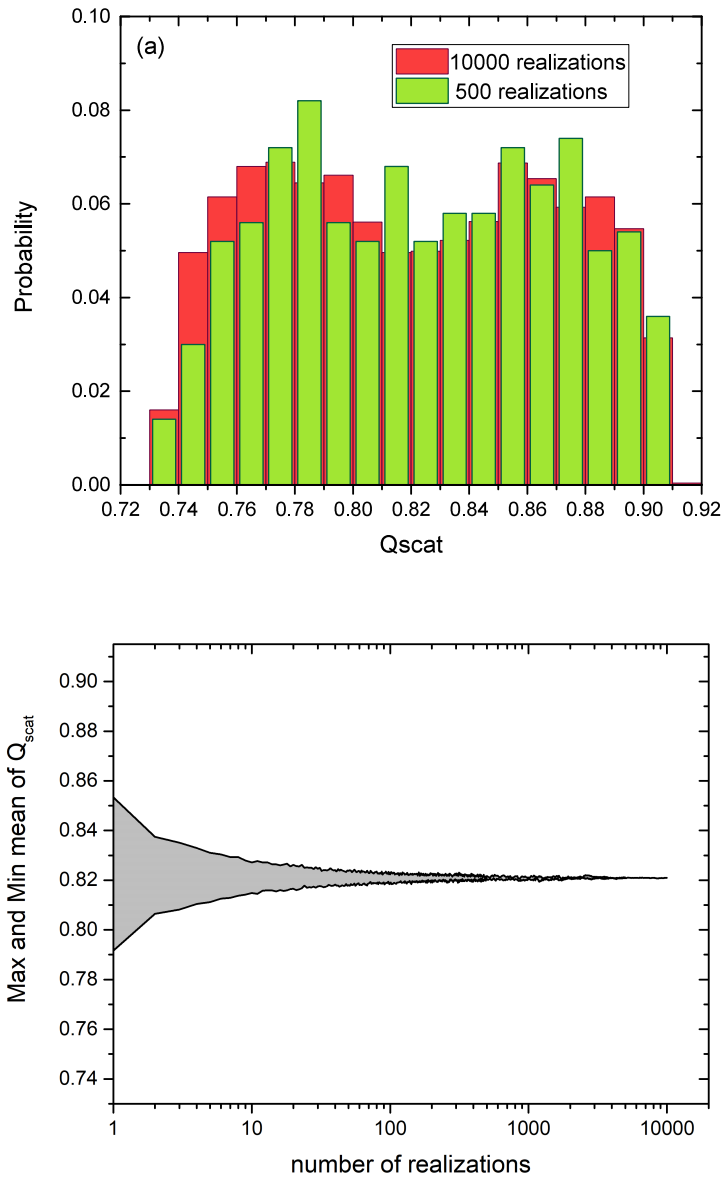


Figure 6.2 Panel (a): Probability distribution of Q_{scat} for a phase separated particle with the eccentric core positioned at 500 random locations (green columns) and 10000 random locations (red column) within a 100 nm particle at OIR = 1:4 and $k = 0.168$. Panel (b): Comparison of the calculated mean value for Q_{scat} of the same particle as in panel (a) for different numbers of realizations including 2, 5, 50, 100, 200, 500, 2000, 5000 and 10000 calculations.

It is evident from Fig. 6.2(a) that there is a significant change in scattering efficiency with the position of the center of the inclusion as the width of the distribution is more than 20 % of the

mean of the scattering efficiency. Figure. 6.3 depicts a plot of Q_{scat} versus the x , y , and z -axis positions of the core center, with the incident light along the z -axis. Obviously, the scattering efficiency changes significantly with the position of the core along the incoming light axis. It is smallest for the core position facing the incoming light and largest with the core being located at the opposing position to the incoming light with an almost linear dependence for at least this particular set of parameters. The almost linear dependence of the efficiency along the light axis and random dependence perpendicular to it suggests that a concentric core-shell calculation of the scattering efficiency may be an excellent approximation for the mean of a mono-disperse particle ensemble with random eccentric positions. In addition it suggests that the mean of the efficiency for an inclusion randomly distributed in the volume of the particle is not very different from one where the inclusion sticks to the surface of the particle at random positions.

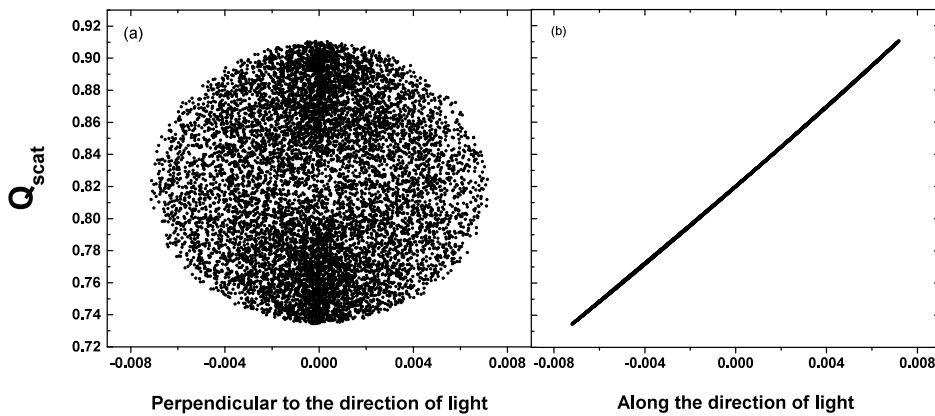


Figure 6.3 The change in Q_{scat} perpendicular to the direction of light (panel a) and along the direction of light (panel b) for particle with OIR = 1:4, $k = 0.168$, $r = 100$ nm over 10000 realizations.

For this particular particle, this is really the case as Fig. 6.4 shows the scattering efficiency for the average eccentric morphology as well as the one for a concentric core-shell with the standard deviation on an enlarged scale. The mean values for eccentric core-shell (with its center randomly placed in the volume) and eccentric core-shell (with its center position randomly placed such that it touches the surface) are very close and only differ in the 4th decimal place and the value for concentric core-shell is about 0.5% lower. This emphasizes that the concentric core-shell model may be a good approximation for calculating the mean

value for a distribution of particles with randomly located eccentric cores within either volume or surface for the OIR range and refractive indices typical of aged aerosol and particles in the accumulation size range. Let us note parenthetically, that very similar behavior is exhibit when plotting the absorption efficiency instead of the scattering efficiency.

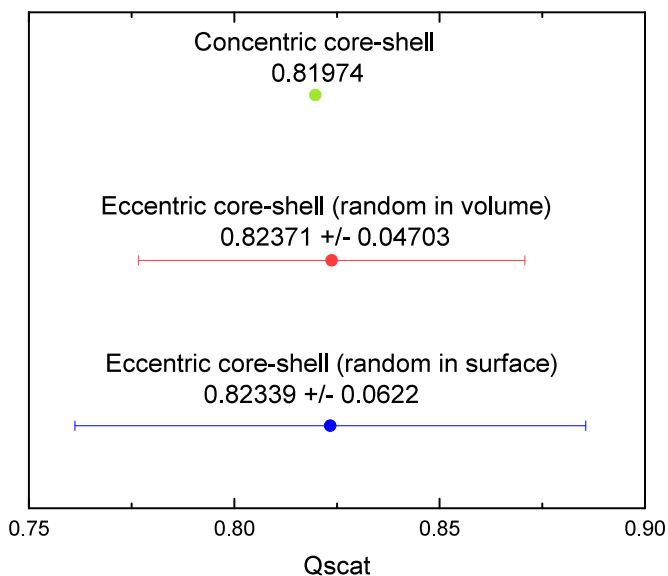


Figure 6.4 Q_{scat} mean value for eccentric core-shell (over 10000 realizations) within the volume (blue dot), Q_{scat} mean value for eccentric core-shell (over 10000 realizations) on random surface (red dot), and Q_{scat} for concentric core-shell (green dot).

6.3 Results & discussions

To test this hypothesis over a wide parameter range, we compare mean scattering and absorption efficiencies for particles with eccentric core-shell morphology (with the inorganic core randomly placed at 500 different positions within the volume of the particle) with the corresponding concentric core-shell morphology.

The efficiencies for scattering and absorption are strongly dependent on the size of the particle [Bohren and Huffman, 1998; Van de Hulst, 1957] for accumulation mode particles. This is illustrated in Fig. 6.5 for a case with $k = 0.168$, and OIR = 1:4. Here, the homogeneous particle is more efficient in absorbing the incoming light as particle size is

increasing compared to the phase-separated one. In contrast, the phase-separated particle scatters light about 20% more efficiently for particles above 400-nm diameter.

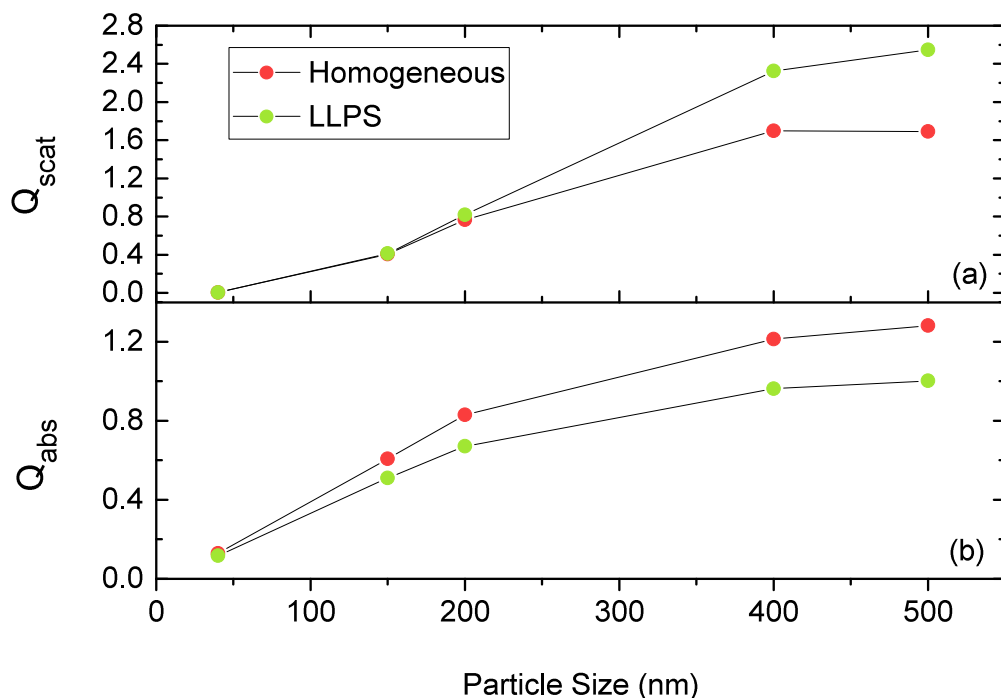


Figure 6.5 Q_{scat} (panel a), and Q_{abs} (panel b) calculated for phase separated (LLPS) and homogeneous particles ranging from 40-500 nm at OIR = 1:4, and $k = 0.168$ using the eccentric core-shell Mie-code at $\lambda = 355$ nm. The red and green dots show the results for the same system at specific particle size for homogenous and phase separated (LLPS) particles respectively. The lines are only meant to guide the eye.

Since we are interested in the impact of LLPS on aerosol scattering and absorption, we take the internally mixed, homogeneous particle as reference and plot in the following always the ratio of the LLPS morphology to the homogeneous particle for all calculated efficiencies. This way, the strong size dependence of the efficiencies seen in Fig. 6.5 for both morphologies cancels each other out and the emphasis is instead put on the effect of morphological change. These ratios can be understood as an empirical factor that could be used to correct calculations for homogeneous particles if those of equivalent phase separated particles are needed.

In Figure 6.6, we have plotted the ratio of scattering efficiencies for the LLPS morphology over the ones for the homogenous morphology. The analogous ratios for absorption efficiencies are plotted in the right column.

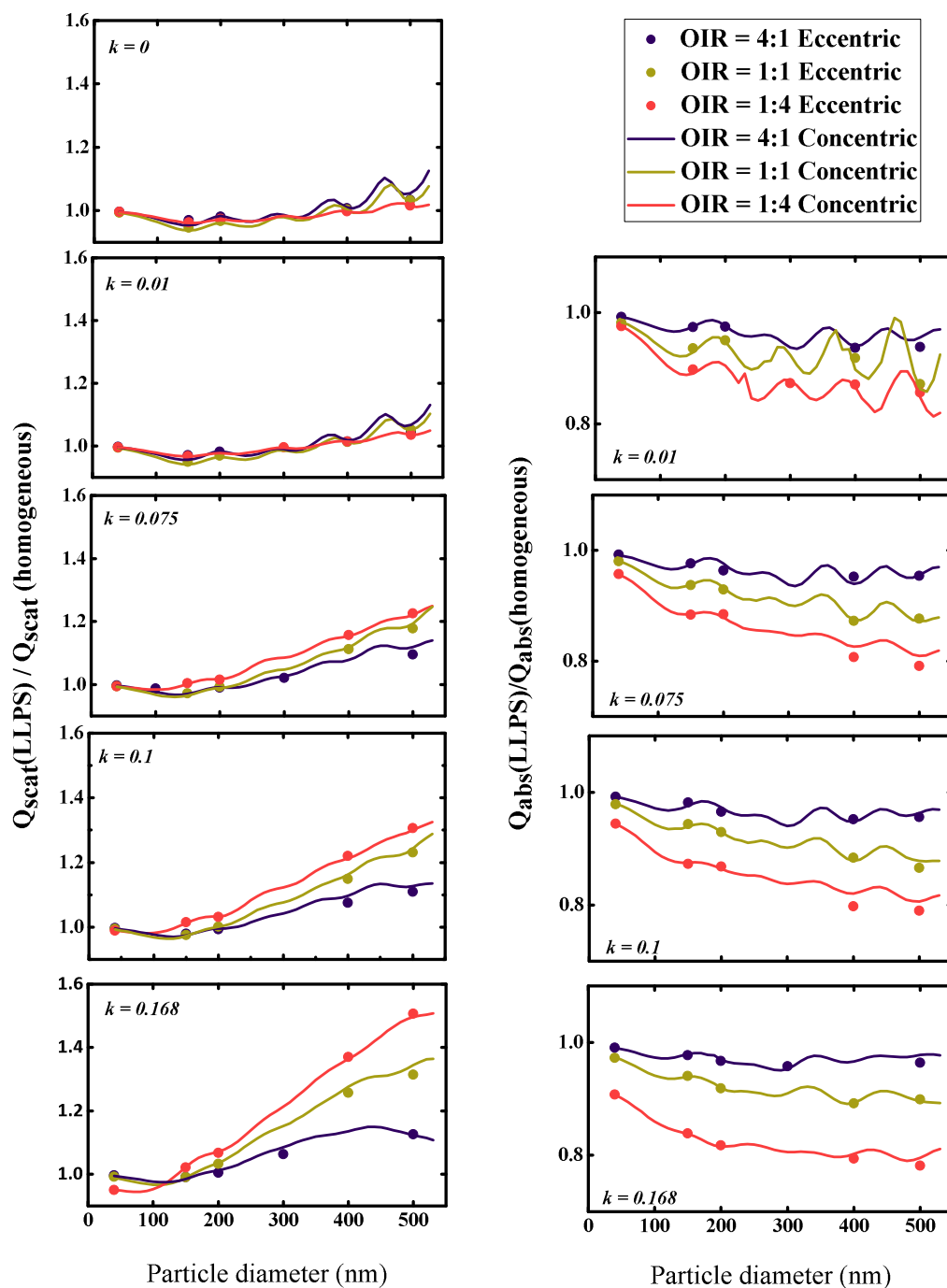


Figure 6.6 Left row: ratio of Q_{scat} of LLPS morphology Over homogenous morphology as function of particle diameter for OIR = 1:4, 1:1, 4:1, with increasing k from top to bottom, k

= 0, 0.01, 0.075, 0.1, and 0.168. Right row: corresponding absorption efficiency ratios. Symbols are calculations with random orientation of an eccentric core shell for the phase-separated particles; lines are calculations for the corresponding symmetric core-shell morphology.

Clearly, the effect of phase separation increases with particle size: the ratio of scattering efficiencies increases whereas the ratio of absorption efficiencies decreases. All calculations have been performed for a wavelength of 355 nm, hence particles much smaller than this wavelength are close to the Rayleigh scattering and become less sensitive to internal morphology. Hence, we expect all ratios to approach 1 for very small particle sizes. Also apparent are periodicities in both the ratio for scattering as well as the ratio of absorbing efficiencies showing a period with size of about 100 to 150 nm presumably related to half-integral ratios of size to wavelength. These dampen out with increasing absorptivity.

However, the overall effect of increasing absorptivity is to enhance the differences between phase-separated particles relative to homogeneous ones.

The most significant trend is the dependence of the efficiency ratios on the organic to inorganic ratio. For the absorption efficiency, the particles with the lowest organic volume (OIR = 1:4) show the strongest deviation for the LLPS morphology relative to the homogenous particle. As the organic fraction decreases in the particle, the effect of redistribution of the absorbing molecules into the organic phase yield a stronger contrast in the imaginary part of the refractive index between shell and core. This increase in contrast influences both absorption and scattering efficiency ratios.

Most importantly, the extensive comparison between mean of eccentric core-shell realizations with concentric core shell calculations indicate that a concentric core-shell model is sufficient for estimating the ratios between scattering and absorption efficiencies for particles smaller than 500 nm in diameter and the ranges in OIR, and absorptivity under consideration here. This approximation becomes less accurate with particle size but stays within 2.8% at maximum and is better than 1% for most of the parameter range under consideration here.

6.4. Atmospheric implications

In the previous section we showed that concentric core shell calculation are sufficient to approximate the radiative impact of LLPS for a typical atmospheric aerosol containing a molecular absorber like Brown carbon. Utilizing this insight allows us to perform integration over the UV-VIS part of the solar spectrum in a numerically efficient manner. In this section we calculate the ratio of radiative forcing caused by a phase separated versus a homogeneously mixed aerosol in the thin aerosol layer approximation for monodisperse aerosol.

6.4.1. The importance of looking at scattering cross-section

According to Nemesure and Schwartz (1998), the property that dictates the radiative impacts is the scattering cross-section and the up-scattering fraction.

In order to calculate the radiative forcing enforced by an optically thin aerosol layer, the following equation can be used:

$$\Delta F(\theta_0) = (F^\downarrow \cos \theta_0) (Q_{\text{ext}} \frac{1}{\cos \theta_0}) \omega \beta(\theta_0) C \Delta z \quad \text{Eq (6.1)}$$

Where, $(F^\downarrow \cos \theta_0)$ being the incident direct beam flux at the top of the scattering element, θ_0 being the solar zenith angle (SZA), Q_{ext} the extinction efficiency, ω the single scattering albedo, $\beta(\theta_0)$ the up-scatter fraction and C the concentration of the particles.

Since the extinction efficiency is the sum of scattering and absorption efficiencies, $Q_{\text{ext}} = Q_{\text{scat}} + Q_{\text{abs}}$, and the single scattering albedo is the ratio of scattering over extinction efficiencies:

$$\omega = \frac{Q_{\text{scat}}}{Q_{\text{scat}} + Q_{\text{abs}}} = \frac{Q_{\text{scat}}}{Q_{\text{ext}}} \quad \text{Eq (6.2)}$$

That simplifies equation (1) to:

$$\Delta F(\theta_0) = F^\downarrow Q_{\text{scat}} \beta(\theta_0) C \Delta z \quad \text{Eq (6.3)}$$

The up-scatter fraction, β , is a function of particle size and accounts for the asymmetry of the phase function. It has a value of 0.5 for small particle in Rayleigh regime and decreases as the

size of the particle increases. The up-scattering fraction for accumulation-mode particles ($0.1 \mu\text{m} < r < 1\mu\text{m}$) that dominates aerosols mass and light scattering properties in the atmosphere, β may be approximated for isotropic incoming radiation by $\beta = \frac{1}{2} (1 - \frac{7}{8} g)$ [Wiscombe and Grams, 1976], with g being the asymmetry parameter, i.e. the average cosine of the scattering angle ($g = \int_{4\pi} P \cos\theta d\Omega$, P being the normalized phase function). Since we are only interested in calculating the ratio of the radiative forcing for the LLPS morphology relative to homogenous morphology, we take this approximation for the up-scatter fraction and calculate the ratio as:

$$\text{Ratio } \Delta F = \frac{\int_{\lambda_1}^{\lambda_2} (F^\downarrow(\lambda) Q_{scat}^{LLPS}(\lambda) \beta^{LLPS}(\lambda)) d\lambda}{\int_{\lambda_1}^{\lambda_2} (F^\downarrow(\lambda) Q_{scat}^{Homo}(\lambda) \beta^{LLPS}(\lambda)) d\lambda} \quad \text{Eq (6.4)}$$

An example of the relevant factors of Eq. (6.4) are shown in Fig. 6.7 for a particle for which we expect a significant effect of morphology: its OIR is equal to 1:4, it has a diameter of 200 nm, an imaginary part of the refractive index of $k = 0.168$ at 355 nm and the wavelength dependence of the imaginary part of the refractive index is given by an Ångström exponent, AAE, equal to 2. The real part of the refractive index is parameterized as explained in Appendix 6.1.

6.4.2 Calculating the impact of LLPS on radiative forcing of a thin aerosol layer

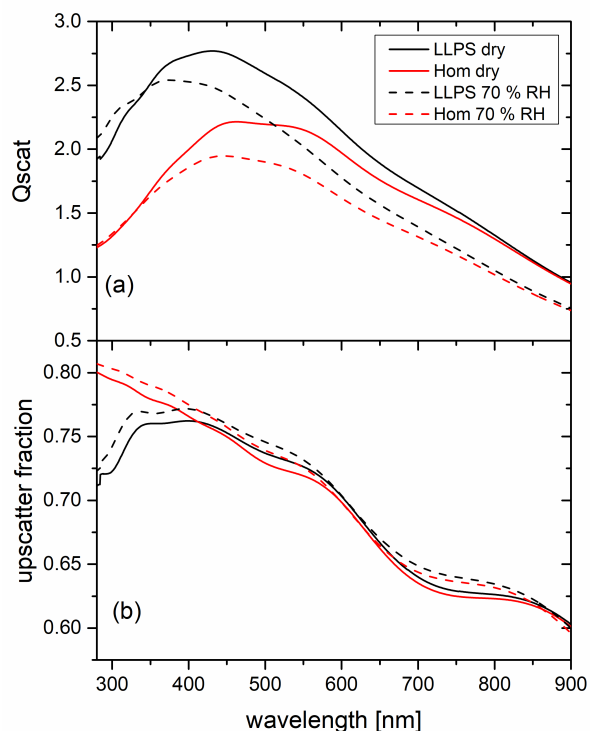


Figure 6.7 (a): Scattering efficiency for the homogeneous morphology (red) and LLPS morphology (black) under dry and wet conditions (solid and dashed line, respectively). (b): upscatter fraction for the homogeneous particle (red) and LLPS particle (black) under dry and wet conditions (solid and dashed line, respectively).

Panel (a) of Fig. 6.7 shows the scattering efficiency for both, dry conditions and at a relative humidity of 70%. As discussed in section 6.1, the LLPS morphology yields larger scattering efficiencies especially at shorter wavelengths (below 500 nm) at which the differences in refractive index between the morphologies are more significant. The up-scatter fraction shown in panel (b) for LLPS morphology is about 10% smaller than for the homogeneous morphology at near UV-wavelength ($\lambda = 290$ nm) but they merge for the wavelengths above 400 nm.

According to Eq (6.4), the product of up-scatter fraction and scattering efficiency multiplied by the incoming radiation and integrated over the solar spectrum for LLPS morphology and homogeneous morphology yields a “Ratio” that quantifies the effect of particles with LLPS morphology on radiative forcing relative to those with homogeneous morphology. This ratio

is shown as a function of particle radius under dry and wet (70% RH) conditions in Figs. 6.8 (a) and 6.8 (b) respectively.

These calculations were done as in the example of Fig. 6.6 but for different scenarios with OIR = 1:4, 1:1, 4:1, $k = 0, 0.1, 0.168$. The AAE value is equal to 2. This corresponds to highly absorbing BrC and will give the largest radiative forcing impact possible by mixed BrC particles.

For this part, we used Lorenz-Lorenz relation [Born & Wolf, 1959] to estimate the real part of the refractive index of our mixture containing AS and absorbing organic matter at different OIR and as a function of wavelength at dry condition and 70% RH. The calculation of the real part is explained explicitly in Appendix 6.1.

The data for spectral irradiance was taken from ASTM G173-03 (<http://rredc.nrel.gov/solar/spectra/am1.5/>). For more details, please see Appendix 6.2.

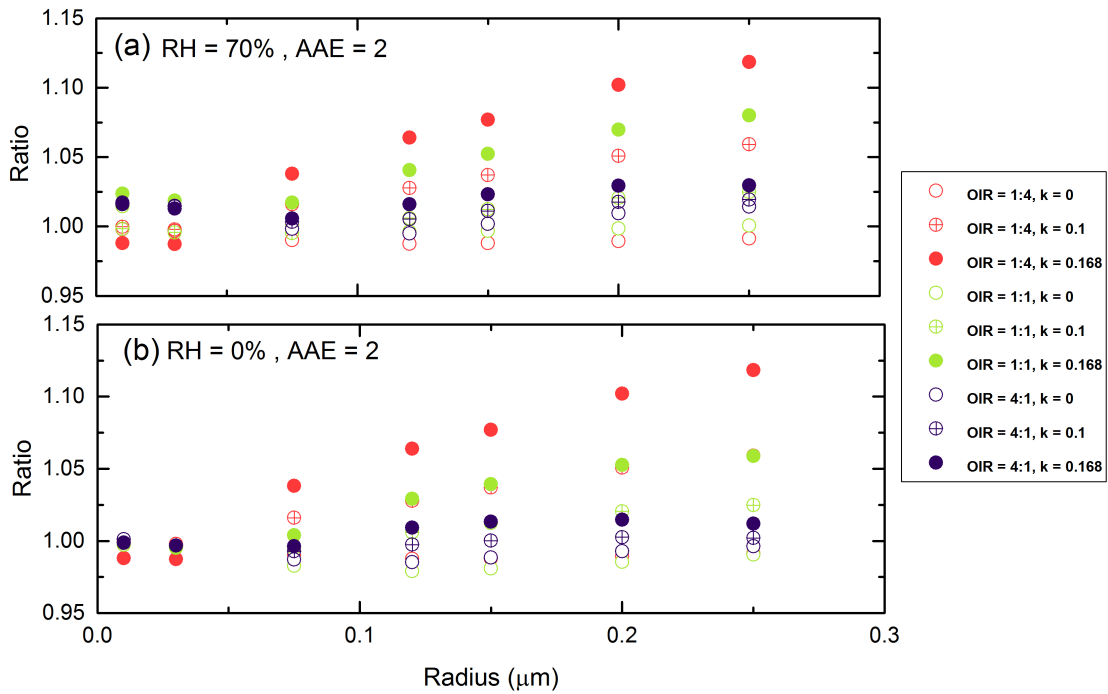


Figure 6.8 Ratio of radiative forcing of LLPS to homogenous case under 70% RH (a) and dry condition (b).

As illustrated in Fig 6.8, the overall result is not much different for the dry and wet condition. At dry condition, there is more overlap of data where the ratio is lower but the general pattern is quite the same. As expected for accumulation-mode particles, the greatest impact from LLPS contribution comes from the case where organic fraction is the lowest (OIR = 1:4) and k has the largest value (0.168). This corresponds to a factor of 11.8%, which could be implemented in global models, but is not significant compared to other uncertainties including BrC loading.

6.5. Conclusions

Using both eccentric and concentric core-shell model for a sample consist of AS and absorbing organic material at different OIRs and imaginary part values revealed that the concentric core-shell model is a good approximation for calculating optical properties of the phase separated particles of this specific system. The largest impact from LLPS on the Q_{scat} of our model system was close to 50% and resulted from the case where organic fraction had the lowest contribution in the mixed particle (OIR = 1:4) and formed a very thin shell around the inorganic core and was highly absorbing ($k = 0.168$). This factor reduces substantially to 11.8% after taking the full solar spectrum into account.

Appendix 6.1: Calculating the real part of refractive index

The real part of the refractive index for a liquid solution can be estimated in terms of the refractivity of the solution based on the Lorentz-Lorenz relation [Born & Wolf, 1959]. The refractivity to a good approximation is a linear superposition of the molar refractivities of the solution's components. While refractive index data as well as density data are available for aqueous ammonium sulfate solutions [Tang & Munkelwitz, 1994], we choose the refractive index and density parameterizations of Lienhard et al. [2015] to be representative for the SOM in our model calculations. As the molar refractivities depend strongly on wavelength, we parameterize the SOM molar refractivity wavelength dependence based on the parameterization given in Liu et al. [2013] and the ones for aqueous ammonium sulfate on the parameterization by Semmler and Koop. Finally, we use ideal mixing of the two binary systems to calculate the refractive index of the ternary system.

The resulting refractive indices for the ternary system with different OIR under dry conditions are shown in Fig. 6.A1.

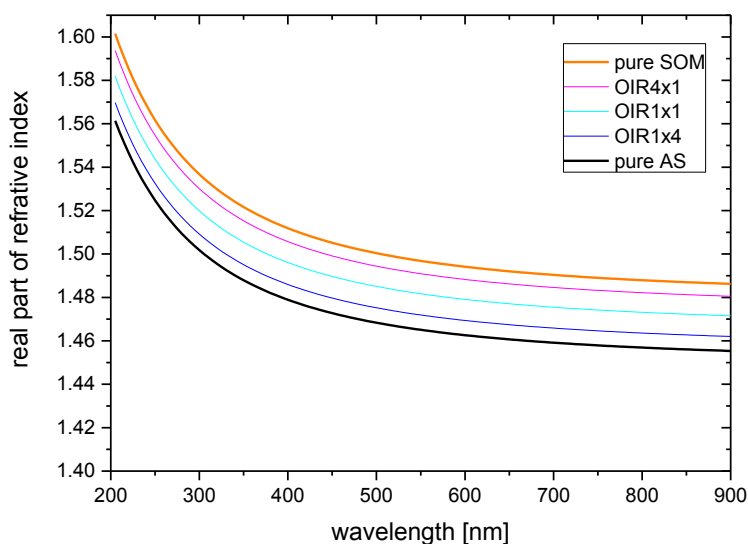


Fig. 6.A1: Real part of refractive index for mixtures of AS and SOM with varying OIR containing no water.

binary aqueous solutions for AS [Tang & Munkelwitz, 1994] and SOM [Lienhard et al. 2015] and the Zdanovskii-Stokes-Robinson (ZSR) relation to calculate the water content of the mixture. This yields the refractive indices shown in Fig. A2.

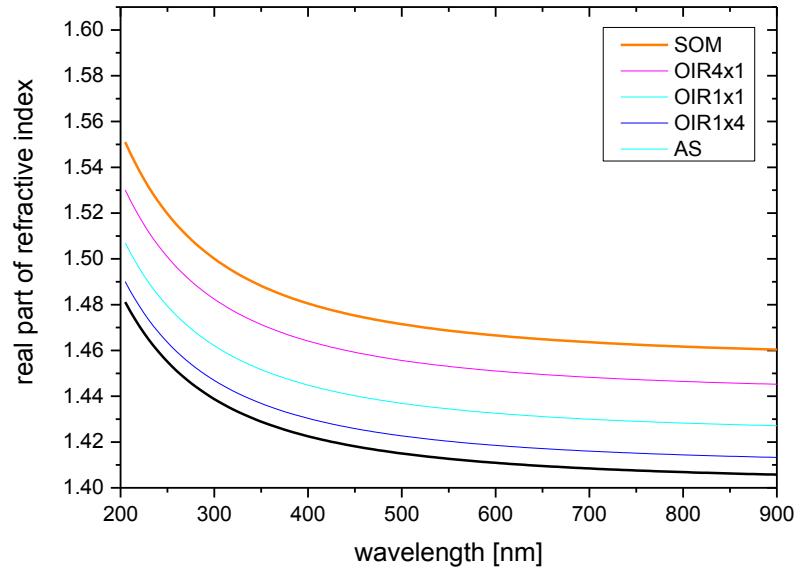


Fig. 6.A2: Real part of refractive index for mixtures of AS and SOM with varying OIR at 70% RH.

Under humid conditions the real part of the refractive index decrease and, since AS takes up more water at 70% compared to SOM, the difference in refractive index between AS rich mixtures to SOM rich mixtures increases when comparing humid to dry conditions.

Appendix 6.2: Spectral Irradiance

For calculating the shortwave radiative forcing ratio defined in eq. 6.4, spectral irradiance is needed as an input for performing the integration. Since we are interested in estimating the relevance of LLPS for radiative forcing and calculating only a ratio, the particular choice of irradiance data is not very important. We use the ASTM G173-03 as spectral irradiance, which is plotted in Fig. 6.B1:

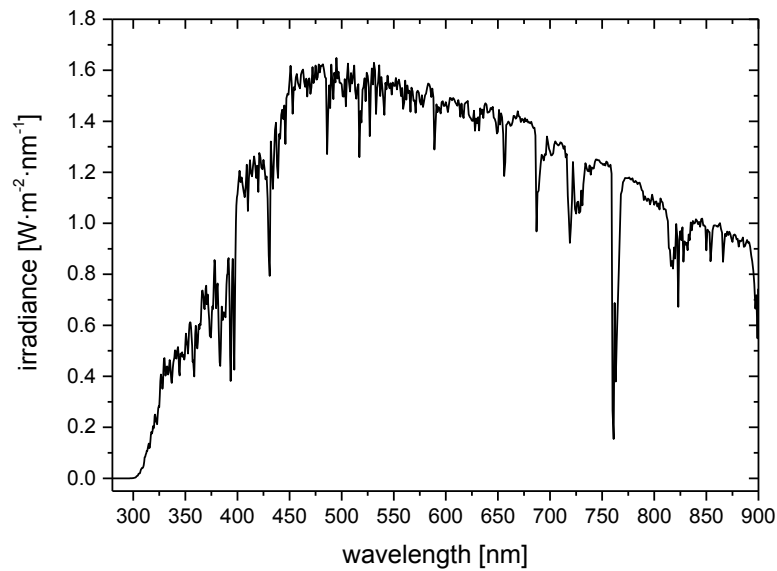


Fig. 6.B1: Direct spectral irradiance (ASTM G173-03).

The irradiance is for a solar zenith angle of 41.81° , the atmospheric conditions are those of the standard US atmosphere with an ozone column of 340 DU and total column water vapor equivalent of 1.42 cm. The irradiance is considered to be a reasonable average for the 48 contiguous states of the U.S.A. over a period of one year.

Chapter 7

7. Summary and Final remarks

This PhD work mainly focused on investigating the morphology and optical properties of mixed aerosol particles exhibiting liquid-liquid phase separation (LLPS).

7.1. Kinetic limitations to inorganic ion diffusivity and to coalescence of inorganic inclusions in viscous liquid-liquid phase separated particles

In chapter 5, we investigated the morphology of ammonium sulfate / carminic acid / H₂O model system (AS/ CA/ H₂O) for droplets between 40 – 75 μm in diameters using optical microscopy coupled to a relative humidity and temperature controlled flow cell. For the first time, experiments were conducted at different temperatures and different drying rates to see the impact of these two factors on the morphology of phase separated particles. Our results revealed that the morphology of the mixed particles after the onset of LLPS strongly depends on the drying rate and less significantly on the temperature. At 20 °C, and a drying rate of 0.35% RH per minute, the AS inclusions forming the second phase coalesced and formed a spherical core-shell morphology. At the higher drying rate at 20°C, the final coalesced inclusion did not reshape to a spherical form. We believe that at higher drying rate, the matrix loses water at the higher rate and becomes more viscous and doesn't allow the AS inclusion to move and reduce its surface energy by forming a

spherical core-shell. At the lowest drying rate experiment (0.55% RH per minute) taken at 15 °C, the AS inclusions coalesced but did not form a spherical core due to higher viscosity of the matrix. As drying rate increases (0.76% RH per minute) at 15 °C, the AS inclusions did not coalesce at the final stage of the experiment and before efflorescence. Since the drying rate were not equal for each experiment, we conclude that a combination of drying rate and temperature resulted in higher viscosity of the organic matrix and limit the growth, coalesce, and reshaping of the AS inclusions. This phenomenon can be seen more clearly at the experiment conducted at 6 °C where the number of AS inclusions increases drastically most likely due to the reduced diffusivity of AS in a more viscous matrix, which in the absence of an neighbouring inclusion undergo higher supersaturations and are pushed to nucleate additional inclusions. In this experiment, except some early and minimal growth of initial inclusions, the number of coalescence events decreases massively and inclusions “freeze” in the matrix for about 40 min before efflorescence takes place.

Once two inclusions coalesce, the coalescence time for these inclusions to form a new spherical inclusion upon further drying provides an opportunity to estimate the viscosity of the organic phase using a coalescence model proposed by McGuire et al. (1996). Using this technique for the two experiments at 20 °C and 15 °C, the AS diffusivity was calculated using Stokes-Einstein relationship. All data for viscosity at 20 °C (except the first one that we believe is not the most accurate measurement) agree with each other within about a factor of two. The average viscosity at 20 °C (excluding the first coagulation event) is calculated to be 11 Pa·s. This value may be compared to the viscosity of α -pinene secondary organic material (SOM) determined to be $6 \cdot 10^2$ Pa·s by the “bead-mobility” technique (Renbaum-Wolff et al., 2013). The only coagulation event of the 15°C experiment that relaxed to a spherical shape yielded a viscosity of 16 Pa·s which is larger but not significantly larger than the viscosity value obtained for the experiment at 20 °C.

Since we have not tested our method against any known system, it is difficult to assess the accuracy of the calculated viscosities although the order of magnitude seems to be correct. One way to have a better feeling regarding the accuracy of McGuire approach, is to perform the technique to one our well studied systems of AS/PEG/H₂O where there are

a few number of coalescence events. The obtained viscosity from McGuire could be compared to the well-known viscosity of PEG matrix (98 mPa·s).

Furthermore, we used the initial growth of the first AS inclusion to estimate the average diffusivity of AS in our mixed model matrix using the derivation by Maxwell (Maxwell, 1877) for the growth of spherical particles by diffusion (eq 5.3). According to Table 5.2, AS diffusivity differ by about a factor of two for the experiments conducted at the lowest (6 °C) and highest temperature (20 °C). As expected AS diffusivity (D_{AS}) increases with temperature although the drying rates are different for all these experiments. Comparing the diffusivities tabulated in Table 2 for the experiment at 20°C, with the ones derived from viscosity (Table 1), indicate that Stokes-Einstein underestimates D_{AS} by a factor of ~ 30 ($9 \cdot 10^{-10} \text{ cm}^2 \cdot \text{s}^{-1}$ vs. $2.5 \cdot 10^{-8} \text{ cm}^2 \cdot \text{s}^{-1}$). The deviation was about the same for the experiment at 15°C ($5.5 \cdot 10^{-10} \text{ cm}^2 \cdot \text{s}^{-1}$ vs. $1.6 \cdot 10^{-8} \text{ cm}^2 \cdot \text{s}^{-1}$). We believe that the uncertainty involved in the viscosity measurements is about an order of magnitude and the uncertainty in estimating the diffusivity data is a factor of 5. Hence, it is difficult to decide if the Stokes-Einstein relationship holds for our system or not.

One must note that the impact of temperature on the onset of LLPS (SRH) was not one the objectives of our study. Hence, it would be interesting to include that in the future studies and find out if we come to the same conclusion that You and Bertram (2015) and Schill and Tolbert (2013) did that indicated no significant temperature dependence for SRH.

In future studies, it is suggested to run the experiments at different temperatures at the same drying rate to be able to compare the resulted morphology in a more sensible fashion. It is also important to extend the temperature range to lower values to cover the whole troposphere. The limitation of our current setup does not allow to conduct experiments at temperatures lower than 5 °C. In order to go to temperatures below zero, we need to increase the flow rate of the cooling liquid into the cell but the flow is limited by the internal diameter of the tubes that the cooling liquid is running through. We also need to avoid dew formation on the optical windows. There must be a closed cavity between the optics and the window on the cell where pure N_2 can flow in and prohibit the formation of dew. The ventilation bias that is illustrated in Figure 5.5.6 needs to be

optimized to have a homogenous flow over the whole particle at low temperatures and high drying rates.

The partial phase diagram data (OIR = 1:2, 1:3, 1:6) of AS/ CA/ H₂O shows a strong composition dependence of SRH indicating that the system may be completely miscible for particles with high CA content. For the OIR 1:3 case, we also measured the transition from phase separated to one phase upon humidification which gave a higher water activity compared to the SRH of the same composition as expected for LLPS through nucleation and growth. Although both water activity values agreed within the uncertainty of the humidity sensor, it is important to measure the water activity upon humidification for OIR = 1:2, and 1:6 and compare the values to the SRH (onset of LLPS upon drying). This will reduce the uncertainties regarding the AS concentration in homogenous particle and right before LLPS and offers a more accurate value for AS diffusivity using eq (5.3).

7.2. Radiative impact of liquid-liquid phase separation for aerosol containing a molecular absorber

In chapter 6, we calculated optical efficiencies of a mixed AS/ BrC/ H₂O mixed system for submicron particles at organic to inorganic ratios (OIR) relevant for mixed inorganic/organic atmospheric particles (OIR = 1:4, 1:1, 4:1) at $\lambda = 355$ nm. The calculation was done for homogenous and phase separated particles using both eccentric and concentric core-shell morphologies. The main objective of this project was to determine the magnitude of the change that a phase-separated particle could impose on optical properties of aerosols compared to a homogenous case. In addition to the traditional concentric core-shell approach, we also used an eccentric core shell code in which the inorganic core is positioned at more than 500 positions in the volume of the organic shell or slightly touch the surface. One important finding was that the comparison between concentric and eccentric core-shell model revealed that the concentric core-shell is quite a good approximation for calculating the ratio of Q_{abs} and Q_{scat} for particles smaller than 500 nm in diameter and within the range of OIR used in our experiment.

Our results show that both absorption and scattering efficiencies (Q_{abs} , and Q_{scat}) are a function of particle size. In our model system, the homogeneous particles show higher efficiency for light absorption whereas the phase separated particles were more efficient to scatter light especially for particles above 400-nm in diameter.

Since we were only interested in the impact of LLPS on the radiative properties of aerosols, we calculated the ratio of absorption and scattering efficiencies for LLPS to homogenous case for particles in our model system at different OIRs and values for imaginary part of refractive index (k).

The most significant trend observed was the dependence of Q_{abs} and Q_{scat} ratio on the OIR. Regarding absorption efficiency, the particles with the lowest organic volume (OIR = 1:4) show strongest deviation in Q_{abs} for the LLPS case relative to the homogenous particles. This trend is due to the fact that as the organic fraction decreases in the particle, the effect of redistribution of the absorbing molecules into the organic phase becomes more significant.

The calculations to estimate the potential impact of LLPS on direct radiative forcing for our AS /BrC /H₂O system yield a factor of 1.18 for the case with highest imaginary part ($k = 0.168$) and lowest OIR (OIR = 1:4).

Based on this study, it is safe to state that LLPS can be disregarded for particles below 50nm when volume mixing is used to calculate the real part of the refractive index of the homogeneous particle. Although the outcome might be very different if use Lorenz-Lorenz equation to calculate the real part of the mixed phase. The highest impact that LLPS might imposed on the radiative forcing of the particles consist of our model system is 11.8%. This gives a correcting factor that can be implemented in the global models to describe the physical state of mixed particles and their impact on radiative forcing in a more precise way.

Bibliography

- Abramson, E.; Imre, D.; Beranek, J.; Wilson, J.; Zelenyuk, A. Experimental Detection of Chemical Diffusion Within Secondary Organic Aerosol Particles. *Phys. Chem. Chem. Phys.* **2013**, 15, 2983–2991.
- AIOMFAC Home Page: <http://www.aiomfac.caltech.edu/> (accessed May 28, 2017).
- Albrecht, B. A. Aerosols, cloud microphysics, and fractional cloudiness. *Science*. **1989**, 245.4923, 1227-1230.
- Alexander, D. T.; Crozier, P. A.; Anderson, J. R. Brown carbon spheres in East Asian outflow and their optical properties. *Science*. **2008**, 321(5890), 833-836.
- Altaf, M. B.; Zuend, A.; Freedman, M. A. Role of Nucleation Mechanism on the Size Dependent Morphology of Organic Aerosol. *Chem. Commun.* **2016**, 52(59), 9220-9223.
- Andreae, M. O.; Crutzen, P. J. Atmospheric aerosols: Biogeochemical sources and role in atmospheric chemistry. *Science*. **1997**, 276(5315), 1052-1058.
- Andreae, M. O.; Gelencser, A. Black carbon or brown carbon? The nature of light-absorbing carbonaceous aerosols. *Atmos. Chem. Phys.* **2006**, 6, 3131-3148.
- Angell, C. A. Structural instability and relaxation in liquid and glassy phases near the fragile liquid limit. *J. Non-Cryst. Solids*. **1988**, 102, 205–221, DOI: 10.1016/0022-3093(88)90133-90140.
- Anttila, T.; Kiendler-Scharr, A.; Mentel, T. F.; Tillmann, R. Size Dependent Partitioning of Organic Material: Evidence for the Formation of Organic Coatings on Aqueous Aerosols. *J. Phys. Chem. A*. **2007**, 57, 215–237, DOI:10.1007/s10874-007-9067-9.
- Anttila, T.; Kiendler-Scharr, A.; Tillmann, R.; Mentel, T. F. On the reactive uptake of gaseous compounds by organic-coated aqueous aerosols: Theoretical analysis and application to the heterogeneous hydrolysis of N₂O₅. *J. Phys. Chem. A*. **2006**, 110(35), 10435-10443.
- Arola, A.; Schuster, G.; Myhre, G.; Kazadzis, S.; Dey, S.; Tripathi, S. N. Arola A, Schuster G, Myhre G, Kazadzis S, Dey S, Tripathi SN. Inferring absorbing organic carbon content from AERONET data. *Atmos. Chem. Phys.* **2011**, 11(1), 215-225.
- Arnott, W. P.; Moosmüller, H.; Sheridan, P. J.; Ogren, J. A.; Rasp, R.; Slaton, W. V.; Hand, J. L.; Kreidenweis, S. M.; Collett, J. L. Photoacoustic and filter-based ambient aerosol light absorption measurements: Instrument comparisons and the role of relative humidity. *J. Geophys. Res: Atmos.* **2003**, 108(D1).
- Bahadur, R.; Praveen, P. S.; Xu, Y.; Ramanathan, V. Solar absorption by elemental and brown carbon determined from spectral observations. *Proc. Natl. Acad. Sci. U. S. A.* **2012**, 109(43), 17366-17371.
- Barber, P. W.; Hill, S. C. *Light Scattering by Particles: Computational Methods*. World Scientific Publishing Co. Inc., Singapore, 1990.
- Bastelberger, S.; Krieger, U.; Luo, B.; Peter, T. Diffusivity Measurements of Volatile Organics in Levitated Viscous Aerosol Particles. **2017**.

- Bateman, A. P.; Gong, Z.; Liu, P.; Sato, B.; Cirino, G.; Zhang, Y.; Artaxo, P.; Bertram, A. K.; Manzi, A. O.; Rizzo, L. V.; Souza, R. A. Sub-micrometer Particulate Matter is Primarily in Liquid Form Over Amazon Rainforest. *Nat. Geosci.* **2016**, 9(1), 34-37.
- Bergstrom, R. W.; Russell, P. B.; Hignett, P. Wavelength dependence of the absorption of black carbon particles: Predictions and results from the TARFOX experiment and implications for the aerosol single scattering albedo. *J. Atmos. Sci.* **2002**, 59(3), 567-577.
- Bernsen, J. Dynamic Thresholding of Grey-level Images. *International conference on pattern recognition.* **1986**, 2, 1251-1255.
- Bertram, A. K.; Martin, S. T.; Hanna, S. J.; Smith, M. L.; Bodsworth, A.; Chen, Q.; Kuwata, M.; Liu, A.; You, Y.; Zorn, S. R. Predicting the Relative Humidities of Liquid-Liquid Phase Separation, Efflorescence, and Deliquescence of Mixed Particles of Ammonium Sulfate, Organic Material, and Water Using the Organic-to-sulfate Mass Ratio of the Particle and the Oxygen-to-carbon Elemental Ratio of the Organic Component. *Atmos. Chem. Phys.* **2011**, 11, 10995–11006, DOI:10.5194/acp-11-10995.
- Bluvshstein, N.; Flores, J. M.; Segev, L.; Rudich, Y. A new approach for retrieving the UV-vis optical properties of ambient aerosols. *Atmos. Meas. Tech.* **2016**, 9(8), 3477-3490.
- Bohren, C. F.; Huffman, D.R. *Absorption and scattering of light by small particles.* John Wiley & Sons. 2008.
- Bond, T. C. Spectral dependence of visible light absorption by carbonaceous particles emitted from coal combustion. *Geophys. Res. Lett.* **2001**, 28(21), 4075-4078.
- Bond, T.; Bergstrom, R. Light absorption by carbonaceous particles: An investigative review. *Aerosol Sci. Technol.* **2006**, 40(1), 27-67.
- Bond, T. C.; Zarzycki, C.; Flanner, M. G.; Koch, D. M. Quantifying immediate radiative forcing by black carbon and organic matter with the Specific Forcing Pulse *Atmos. Chem. Phys.* **2011**, 11(4), 1505-1525.
- Bond, T. C.; Doherty, S. J.; Fahey, D. W.; Forster, P. M.; Berntsen, T.; DeAngelo, B. J.; Flanner, M. G.; Ghan, S.; Kaercher, B.; Koch, D.; Kinne, S.; Kondo, Y.; Quinn, P. K.; Sarofim, M. C.; Schultz, M. G.; Schulz, M.; Venkataraman, C.; Zhang, H. Bounding the role of black carbon in the climate system: A scientific assessment. *J. Geophys. Res: Atmos.* **2013**, 118(11), 5380-5520.
- Bones, D. L.; Henricksen, D. K.; Mang, S. A.; Gonsior, M.; Bateman, A. P.; Nguyen, T. B.; Cooper, W. J.; Nizkorodov, S. A. *J. Geophys. Res.: Atmos.* **2010**, 115, No. D05203.
- Born, M.; Wolf, E. *Principles of Optics: Electromagnetic Theory of Propagation, Interference and Diffraction of Light.* Pergamon Press, 1959.
- Braban, C. F.; Abbatt J. P. A study of the phase transition behavior of internally mixed ammonium sulfate-malonic acid aerosols. *Atmos. Chem. Phys.* **2004**, 4(5), 1451-1459.
- Braban, C. F.; Carroll, M. F.; Styler, S. A.; Abbatt, J.P. Phase transitions of malonic and oxalic acid aerosols. *J. Phys. Chem. A.* **2003**, 107(34), 6594-6602
- Brodsky, D. M.; Georgopoulos, P. G. Growth and deposition of hygroscopic particulate matter in the human lungs. *Aerosol. Sci. Technol.* **2001**, 34(1), 144–159.

- Brooks, S. D.; DeMott, P. J.; Kreidenweis, S. M. Water uptake by particles containing humic materials and mixtures of humic materials with ammonium sulfate. *Atmos. Environ.* **2004**, 38(13), 1859-1868.
- Brooks, S. D.; Wise, M. E.; Cushing, M.; Tolbert, M. A. Deliquescence Behavior of Organic/ammonium sulfate Aerosol, *Geophys. Res. Lett.* **2002**, 29(19), 1917, DOI: 10.1029/2002GL014733.
- Baynes, T. S. The Encyclopaedia Britannica, *A Dictionary of Arts, Sciences, and General Literature*, C. Scribner's sons, New York, 9th edition, 1878, vol. 7.
- Cass, G. R.; Hughes, L. A.; Bhawe, P.; Kleeman, M. J.; Allen, J. O.; Salmon, L. G. The chemical composition of atmospheric ultrafine particles. *Phil. Trans. R. Soc. A* **2000**, 358(1775), 2581- 2592.
- Cavalli F, Facchini MC, Decesari S, Mircea M, Emblico L, Fuzzi S, Ceburnis D, Yoon YJ, O'Dowd CD, Putaud JP, Dell'Acqua A. Advances in characterization of size-resolved organic matter in marine aerosol over the North Atlantic. *Journal of Geophysical Research: Atmospheres*. 2004 Dec 27;109(D24).
- Caurie, M. Raoult's Law, Water Activity and Moisture Availability in Solutions *J. Food. Sci.* **1983**, 48(2), 648-649.
- Chakrabarty, R. K.; Moosmüller, H.; Chen, L. W.; Lewis, K.; Arnott, W. P.; Mazzoleni, C.; Dubey, M. K.; Wold, C. E.; Hao, W. M.; Kreidenweis, S. M. Brown carbon in tar balls from smoldering biomass combustion. *Atmos. Chem. Phys.* **2010**, 10(13), 6363-6370.
- Chan, H. K.; Eberl, S.; Daviskas, E.; Constable, C.; Young, I. Changes in lung deposition of aerosols due to hygroscopic growth: a fast SPECT study. *J. Aerosol. Med.* **2002**, 15(3), 307-311.
- Chang, E. I.; Pankow, J. F. Prediction of activity coefficients in liquid aerosol particles containing organic compounds, dissolved inorganic salts, and water - Part 2: Consideration of phase separation effects by an X-UNIFAC model. *Atmos. Environ.* **2006**, 40, 6422-6436.
- Charlson, R. J.; Schwartz, S. E.; Hales, J. M.; Cess, R. D.; Coakley, J. A.; Hansen, J. E.; Hofmann, D. J. Climate forcing by anthropogenic aerosols. *Science*. **1992**, 255, 423 – 430.
- Chenyakin, Y.; Ullmann, D. A.; Evoy, E.; Renbaum-Wolff, L.; Kamal, S.; and Bertram, A. K. Diffusion Coefficients of Organic Molecules in Sucrose–water Solutions and Comparison with Stokes–Einstein Predictions. *Atmos. Chem. Phys.* **2017**, 17, 2423–2435, DOI:10.5194/acp-17- 2423-2017.
- Chung, C. E.; Ramanathan, V.; Decremer, D. Observationally constrained estimates of carbonaceous aerosol radiative forcing. *Proc. Natl. Acad. Sci. U. S. A.* **2012**, 109(29), 116241-1629.
- Ciobanu, V.G.; Marcolli, C; Krieger, U.K.; Weers, U.; Peter, T. Liquid– liquid Phase Separation in Mixed Organic/inorganic Aerosol Particles. *J. Phys. Chem. A.* **2009**, 113, 10966-78.
- Ciobanu, V. G.; Marcolli, C.; Krieger, U. K.; Zuend, A.; Peter, T. Efflorescence of Ammonium Sulfate and Coated Ammonium Sulfate Particles: Evidence for Surface Nucleation. *J. Phys. Chem. A.* **2010**, 114, 9486-95.
- Clegg, S. M.; Abbatt, J. P. Oxidation of SO₂ by H₂O₂ on Ice Surfaces at 228 K: a Sink for SO₂ in Ice Clouds. *Atmos. Chem. Phys.* **2001**, 1, 73-78.

- Colberg, C.A.; Luo, B. P.; Wernli, H.; Koop, T.; Peter, T. A novel model to predict the physical state of atmospheric H₂SO₄/NH₃/H₂O aerosol particles. *Atmos. Chem. Phys.* **2003**, 3(4), 909-924.
- Corr, C. A.; Hall, S. R.; Ullmann, K.; Anderson, B. E.; Beyersdorf, A. J.; Thornhill, K. L.; Cubison, M. J.; Jimenez, J. L.; Wisthaler, A.; Dibb, J. E. Spectral absorption of biomass burning aerosol determined from retrieved single scattering albedo during ARCTAS. *Atmos. Chem. Phys.* **2012**, 12(21), 10505-10518.
- Cosman, L. M.; Bertram, A. K. Reactive Uptake of N₂O₅ on Aqueous H₂SO₄ Solutions Coated with 1-component and 2-component Monolayers. *J. Phys. Chem. A.* **2008**, 112, 4625-4635.
- Costabile, F.; Gilardoni, S.; Barnaba, F.; Di Ianni, A.; Di Liberto, L.; Dionisi, D.; Manigrasso, M.; Paglione, M.; Poluzzi, V.; Rinaldi, M.; Facchini, M. C. Characteristics of an aged organic “brown” aerosol in the urban Po Valley atmosphere. *Atmos. Chem. Phys. Discuss.* **2016**, 10.
- Decesari, S.; Facchini, M. C.; Fuzzi, S.; McFiggans, G. B.; Coe, H.; Bower, K. N. The water-soluble organic component of size-segregated aerosol, cloud water and wet depositions from Jeju Island during ACE-Asia. *Atmos. Environ.* **2005**, 39(2), 211-222.
- Decesari, S.; Fuzzi, S.; Facchini, M. C.; Mircea, M.; Emblico, L.; Cavalli, F.; ... & Artaxo, P. Characterization of the organic composition of aerosols from Rondônia, Brazil, during the LBA-SMOCC 2002 experiment and its representation through model compounds. *Atmos. Chem. Phys.* **2006**, 6(2), 375-402.
- De Haan, D. O.; Hawkins, L. N.; Kononenko, J. A.; Turley, J. J.; Corrigan, A. L.; Tolbert, M. A.; Jimenez, J. L. Formation of nitrogen-containing oligomers by methylglyoxal and amines in simulated evaporating cloud droplets. *Environ. Sci. Technol.* **2011**, 45 (3), 984991.
- Dick, W. D.; Saxena, P.; McMurry, P. H. Estimation of water uptake by organic compounds in submicron aerosols measured during the Southeastern Aerosol and Visibility Study. *J. Geophys. Res. Atmos.* **2000**, 105(D1), 1471-1479.
- Doherty, S. J.; Warren, S. G.; Grenfell, T. C.; Clarke, A. D.; Brandt, R. E. Light-absorbing impurities in Arctic snow. *Atmos. Chem. Phys.* **2010**, 10(23), 11647-11680.
- Drozd, G. T.; McNeill, V. F. Organic matrix effects on the formation of light-absorbing compounds from α -dicarbonyls in aqueous salt solution. *Environmental Science: Processes & Impacts.* 2014, 16(4), 741-477.
- Eastern, R. C.; Peter, L. K. Binary homogeneous nucleation: temperature and relative humidity fluctuations, nonlinearity, and aspects of new particles production in the atmosphere. *J. Appl. Meteorol.* **1994**, 33, 775-784.
- Erdakos, G. B.; Asher, W. E.; Seinfeld, J. H.; Pankow, J. F. Prediction of Activity Coefficients in Liquid Aerosol Particles Containing Organic Compounds, Dissolved Inorganic Salts, and Water—Part 1: Organic Compounds and Water by Consideration of Short-and Long-range Effects Using X-UNIFAC. 1. *Atmos. Environ.* **2006**, 40, 6410-4621.
- Escoreia, E. N.; Sjostedt, S. J.; Abbatt, J. P. D. Kinetics of N₂O₅ hydrolysis on secondary organic aerosol and mixed ammonium bisulfate-secondary organic aerosol particles. *J. Phys. Chem. A.* **2010**, 114, 13113–13121.
- Faraday Discuss.* **2013**, 165, 336–338, DOI: 10.1039/C3FD90033A.

- Feng, Y.; Ramanathan, V.; Kotamarthi, V. R. Brown carbon: a significant atmospheric absorber of solar radiation? *Atmos. Chem. Phys.* **2013**, 13(17), 8607-8621.
- Finlayson-Pitts, B. J.; Pitts, J. N. Tropospheric Air Pollution: Ozone, Airborne Toxics, Polycyclic Aromatic Hydrocarbons, and Particles. *Science*. **1997**, 276, 1045-1051.
- Folkers, M.; Mentel, T. F.; Wahner, A. Influence of an organic coating on the reactivity of aqueous aerosols probed by the heterogeneous hydrolysis of N_2O_5 . *Geophys. Res. Lett.* **2003**, 30, 1644.
- Forster, P.; Ramaswamy, V.; Artaxo, P.; Berntsen, T.; Betts, R.; Fahey, D. W.; Haywood, J.; Lean, J.; Lowe, D. C.; Myhre, G.; Nganga, J. Changes in Atmospheric Constituents and in Radiative forcing. Chapter 2. In *Climate Change 2007. The Physical Science Basis* 2007.
- Graber, E. R.; Rudich, Y. Atmospheric HULIS: How humic-like are they? A comprehensive and critical review. *Atmos. Chem. Phys.* **2006**, 729-753.
- Graham, B.; Mayol-Bracero, O. L.; Guyon, P.; Roberts, G. C.; Decesari, S.; Facchini, M. C.; Artaxo, P.; Maenhaut, W.; Köll, P.; Andreae, M. O. Water-soluble organic compounds in biomass burning aerosols over Amazonia 1. Characterization by NMR and GC-MS. *J. Geophys. Res. Atmos.* **2002**, 107(D20).
- Gaston, C. J.; Thornton, J. A.; Ng, N. L. Reactive uptake of N_2O_5 to internally mixed inorganic and organic particles: the role of organic carbon oxidation state and inferred organic phase separations. *Atmos. Chem. Phys.* **2014**, 14(11), 5693-5707.
- Gaston, C. J.; Thornton, J. A. Reacto-Diffusive Length of N_2O_5 in Aqueous Sulfate- and Chloride-Containing Aerosol Particles. *J. Phys. Chem. A*. **2016**, 120(7), 1039-1045.
- Goldstein, A. H.; Galbally, I. E. Known and unexplored organic constituents in the earth's atmosphere. *Environ. Sci. Technol.* **2007**, 1514-1521.
- Hänel, G. The Properties of Atmospheric Aerosol Particles as Functions of the Relative Humidity at Thermodynamic Equilibrium with the Surrounding Moist Air. *Advances in geophysics*. **1976**, 19, 73-188.
- Hansen, J.; Sato, M.; Ruedy, R. J. Radiative forcing and climate response. *Geophys. Res. Atmos.* **1997**, 102, 6831-6864.
- Harrison, R. M.; Yin, J. Particulate matter in the atmosphere: which particle properties are important for its effects on health? *Sci. Total. Environ.* **2000**, 249(1), 85-101.
- Haywood, J.; Boucher, O. Estimates of the direct and indirect radiative forcing due to tropospheric aerosols: A review. *Rev. Geophys.* **2000**, 38.4, 513-543.
- Hecobian, A.; Zhang, X.; Zheng, M.; Frank, N.; Edgerton, E. S.; Weber, R. Water-Soluble Organic Aerosol material and the light-absorption characteristics of aqueous extracts measured over the Southeastern United States. *J. Atmos. Chem. Phys.* **2010**, 10(13), 5965-5977.
- Hodas, N.; Zuend, A.; Mui, W.; Flagan, R. C.; Seinfeld, J. H. Influence of particle-phase state on the hygroscopic behavior of mixed organic-inorganic aerosols. *Atmos. Chem. Phys.* **2015**, 15(9), 5027-5045.
- Jaques, P. A.; Kim, C. S. Measurement of total lung deposition of inhaled ultrafine particles in healthy men and women. *Inhal. Toxicol.* **2000**, 12(8), 715-731.

- Jethva, H.; Torres, O. Satellite-based evidence of wavelength-dependent aerosol absorption in biomass burning smoke inferred from Ozone Monitoring Instrument. *Atmos. Chem. Phys.* **2011**, 11(20), 10541.
- Jiang, X.; Wiedinmyer, C.; Carlton, A. G. Aerosols from fires: An examination of the effects on ozone photochemistry in the Western United States. *Environ. Sci. Technol.* **2012**, 46(21), 11878-11886.
- Jimenez, J. L.; Canagaratna, M. R.; Donahue, N. M.; Prevot, A. S. H.; Zhang, Q.; Kroll, J. H.; ... & Shimojo, A. Evolution of organic aerosols in the atmosphere. *Science*, **2009**, 326(5959), 1525-1529.
- Kaiser T, Schweiger G. Stable algorithm for the computation of Mie coefficients for scattered and transmitted fields of a coated sphere. *Computers in Physics*. 1993 Nov 1;7(6):682-6.
- Kaiser T, Schweiger G. Stable algorithm for the computation of Mie coefficients for scattered and transmitted fields of a coated sphere. *Computers in Physics*. 1993 Nov 1;7(6):682-6.
- Kanakidou, M.; Seinfeld, J. H.; Pandis, S. N.; Barnes, I.; Dentener, F. J.; Facchini, M. C., ... & Wilson, J. Organic aerosol and global climate modeling: a review. *Atmos. Chem. Phys.* **2005**, 5(4), 1053-1123.
- Kidd, C.; Perraud, V.; Wingen, L. M.; Finlayson-Pitts, B. J. Integrating Phase and Composition of Secondary Organic Aerosol from the Ozonolysis of α -pinene. *Proc. Natl. Acad. Sci. U.S.A.* **2014**, 111, 7552-7557.
- Kirchstetter, T. W.; Novakov, T.; Hobbs, P. V. Evidence that the spectral dependence of light absorption by aerosols is affected by organic carbon. *J. Geophys. Res.:Atmos.* **2004**, 109, D21(208).
- Kirchstetter, T. W.; Thatcher, T. L. Contribution of organic carbon to wood smoke particulate matter absorption of solar radiation. *Atmos. Chem. Phys.* **2012**, 12(14), 6067-6072.
- Knopf, D. A. Thermodynamic Properties and Nucleation Processes of Upper Tropospheric and Lower Stratospheric Aerosol Particles, Diss. ETH No. 15103, Zurich, Switzerland, **2003**.
- Koop, T.; Bookhold, J.; Shiraiwa, M.; Pöschl, U. Glass Transition and Phase State of Organic Compounds: Dependency on Molecular Properties and Implications for Secondary Organic Aerosols in the Atmosphere. *Phys. Chem. Chem. Phys.* **2011**, 13, 19238-19255.
- Krom, M. D.; Berner, R. A. The Diffusion Coefficients of Sulfate, Ammonium, and Phosphate Ions in Anoxic Marine Sediments. *Limnol. Oceanogr.* **1980**, 25, 327-337.
- Krieger, U. K.; Marcolli, C.; Reid, J. P. Exploring the complexity of aerosol particle properties and processes using single particle techniques. *Chem. Soc. Rev.* **2012**, 41, 6631-6662.
- Kwamena, N. O. A.; Buajarnern, J.; Reid, J. P. Equilibrium Morphology of Mixed Organic/inorganic/aqueous Aerosol Droplets: Investigating the Effect of Relative Humidity and Surfactants. *J. Phys. Chem. A.* **2010**, 114, 5787-5795, DOI:10.1021/Jp1003648.
- Lack, D. A.; Cappa, C. D. Impact of brown and clear carbon on light absorption enhancement, single scatter albedo and absorption wavelength dependence of black carbon. *Atmos. Chem. Phys.* **2010**, 10(9), 4207-4220.

- Lack, D. A.; Langridge, J. M. On the attribution of black and brown carbon light absorption using the Ångström exponent. *Atmos. Chem. Phys.* **2013**, 13(20), 10535-10543.
- Lack, D. A.; Langridge, J. M.; Bahreini, R.; Cappa, C. D.; Middlebrook, A. M.; Schwarz, J. P. Brown carbon and internal mixing in biomass burning particles. *Proc. Natl. Acad. Sci. U.S.A.* **2012**, 109(37), 14802-14807.
- Lack, D. A.; Richardson, M. S.; Law, D.; Langridge, J. M.; Cappa, C. D.; McLaughlin, R. J.; Murphy, D. M. Aircraft instrument for comprehensive characterization of aerosol optical properties, part 2: black and brown carbon absorption and absorption enhancement measured with photo acoustic spectroscopy. *Aerosol. Sci. Technol.* **2012**, 46(5), 555-568.
- Langridge, J. M.; Richardson, M. S.; Lack, D. A.; Brock, C. A.; Murphy, D. M. Limitations of the photoacoustic technique for aerosol absorption measurement at high relative humidity. *Aerosol. Sci. Technol.* **2013**, 47(11), 1163-1173.
- Lang-Yona, N.; Abo-Riziq, A.; Erlick, C.; Segre, E.; Trainic, M.; Rudich, Y. Interaction of internally mixed aerosols with light. *Phys. Chem. Chem. Phys.* **2010**, 12(1), 21-31.
- Laskin, A.; Laskin, J.; Nizkorodov, S. A. Chemistry of Atmospheric Brown Carbon. *Chem. Rev.* **2015**, 115, 4335-4382.
- Leaist, D. G.; Hao, L. Binary Mutual Diffusion Coefficients of Aqueous Ammonium and Potassium Sulfates at 25° C. *J. Solution Chem.* **1992**, 21, 345-350.
- Lee, A. K.; Zhao, R.; Li, R.; Liggio, J.; Li, S. M.; Abbatt, J. P. Formation of light absorbing organo-nitrogen species from evaporation of droplets containing glyoxal and ammonium sulfate. *Environ. Sci. Technol.* **2013**, 47 (22), 12819-12826.
- Lee, S. H.; Murphy, D. M.; Thomson, D. S.; Middlebrook, A. M. Chemical Components of Single Particles Measured with Particle Analysis by Laser Mass Spectrometry (PALMS) During the Atlanta SuperSite Project: Focus on Organic/sulfate, Lead, Soot, and Mineral Particles. *J. Geophys. Res.* **2002**, 107(D1), 4003, DOI:10.1029/2000jd000011.
- Lee, S. H.; Murphy, D. M.; Thomson, D. S.; Middlebrook, A. M. Nitrate and oxidized organic ions in single particle mass spectra during the 1999 Atlanta Supersite Project. *J. Geophys. Res.* **2003**, 108(D7), SOS-5.
- Li, G.; Bei, N.; Tie, X.; Molina, L. T. Aerosol effects on the photochemistry in Mexico City during MCMA-2006/MILAGRO campaign. *Atmos. Chem. Phys.* **2011**, 11(11), 5169.
- Li, G. Q.; Lai, P. T.; Huang, M. Q.; Zeng, S. H.; Li, B.; Cheng, Y. C. A Humidity-sensing Model for Metal-insulator-semiconductor Capacitors with Porous Ceramic Film. *J. Appl. Phys.* **2000**, 87, 8716-8720.
- Lienhard, D. M.; Huisman, A. J.; Bones, D. L.; Te, Y. F.; Luo, B. P.; Krieger, U. K.; Reid, J. P. Retrieving the Translational Diffusion Coefficient of Water from Experiments on Single Levitated Aerosol Droplets. *Phys. Chem. Chem. Phys.* **2014**, 16, 16677-16683, DOI:10.1039/c4cp01939c.
- Lienhard, D. M.; Huisman, A. J.; Krieger, U. K.; Rudich, Y.; Marcolli, C.; Luo, B. P.; Bones, D. L.; Reid, J. P.; Lambe, A. T.; Canagaratna, M. R.; Davidovits, P.; Onasch, T. B.; Worsnop, D. R.; Steimer, S. S.; Koop, T.; Peter, T. Viscous Organic Aerosol Particles in the Upper Troposphere: Diffusivity-controlled Water Uptake and Ice Nucleation. *Atmos. Chem. Phys.* **2015**, 15, 13599-13613, DOI:10.5194/acp-15-13599.

- Liu, J.; Bergin, M.; Guo, H.; King, L.; Kotra, N.; Edgerton, E.; Weber, R. J. Size-resolved measurements of brown carbon in water and methanol extracts and estimates of their contribution to ambient fine-particle light absorption. *J. Atmos. Chem. Phys.* **2013**, 13(24), 12389-12404.
- Lohmann, U.; Feichter, J. Global indirect aerosol effects: a review. *Atmos. Chem. Phys.* **2005**, 5(3), 715-737.
- Löndahl, J.; Pagels, J.; Boman, C.; Swietlicki, E.; Massling, A.; Rissler, J.; ... & Sandström, T. Deposition of biomass combustion aerosol particles in the human respiratory tract. *Inhal. Toxicol.* **2008**, 20(10), 923-933.
- Lu, J. W.; Rickards, A. M.; Walker, J. S.; Knox, K. J.; Miles, R. E.; Reid, J. P.; Signorell, R. Timescales of Water Transport in Viscous Aerosol: Measurements on Sub-micron Particles and Dependence on Conditioning History. *Phys. Chem. Chem. Phys.* **2014**, 16, 9819-9830.
- Ma, L.; Thompson, J. E. Optical properties of dispersed aerosols in the near ultraviolet (355 nm): measurement approach and initial data. *Anal. Chem.* **2012**, 84(13), 5611-5617.
- Ma, X.; Yu, F.; Luo, G. Aerosol direct radiative forcing based on GEOS-Chem-APM and uncertainties. *Atmos. Chem. Phys.* **2012**, 12(12), 5563-5581.
- Mackowski, D. W.; Mishchenko, M. I. Calculation of the T matrix and the scattering matrix for ensembles of spheres. *JOSA A.* **1996**, 13(11), 2266-2278.
- Marchand, G.; Lavoie, J.; Lazure, L. Evaluation of bioaerosols in a municipal solid waste recycling and composting plant. *J. Air. Waste. Manag. Assoc.* **1995**, 45(10), 778-781.
- Marculli, C.; Luo, B. P.; Peter, T. Mixing of the Organic Aerosol Fractions: Liquids as the Thermodynamically Stable Phases. *J. Phys. Chem. A.* **2004**, 108, 2216-2224, DOI:10.1021/Jp036080l.
- Marculli, C.; Krieger, U. K. Phase Changes During Hygroscopic Cycles of Mixed Organic/inorganic Model Systems of Tropospheric Aerosols. *J. Phys. Chem. A.* **2006**, 110, 1881-1893, DOI:10.1021/Jp0556759.
- Marcus, Y. Ionic Radii in Aqueous Solutions. *Chem. Rev.* **1988**, 88, 1475-1498.
- Marshall, F. H.; Miles, R. E. H.; Song, Y. C.; Ohm, P. B.; Power, R. M.; Reid, J. P.; Dutcher, C. S. Diffusion and Reactivity in Ultra-viscous Aerosol and the Correlation with Particle Viscosity. *Chem. Sci.* **2016**, 7, 1298-1308, DOI:10.1039/c5sc03223g.
- Martin, S. T. Phase Transitions of Aqueous Atmospheric Particles. *Chem. Rev.* **2000**, 100, 3403-3453, DOI:10.1021/Cr990034t.
- Martin, S.T.; Hung, H. M.; Park, R. J.; Jacob, D. J.; Spurr, R. J.; Chance, K. V.; Chin, M. Effects of The Physical State of Tropospheric Ammonium-sulfate-nitrate Particles on Global Aerosol Direct Radiative Forcing. *Atmos. Chem. Phys.* **2004**, 4, 183-214.
- Mayol-Bracero, O. L.; Guyon, P.; Graham, B.; Roberts, G.; Andreae, M.O.; Decesari, S.; Facchini, M. C.; Fuzzi, S.; Artaxo, P. Water-soluble organic compounds in biomass burning aerosols over amazonia 2. Apportionment of the chemical composition and importance of the polyacidic fraction. *J. Geophys. Res. Atmos.* **2002**, 107(D20).

- McGuire, K.S.; Laxminarayan, A.; Martula, D. S.; Lloyd, D. R. Kinetics of Droplet Growth in Liquid–liquid Phase Separation of Polymer–diluent Systems: Model Development. *Adv. Colloid Interface Sci.* **1996**, 182, 46-58.
- McNeill, V.F.; Patterson, J.; Wolfe, G. M.; Thornton, J. A. The effect of varying levels of surfactant on the reactive uptake of N₂O₅ to aqueous aerosol. *Atmos. Chem. Phys.* **2006**, 6(6), 1635-1644.
- Middlebrook, A. M.; Murphy, D. M.; Thomson, D. S. Observations of organic material in individual marine particles at Cape Grim during the First Aerosol Characterization Experiment (ACE 1). *J. Geophys. Res: Atmos.* 1998, 103(D13), 16475-16483.
- Mie, G. Beiträge zur Optik trüber Medien, speziell kolloidaler Metallösungen. *Annalen der physik.* **1908**, 330(3), 377-445.
- Moise, T.; Flores, J. M.; Rudich, Y. Optical properties of secondary organic aerosols and their changes by chemical processes. *Chem. Rev.* **2015**, 115(10), 4400-4439.
- Moosmueller, H.; Chakrabarty, R. K.; Arnott, W. P. Aerosol light absorption and its measurement: A review. *J. Quant. Spectr. Rad. Transfer.* **2009**, 110(11), 844-878.
- Moosmueller, H.; Chakrabarty, R. K.; Ehlers, K. M.; Arnott, W. P. Absorption Ångström coefficient, brown carbon, and aerosols: basic concepts, bulk matter, and spherical particles. *Atmos. Chem. Phys.* **2011**, 11(3), 1217-1225.
- MSTM, Version 3.0: <http://eng.auburn.edu/users/dmckwski/scatcodes/>
- Murphy, D. M.; Cziczo, D. J.; Froyd, K. D.; Hudson, P. K.; Matthew, B. M.; Middlebrook, A. M.; Peltier, R. E.; Sullivan, A.; Thomson, D. S.; Weber, R. J. Single-Particle Mass Spectrometry of Tropospheric Aerosol Particles. *J. Geophys. Res.* **2006**, 111(D23), DOI:10.1029/2006jd007340.
- Murphy, D. M.; Thomson, D. S. Chemical composition of single aerosol particles at Idaho Hill: Negative ion measurements. *J. Geophys. Res.* **1997**, 102(D5), 6353-6368
- Murphy, D. M.; Thomson, D. S.; Mahoney, M. J. In situ measurements of organics, meteoritic material, mercury, and other elements in aerosols at 5 to 19 kilometers. *Science*, **1998**, 282(5394), 1664-1669.
- Nakajima, T.; Yoon, S. C.; Ramanathan, V.; Shi, G. Y.; Takemura, T.; Higurashi, A.; Takamura, T.; Aoki, K.; Sohn, B. J.; Kim, S. W.; Tsuruta, H. Overview of the Atmospheric Brown Cloud East Asian Regional Experiment 2005 and a study of the aerosol direct radiative forcing in east Asia. *J. Geophys. Res.: Atmos.* **2007**, 112, D22S21.
- Nakayama, T.; Matsumi, Y.; Sato, K.; Imamura, T.; Yamazaki, A.; Uchiyama, A. Laboratory studies on optical properties of secondary organic aerosols generated during the photooxidation of toluene and the ozonolysis of α -pinene. *J. Geophys. Res: Atmos.* **2010**, 115(D24).
- Nel, A. Air pollution-related illness: effects of particles. *Science*, **2005**, 308(5723), 804-806.
- Nel, A.; Xia, T.; Mädler, L.; Li, N. Toxic potential of materials at the nanolevel. *Science*, **2006**, 311(5761), 622-627.
- Nguyen, T. B.; Lee, P. B. Updyke, K. M.; Bones, D. L.; Laskin, J.; Laskin, A. Nizkorodov, S. A. Formation of nitrogen-and sulfur-containing light-absorbing compounds accelerated by evaporation of water from secondary organic aerosols. *J. Geophys. Res. Atmos.* **2012**, 117(D1), 207.

- O'Dowd, C. D.; Facchini, M. C.; Cavalli, F.; Ceburnis, D.; Mircea, M.; Decesari, S.; ... & Putaud, J.P. Biogenically driven organic contribution to marine aerosol. *Nature*, **2004**, 431(7009), 676-680.
- Pajunoja, A.; Malila, J.; Hao, L.; Joutsensaari, J.; Lehtinen, K. E.; Virtanen, A. Estimating the Viscosity Range of SOA Particles Based on Their Coalescence Time. *Aerosol. Sci. Technol.* **2014**, 48, i-iv.
- Pajunoja, A.; Lambe, A. T.; Hakala, J.; Rastak, N.; Cummings, M. J.; Brogan, J. F.; Hao, L.; Paramonov, M.; Hong, J.; Prisle, N. L.; Malila, J. Adsorptive Uptake of Water by Semisolid Secondary Organic Aerosols. *Geophys. Res. Lett.* **2015**, 42, 3063-3068.
- Pankow, J. F. Gas/particle Partitioning of Neutral and Ionizing Compounds to Single and Multi-phase Aerosol Particles. 1. Unified Modeling Framework. *Atmos. Environ.* **2003**, 37, 3323-3333, doi:10.1016/S1352-2310(03)00346-7.
- Pankow, J. F.; Chang, E. I. Variation in the sensitivity of predicted levels of atmospheric organic particulate matter (OPM). *Environ. Sci. Technol.* **2008**, 42(19), 7321-7329.
- Papon, P.; Leblond, J.; Meijer, P. H. E. *The Physics of Phase Transitions: Concepts and Applications*, Springer, New York, US. 1999.
- Parsons, M. T.; Mak, J.; Lipetz, S. R.; Bertram, A. K. Deliquescence of Malonic, Succinic, Glutaric, and Adipic Acid Particles. *J. Geophys. Res. Atmos.* **2004**, 109, 109, D06212, 8 pages, doi:10.1029/2003jd004075.
- Perraud, V.; Bruns, E. A.; Ezell, M. J.; Johnson, S. N.; Yu, Y.; Alexander, M. L.; Zelenyuk, A.; Imre, D.; Chang, W. L.; Dabdub, D.; Pankow, J. F. Non-equilibrium Atmospheric Secondary Organic Aerosol Formation and Growth. *Proc. Natl. Acad. Sci. U.S.A.* **2012**, 109, 2836-2841.
- Pilinis, C.; Seinfeld, J. H.; Grosjean, D. Water content of atmospheric aerosols. *Atmos. Environ.* **1989**, 23(7), 1601-1606.
- Pope III, C. A.; Dockery, D. W. Health Effects of Fine Particulate Air Pollution: Lines that Connect. *J. Air Waste Manage. Assoc.* **2006**, 56, 709-742.
- Pöschl, U. Atmospheric aerosols: Composition, transformation, climate and health effects. *Angew. Chem. Int. Ed.* **2005**, 44(46), 7520-7540.
- Powelson, M. H.; Espelien, B. M.; Hawkins, L. N.; Galloway, M. M.; De Haan, D. O. Brown carbon formation by aqueous-phase carbonyl compound reactions with amines and ammonium sulfate. *Environ. Sci. Technol.* **2014**, 48(2), 985-993.
- Prisle, N. L.; Raatikainen, T.; Laaksonen, A.; Bilde, M. Surfactants in Cloud Droplet Activation: Mixed Organic-inorganic particles. *Atmos. Chem. Phys.* **2010**, 10, 5663-5683.
- Qiu, Y.; Molinero, V. Morphology of liquid-liquid phase separated aerosols. *J. Amer. Chem. Soc.* **2015**, 137(33), 10642-10651.
- Ramanathan, V.; Crutzen, P. J.; Lelieveld, J.; Mitra, A. P.; Althausen, D.; Anderson, J.; Andreae, M. O.; Cantrell, W.; Cass, G. R.; Chung, C. E.; Clarke, A. D. Indian Ocean Experiment: An integrated analysis of the climate forcing and effects of the great Indo - Asian haze. *J. Geophys. Res. Atmos.* **2001**, 106(D22), 28371-28398.
- Ramanathan, V.; Li, F.; Ramana, M. V.; Praveen, P. S.; Kim, D.; Corrigan, C. E.; Nguyen, H.; Stone, E. A.; Schauer, J. J.; Carmichael, G. R.; Adhikary, B. Atmospheric brown clouds: Hemispherical and regional variations in long-range

- transport, absorption, and radiative forcing. *J. Geophys. Res: Atmos.* **2007**, 112(D22).
- Ravishankara, A. R. Heterogeneous and Multiphase Chemistry in the Troposphere. *Science.* **1997**, 276, 1058-1065.
- Renbaum-Wolff, L.; Grayson, A.; Bateman, A. P.; Kuwata, M.; Sellier, M.; Murray, B. J.; Shilling, J. E.; Martin, S. T.; Bertram, A. K. Viscosity of α -Pinene Secondary Organic Material and Implications for Particle Growth and Reactivity. *Proc. Natl. Acad. Sci. U.S.A.* **2013**, 110, 8014–8019.
- Reid, J. P.; Dennis-Smith, B. J.; Kwamena, N. O. A.; Miles, R. E. H.; Hanford, K. L.; Homer, C. J. The Morphology of Aerosol Particles Consisting of Hydrophobic and Hydrophilic Phases: Hydrocarbons, Alcohols and Fatty Acids as the Hydrophobic Component, *Phys. Chem. Chem. Phys.* **2011**, 13, 15559–15572, DOI:10.1039/C1CP21510H.
- Reid, J. P.; Mitchem, L. Laser probing of single-aerosol droplet dynamics. *Annu. Rev. Phys. Chem.* **2006**, 57, 245-271.
- Reisen, F.; Meyer, C. P.; McCaw, L.; Powell, J. C.; Tolhurst, K.; Keywood, M. D.; & Gras, J. L. Impact of smoke from biomass burning on air quality in rural communities in southern Australia. *Atmospheric Environment.* **2011**, 45(24), 3944-3953.
- Richardson, C. B.; Spann, J. F. Measurement of the water cycle in a levitated ammonium sulfate particle. *J. Aerosol. Sci.* **1984**, 15(5), 563-71.
- Riemer, N.; Vogel, H.; Vogel, B.; Anttila, T.; Kiendler-Scharr, A.; Mentel, T. F. Relative importance of organic coatings for the heterogeneous hydrolysis of N_2O during summer in Europe. *J. Geophys. Res. Atmos.* **2009**, 114(D17), 307.
- Rothfuss, N. E.; Petters, M. D. Characterization of the Temperature and Humidity-dependent Phase Diagram of Amorphous Nanoscale Organic Aerosols. *Phys. Chem. Chem. Phys.* **2017**;19(9):6532-6545.
- Saleh, R.; Hennigan, C. J.; McMeeking, G. R.; Chuang, W. K.; Robinson, E. S.; Coe, H.; Donahue, N. M.; Robinson, A. L. Absorptivity of brown carbon in fresh and photo-chemically aged biomass-burning emissions. *Atmos. Chem. Phys.* **2013**, 15, 7683-7693.
- Saleh, R.; Robinson, E. S.; Tkacik, D. S.; Ahern, A. T.; Liu, S.; Aiken, A. C.; Sullivan, R. C.; Presto, A. A.; Dubey, M. K.; Yokelson, R. J.; Donahue, N. M. Brownness of organics in aerosols from biomass burning linked to their black carbon content. *Nat. Geosci.* **2014**, 7(9), 647-650.
- Salma, I.; Ocskay, R.; Láng, G. G. Properties of atmospheric humic-like substances–water system. *Atmos. Chem. Phys.* **2008**, 8(8), 2243-2254.
- Sarangapani, R. Modeling particle deposition in extrathoracic airways. *Aerosol. Sci. Technol.* **2000**, 32(1), 72-89.
- Sarangapani, R.; Wexler, A. S. The role of dispersion in particle deposition in human airways. *Toxicol. Sci.* **2000**, 54(1), 229-236.
- Sareen, N.; Moussa, S. G.; McNeill, V. F. Photochemical Aging of Light-Absorbing Secondary Organic Aerosol Material. *J. Phys. Chem. A.* **2013**, 117, 2987–2996.
- Satheesh, S. K.; Moorthy, K. K. Radiative effects of natural aerosols: A review. *Atmos. Environ.* **2005**, 39(11), 2089-2110.

- Saxena, P.; Hildemann, L. M. Water-soluble organics in atmospheric particles: A critical review of the literature and application of thermodynamics to identify candidate compounds. *J. Atmos. Chem.* **1996**, 24(1), 57-109.
- Schill, G. P.; Tolbert, M. A. Heterogeneous ice nucleation on phase-separated organicsulfate particles: effect of liquid vs. glassy coatings, *Atmos. Chem. Phys.* **2013**, 13, 4681-4695.
- Schneider, C. A.; Rasband, W. S.; Eliceiri, K. W. NIH Image to ImageJ: 25 Years of Image Analysis. *Nature methods.* **2012**, 9(7), 671-675.
- Schroeter, J. D.; Musante, C. J.; Hwang, D.; Burton, R.; Guilmette, R.; Martonen, T. B. Hygroscopic growth and deposition of inhaled secondary cigarette smoke in human nasal pathways. *Aerosol. Sci. Technol.* **2001**, 34, 137-143.
- Seinfeld, J. H.; Erdakos, G. B.; Asher, W. E.; Pankow, J. F. Modeling the formation of secondary organic aerosol (SOA). 2. The predicted effects of relative humidity on aerosol formation in the α -pinene-, β -pinene-, sabinene-, Δ^3 -Carene-, and cyclohexene-ozone systems. *Environ. Sci. Technol.* **2001**, 35, 1806-1817.
- Seinfeld, J. H.; Pandis, S. N. *Atmospheric Chemistry and Physics: From Air Pollution to Climate Change*, John Wiley and Sons Inc. U.S.A., 1998.
- Seinfeld, J. H.; Pandis, S. N. *Atmospheric chemistry and physics*, Wiley Interscience: Hoboken, New Jersey, U.S.A., 2006.
- Shiraiwa, M., Zuend, A., Bertram, A. K., and Seinfeld, J. H.: Gas-particle partitioning of atmospheric aerosols: interplay of physical state, non-ideal mixing and morphology. *Phys. Chem. Chem. Phys.* **2013**, 15, 11441-11453.
- Smith, R. S.; Kay, B. D. The Existence of Supercooled Liquid Water at 150 K. *Nature.* **1999**, 398, 788-791.
- Smith, M. L.; Kuwata, M.; Martin, S. T. Secondary Organic Material Produced by the Dark Ozonolysis of Alpha-pinene Minimally Affects the Deliquescence and Efflorescence of Ammonium Sulfate. *Aerosol Sci. Tech.* **2011**, 45, 244-261, DOI: 10.1080/02786826.2010.532178.
- Smith, M. L.; Bertram, A. K.; Martin, S. T. Deliquescence, Efflorescence, and Phase Miscibility of Mixed Particles of Ammonium Sulfate and Isoprene-derived Secondary Organic Material. *Atmos. Chem. Phys.* **2012**, 12, 9613-9628.
- Solomon, S.; Qin, D.; Manning, M.; Chen, Z.; Marquis, M.; Averyt, K. B.; Tignor, M.; Miller, H. L. *Climate Change 2007: The physical science basis. Contribution of Working Group I to the Fourth Assessment Report of the Intergovernmental Panel on Climate Change*, Cambridge University Press, Cambridge, United Kingdom and New York, NY, U.S.A., 2007.
- Song, M.; Marcolli, C.; Krieger, U. K.; Zuend, A.; Peter, T. Liquid-liquid phase separation in aerosol particles: Dependence on O:C, organic functionalities, and compositional complexity. *Geophys. Res. Lett.* **2012**, 39, L19801.
- Song, M.; Marcolli, C.; Krieger, U. K.; Zuend, A.; Peter, T. Liquid-liquid Phase Separation and Morphology of Internally Mixed Dicarboxylic Acids/Ammonium Sulfate/Water Particles. *Atmos. Chem. Phys.* **2012**, 12, 2691-2712.
- Song, M.; Marcolli, C.; Krieger, U. K.; Lienhard, D. M.; Peter, T. Morphologies of Mixed Organic/Inorganic/Aqueous Aerosol Droplets. *Faraday discuss.* **2013**, 165, 289-316.
- Song, Y. C.; Haddrell, A. E.; Bzdek, B. R.; Reid, J. P.; Bannan, T.; Topping, D. O.; Percival, C.; Cai, C. Measurements and Predictions of Binary Component Aerosol

- Particle Viscosity. *J. Phys. Chem. A.* **2016**, 120, 8123–8137, DOI:10.1021/acs.jpca.6b07835.
- Steimer, S. S.; Berkemeier, T.; Gilgen, A.; Krieger, U. K.; Peter, T.; Shiraiwa, M.; Ammann, M. Shikimic Acid Ozonolysis Kinetics of the Transition from Liquid Aqueous Solution to Highly Viscous Glass. *Phys. Chem. Chem. Phys.* **2015**, 17, 31101–31109, DOI: 10.1039/C5CP04544D.
- Stocker, T, editor. Climate change 2013: the physical science basis: Working Group I contribution to the Fifth assessment report of the Intergovernmental Panel on Climate Change. Cambridge University Press. **2014**.
- Tanaka, K. Measurements of Tracer Diffusion Coefficients of Sulphate Ions in Aqueous Solutions of Ammonium Sulphate and Sodium Sulphate, and of Water in Aqueous Sodium Sulphate Solutions. *J. Chem. Soc., Faraday Trans. 1: Physical Chemistry in Condensed Phases.* **1988**, 84, 2895-2897.
- Tang, I. N. Phase transformation and growth of aerosol particles composed of mixed salts. *J. Aerosol. Sci.* **1976**, 7, 361–371.
- Tang, I. N.; Munkelwitz, H. R. Composition and temperature dependence of the deliquescence properties of hygroscopic aerosols. *Atmos. Environ.* **1993**, Part A, 27(4), 467–473.
- Tang, I. N.; Munkelwitz, H. R. Water activities, densities, and refractive indices of aqueous sulfates and sodium nitrate droplets of atmospheric importance. *J. Geophys. Res.* **1994**, 99(D9), 18801-18.
- Tang M, Alexander JM, Kwon D, Estillore AD, Laskina O, Young MA, Kleiber PD, Grassian VH. Optical and Physicochemical Properties of Brown Carbon Aerosol: Light Scattering, FTIR Extinction Spectroscopy, and Hygroscopic Growth. *The Journal of Physical Chemistry A.* **2016**, (24), 4155-4166.
- Thornton, J. A.; Braban, C. F.; Abbatt, J. P. N₂O₅ hydrolysis on sub-micron organic aerosols: The effect of relative humidity, particle phase, and particle size. *Phys. Chem. Chem. Phys.* **2003**, 5(20), 4593-4603.
- Updyke, K. M.; Nguyen, T. B.; Nizkorodov, S. A. Formation of brown carbon via reactions of ammonia with secondary organic aerosols from biogenic and anthropogenic precursors. *Atmos. Environ.* **2012**, 63, 22-31.
- Van de Hulst, H. C. *Light Scattering by Small Molecules*. Dover Publications, Inc, New York, 1957.
- Veghte, D. P.; Altaf, M. B.; Freedman, M. A. Size Dependence of the Structure of Organic Aerosol. *J. Amer. Chem. Soc.* **2013**, 135, 16046-16049.
- Veghte, D. P.; Bittner, D. R.; Freedman, M. A. Cryo-transmission Electron Microscopy Imaging of the Morphology of Sub-micrometer Aerosol Containing Organic Acids and Ammonium Sulfate. *Anal. Chem.* **2014**, 86, 2436-2442.
- Veghte, D. P.; Freedman, M. A. The necessity of microscopy to characterize the optical properties of size-selected, nonspherical aerosol particles. *Anal. Chem.* **2012**, 84(21), 9101-9108.
- Wang, H. Formation of nascent soot and other condensed-phase materials in flames. *Proc. Combust. Inst.* **2011**, 33(1), 41-67.
- Wang, J.; Hoffmann, A. A.; Park, R. J.; Jacob, D. J.; Martin, S. T. Global distribution of solid and aqueous sulfate aerosols: Effect of the hysteresis of particle phase transitions. *J. Geophys. Res.* 2008, 113, D11206, 2008a.

- Wang, L.; Li, Z.; Tian, Q.; Ma, Y.; Zhang, F.; Zhang, Y.; Li, D.; Li, K.; Li, L. Estimate of aerosol absorbing components of black carbon, brown carbon, and dust from ground-based remote sensing data of sun-sky radiometers. *J. Geophys. Res.: Atmos.* **2013**, 118(12), 6534-6543
- Wang, X.; Heald, C. L.; Ridley, D. A.; Schwarz, J. P.; Spackman, J. R.; Perring, A. E.; Coe, H.; Liu, D.; Clarke, A. D. Exploiting simultaneous observational constraints on mass and absorption to estimate the global direct radiative forcing of black carbon and brown carbon. *Atmos. Chem. Phys.* **2014**, 14(20), 10989-11010.
- Weis, D. D.; Ewing, G. E. Water content and morphology of sodium chloride aerosol particles. *J. Geophys. Res.* **1999**, 104, 21275–21285.
- World Health Organization, Regional Office for Europe. *Air Quality Guidelines: Global Update 2005. Particulate Matter, Ozone, Nitrogen Dioxide and Sulphur Dioxide*. World Health Organization. 2006.
- Yang, M.; Howell, S. G.; Zhuang, J.; Huebert, B. J. Attribution of aerosol light absorption to black carbon, brown carbon, and dust in China—interpretations of atmospheric measurements during EAST-AIRE. *Atmos. Chem. Phys.* **2009**, 9(6), 2035-2050.
- Yatavelli, R. L.; Stark, H.; Thompson, S. L.; Kimmel, J. R.; Cubison, M. J.; Day, D. A.; Campuzano-Jost, P.; Palm, B. B.; Hodzic, A.; Thornton, J. A.; Jayne, J. T. Semi-continuous Measurements of Gas–particle Partitioning of Organic Acids in a Ponderosa Pine Forest Using a MOVI-HRTof-CIMS. *Atmos. Chem. Phys.* **2014**, 14, 1527-1546.
- You, Y.; Bertram, A. K. Effects of Molecular Weight and Temperature on Liquid–liquid Phase Separation in Particles Containing Organic Species and Inorganic Salts. *Atmos. Chem. Phys.* **2015**, 15, 1351-1365.
- You, Y.; Renbaum-Wolff, L.; Carreras-Sospedra, M.; Hanna, S. J.; Hiranuma, N.; Kamal, S.; Smith, M. L.; Zhang, X.; Weber, R. J.; Shilling, J. E.; et al. Images Reveal that Atmospheric Particles can Undergo Liquid–liquid Phase Separations. *Proc. Natl. Acad. Sci. U.S.A.* **2012**, 109, 13188-13193.
- You, Y.; Smith, M. L.; Song, M.; Martin, S. T.; Bertram, A. K. Liquid–liquid Phase Separation in Atmospherically Relevant Particles Consisting of Organic Species and Inorganic Salts. *Int. Rev. Phys. Chem.* **2014**, 33, 43-77.
- Yu, H.; Kaufman, Y. J.; Chin, M.; Feingold, G.; Remer, L. A.; Anderson, T. L.; Balkanski, Y.; Bellouin, N.; Boucher, O.; Christopher, S.; DeCola, P.; Kahn, R.; Koch, D.; Loeb, N.; Reddy, M. S.; Schulz, M.; Takemura, T.; Zhou, M. A review of measurement-based assessments of the aerosol direct radiative effect and forcing. *Atmos. Chem. Phys.* **2006**, 6(3), 613-666.
- Zardini, A. A.; Sjogren, S. Marcoll, C.; Krieger, U. K.; Gysel, M.; Weingartner, E.; Baltensperger, U.; Peter, T. A combined particle trap/HTDMA hygroscopicity study of mixed inorganic/organic aerosol particles. *Atmos. Chem. Phys.* **2008**, 8(18), 589-601.
- Zhang, S.; Bellouin, N.; Guttikunda, S. K.; Hopke, P. K.; Jacobson, M. Z.; Kaiser, J. W.; Klimont, Z.; Lohmann, U.; Schwarz, J. P.; Shindell, D.; Storelvmo, T.; Warren, S. G.; Zender, C. S. J. . *Bounding the role of black carbon in the climate system: A scientific assessment. Geophys. Res.: Atmos.* **2013**, 118(11), 5380-5520.
- Zhang Q, Jimenez JL, Canagaratna MR, Allan JD, Coe H, Ulbrich I, Alfarra MR, Takami A, Middlebrook AM, Sun YL, Dzepina K. Ubiquity and dominance of oxygenated species in organic aerosols in anthropogenically-influenced Northern Hemisphere midlatitudes. *Geophys. Res. Lett.* **2007**, 34(13).

- Zhang, X.; Lin, Y. H.; Surratt, J. D.; Zotter, P.; Prévôt, A. S. H.; Weber, R. J. Light-Absorbing Soluble Organic Aerosol in Los Angeles and Atlanta: A Contrast in Secondary Organic Aerosol. *Geophys. Res. Lett.* **2011**, 38, L21810.
- Zhang, X. Q.; McMurray, P.H.; Hering, S. V.; Casuccio, G. S. Mixing characteristics and water content of submicron aerosols measured in Los Angeles and at the Grand Canyon. *Atmospheric Environment. Part A. General Topics.* 1993 Jul 1;27(10):1593-607.
- Zhang, Y.; Sanchez, M. S.; Douet, C.; Wang, Y.; Bateman, A. P.; Gong, Z.; Kuwata, M.; Renbaum-Wolff, L.; Sato, B. B.; Liu, P. F.; Bertram, A. K. Changing Shapes and implied viscosities of suspended submicron particles. *Atmospheric Chemistry and Physics.* **2015**, 15(14), 7819-7829.
- Zhang, Y. H. P. What is vital (and not vital) to advance economically-competitive biofuels production. *Process. Biochem.* **2011**, 46(11), 2091-2110.
- Zhao, Y.; Gao, Y. Acidic species and chloride depletion in coarse aerosol particles in the US east coast. *Sci. Total. Environ.* **2008**, 407(1), 541-547.
- Zimmermann, R. Ambient aerosols and human health: working towards a combined analytical and toxicological approach. *Anal. Bioanal. Chem.* **2011**, 401(10), 3041-3044.
- Zobrist, B.; Soonsin, V.; Luo, B. P.; Krieger, U. K.; Marcolli, C.; Peter, T.; Koop, T. Ultra-slow water diffusion in aqueous sucrose glasses. *Phys. Chem. Chem. Phys.* **2011**, 13, 3514–3526, DOI: 10.1039/c0cp01273d, 2011.
- Zuend, A.; Marcolli, C.; Peter, T.; Seinfeld, J. H. Computation of Liquid-liquid Equilibria and Phase Stabilities: Implications for RH-dependent Gas/particle Partitioning of Organic-inorganic Aerosols. *Atmos. Chem. Phys.* **2010**, 10, 7795–7820, DOI: 10.5194/acp-10-7795-2010.
- Zuend, A.; Marcolli, C.; Booth, A. M.; Lienhard, D. M.; Soonsin, V.; Krieger, U. K.; Topping, D. O.; McFiggans, G.; Peter, T.; Seinfeld, J. H. New and Extended Parameterization of the Thermodynamic Model AIOMFAC: Calculation of Activity Coefficients for Organic-inorganic Mixtures Containing Carboxyl, Hydroxyl, Carbonyl, Ether, Ester, Alkenyl, Alkyl, and Aromatic Functional Groups. *Atmos. Chem. Phys.* **2011**, 11, 9155-206.
- Zuend, A.; Seinfeld, J. H. Modeling the Gas-particle Partitioning of Secondary Organic Aerosol: the Importance of Liquid-liquid Phase Separation. *Atmos. Chem. Phys.* **2012**, 12, 3857-3882.

Acknowledgements

I would like to express my deepest gratitude to Tom Peter for giving me the opportunity to work on this PhD project. Your scientific intuition, valuable insights, and your enthusiasm for truly understanding every single detail was extremely inspirational. Thank you for being a constant source of counsel, encouragement, guidance, and most of all unconditional support when times were rough.

I would also like to kindly thank my main supervisor, Uli Krieger for his scientific expertise, his immense knowledge of experimental physical chemistry, for coming up with new ideas almost everyday, for remaining optimistic in my project especially when I wasn't, for offering valuable feedback on my thesis and for his great passion for science.

I would like to extend my gratitude to the following people:

Thomas Mentel for accepting to review my work and his willingness to travel to Zurich to be part of my examination committee.

Beiping Luo, for his fruitful discussions and sharing his pearls of wisdom regarding diffusivity estimations.

Uwe Weers, for his technical support in the lab and always keeping a high spirit!

Petra Forney and Eva Choffat, for offering their administrative assistance.

Hans-Heini Vogel, for providing IT support, being a joyful soul, and caring for the plants!

All my friends and colleagues at IAC, Zurich, Copenhagen, Vancouver, Tehran and all around the globe for making me learn, laugh, live, think, and challenge me to be a better person.

And last but not least, a very special thank you to "Abraham", for everything!

Curriculum Vitae

Mehrnoush Mousavi-Fard

Date of birth: Sep 21, 1980 in Tehran, Iran

Education

Nov 2013 - May 2017 PhD studies in Atmospheric Sciences
Institute for Atmospheric and Climate Sciences (IAC)
Swiss Federal Institute of Technology Zurich
ETH Zurich, Switzerland

Thesis title: Morphology and Optical properties of Liquid-liquid
Phase Separated Particles.

Supervisors: Dr. Ulrich Krieger & Prof. Dr. Thomas Peter

Sep 2011- Sep 2013 Master's degree in Chemistry (MSc. in Chemistry)
University of Copenhagen, Denmark
Thesis title: Water Activity of pure & mixed Inorganic / Organic
Compounds of Atmospheric Relevance".
Supervisors: Prof. Dr. Merete Bilde & Prof. Dr. Ole John Neilson

Sep 2004 – June 2009 Bachelor of Science (BSc) in Chemistry
Simon Fraser University, Vancouver, Canada

Publications

Published:

1. Fard, M. M.; Krieger, K. U.; Peter, Thomas. Kinetic Limitation to Inorganic Ion Diffusivity and to Coalescence of Inorganic Inclusions in Viscous Liquid-Liquid Phase-Separated Particles. *J. Phys. Chem. A*. **2017**, 121 (48), 9284-9296.

2. Zieger, P.; Väisänen, O.; Corbin, J. C.; Partridge, D. G.; Bastelberger, S., Mousavi-Fard, M., ... & Nenes, A. Revising the hygroscopicity of inorganic sea salt particles. *Nature Communications*. **2017**, 8, ncomms15883.

3. Elm, J., Fard, M., Bilde, M., Mikkelsen, K. V. Interaction of glycine with common atmospheric nucleation precursors. *J. Phys. Chem. A*. **2013**, 117(48), 12990-7.

In Preparation

(Fard et al., **2018**) Radiative impact of liquid-liquid phase separation for aerosol containing a molecular absorber such as “Brown Carbon”.

International Conferences and Summer school

- 2012 Summer school on organic aerosols, Hyytiälä , Finland (poster presentation)
- 2012 European Aerosol Conference (EAC), Granada, Spain
- 2012 The Nordic Society for Aerosol Research Symposium (NOSA)
Helsingør, Denmark (oral presentation)
- 2013 European Aerosol Conference (EAC),
Prague, Czech Republic (poster presentation)
- 2014 European Geosciences Union (EGU), Vienna, Austria, (poster presentation)
- 2014 Towards a Molecular-level Understanding of Atmospheric Aerosols
Ascona, Switzerland, (poster presentation)

- 2015 European Geosciences Union (EGU), Vienna, Austria, (poster presentation)
- 2016 European Geosciences Union (EGU), Vienna, Austria, (poster presentation)
- 2016 Towards a Molecular-level Understanding of Atmospheric Aerosols,
Santa Cruz, CA, U.S.A, (poster presentation)

